Università
Ca'Foscari
Venezia

Dottorato di ricerca in Scienze Chimiche Scuola di dottorato in Scienze e Tecnologie
Ciclo XXV
Anno di discussione (2012-2013)

Synthesis and characterization of lanthanide based luminescent materials

SETTORE SCIENTIFICO DISCIPLINARE DI AFFERENZA: CHIM/02

Tesi di Dottorato di CHANDRASHEKHAR MAROTIRAO MALBA,

matricola 955770

Coordinatore del Dottorato	**Tutore del Dottorando**
Prof. Maurizio Selva	**Prof. Alvise Benedetti**

DEDICATION

I would like to dedicate this work to my beloved parents and to my mentor Dr. Anjani. J. Varma. My parent's lessons on diligence, discipline, and determination, would be major contributors to any success that I may achieve in life. Dr. Varma has been a guide, philosopher and wonderful source of constant inspiration and motivation to me.

TABLE OF CONTENTS

TABLE OF CONTENTS

List of Figures, Schemes and Tables

List of Figures

List of Schemes

List of Tables

CHAPTER 1

CHAPTER 3

CHAPTER 4

List of Abbreviations

NIR: near infrared

FTIR: fourier transform infrared spectroscopy

NMR: Nuclear Magnetic Resonance Spectroscopy

UV/Vis: Ultra-violet/Visible

XRD: X-ray diffraction

ED: electric dipole

CT: charge transfer

ISC: intersystem crossing

LMCT: Ligand to Metal Charge Transfer

MD: magnetic dipole

DCM: dichloromethane

DBM: dibenzoylmethane

TTA: 1-(2-thienoyl)-3,3,3-trifluoroacetone

phen: 1,10-Phenanthroline

Tp: hydrotris(pyrazol-1-yl)borate

OLED: organic light emitting device

BMIM: 1-butyl-3-methylimidazolium

TOMP: trioctyl methyl phosphonium

NTf_2: bis(trifluoromethylsulfonyl)imide

TEOS: tetraethyl orthosilicate

CTAB: Cetyl Trimethylammonium Bromide

MSN: Mesoporous Silica Nanoparticles

MCM: Mobil Composition of Matter

SBA: Santa Barbara Amorphous type

IL: Ionic Liquid

QY: Quantum Yield

PL: photoluminescence

PLE: photoluminescence excitation

TEM: Transmission Electron Microscopy

TA: Thermal Analysis

TG: Thermogravimetric Analysis

DSC: Digital Scanning Calorimetry

EDS: Energy Dispersive Spectrometry

DTA: Differential Thermal Analysis

$Eu(Tp)_3$: europium (III) tris-pyrazolyl borate

ABSTRACT

In this thesis, synthesis and characterization of new lanthanide based luminescent hybrid materials is studied. The thesis consists of two parts. The silica based luminescent hybrid nanomaterials have been prepared and studied in the first part. The different ways for the nanoencapsulation of rare earth complexes in mesoporous silica nanoparticles have been used to prepare highly luminescent nanomaterials. A highly luminescent $Eu(Tp)_3$ complex with limited solubility in organic solvents has been synthesized in situ inside the pores of presynthesized mesoporous silica nanoparticles. The effect of different chemical environment in the silylated mesoporous silica nanoparticles on the luminescence properties of the Eu(III) complex has been studied in detail by encapsulating $Eu(dbm)_3$phen complex in the pores of organically modified mesoporous silica nanoparticles. Furthermore, solid state NMR studies were performed on the $Y(dbm)_3$phen encapsulated mesoporous silica nanoparticles to obtain the structural and dynamic information on these materials. Co-luminescence effect of Tb(III) and Eu(III) complexes has been studied in the mesoporous silica matrix, with the aim of improving luminescence properties of the encapsulated Eu(III) complex. In the second part of this PhD thesis, new anionic tetrakis lanthanide complexes have been synthesized, characterized and their luminescence properties have been studied in detail in the solid state. Furthermore, the luminescent soft materials were prepared by dissolving anionic tetrakis lanthanide complexes in the phosphonium ionic liquids. The phosphonium ionic liquids have been explored as spectroscopic solvents for studying luminescence of new tetrakis lanthanide complexes.

ESTRATTO IN LINGUA ITALIANA

In questa tesi e' stata condotto uno studio che ha riguardato la sintesi e la caratterizzazione di nuovi materiali ibridi luminescenti a base di lantanidi. La tesi si compone di due parti. Nella prima parte sono stati preparati e studiati dei nanomateriali ibridi luminescenti a base di silice. Sono state utilizzate diverse modalita' per il nanoincapsulamento di complessi di terre rare in nanoparticelle di silice mesoporose per preparare nanomateriali altamente luminescenti. Il complesso luminescente $Eu(Tp)_3$, che genralmente mostra una limitata solubilità in solventi organici, è stato sintetizzato in situ all'interno dei pori delle nanoparticelle di silice mesoporose pre-sintetizzate. E' stato inoltre studiato in dettaglio l'effetto di diverse funzionalizzazioni di nanoparticelle di silice mesoporosa sulle proprietà luminescenti del complesso $Eu(dbm)_3phen$ tramite il suo incapsulamento nei pori modificati sulla superficie delle nanoparticelle di silice mesoporose. Per ottenere le informazioni strutturali e dinamiche su questo tipo di sistemi si sono condotti anche degli studi NMR, allo stato solido, su nanoparticelle di silice mesoporose con il complesso $Y(dbm)_3phen$ incapsulato. L'effetto di columinescenza dei complessi di Tb(III) e Eu(III) è stato studiato in matrice di silice mesoporosa, allo scopo di migliorare le proprietà di luminescenza del complesso di Eu(III) incapsulato in essa. Nella seconda parte di questa tesi di dottorato, sono stati inoltre sintetizzati e caratterizzati nuovi complessi anionici tetrakis conteneti elementi lantanoidi allo stato solido, e sono state studiate in dettaglio le loro proprietà luminescenti. Infine, sono stati preparati materiali luminescenti "soffici" sciogliendo complessi anionici tetrakis conteneti elementi lantanoidi in liquidi ionici a base di fosfonio e sono state studiate le proprità luminescenti relative.

Chapter 1

Introduction

1.1. General introduction to lanthanides

In the periodic table of elements, lanthanide series is comprised of a group of 15 elements ranging from lanthanum (atomic number 57) to lutetium (atomic number 71) (figure 1.1). These are called f-block elements because of the gradual filling of last electron in f-orbital's of the antepenultimate shell. The lanthanide series can be extended with the elements scandium (Z = 21) and yttrium (Z = 39), having similar chemical properties to the lanthanides; the enlarged series is called the rare earths. Despite their name, rare earths are not less abundant in nature than tin or silver.

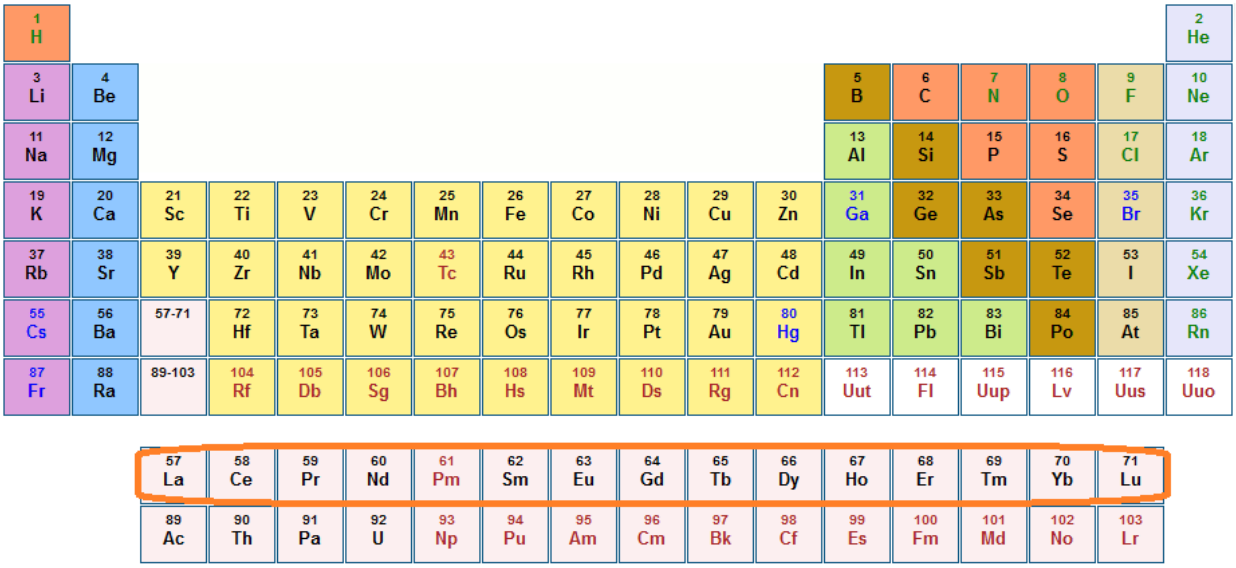

Figure 1.1: The periodic table of elements. The lanthanide series is highlighted at the bottom of the periodic table.

An important feature of the lanthanide ions is their photoluminescence. Several lanthanide ions show luminescence in the visible or near-infrared spectral regions upon irradiation with ultraviolet radiation. For instance, Sm^{3+} emits orange light, Eu^{3+} red light, Tb^{3+} green light, and Tm^{3+} blue light. Nd^{3+}, Er^{3+}, and Yb^{3+} are well-known for their near-infrared luminescence, but other lanthanide ions (Pr^{3+}, Sm^{3+}, Dy^{3+}, Ho^{3+}, and Tm^{3+}) also show transitions in the near-infrared region. The emitting lanthanide ions are characterized by high color purity and are very attractive for applications. An interesting characteristic of emitting lanthanide ions is their line-like emission, which results in a very high color purity for the emitted light. The fascinating spectroscopic properties of the luminescent lanthanide ions make them important for several applications. For instance, they are used for the construction of lamp phosphors,[1] organic light emitting diodes (OLED),[2,3] optical fibres for telecommunications,[3] contrast agents for magnetic resonance imaging,[4] for biological assays.[5-7] Those ions which emit in the near infrared region have found applications in lasers and are also interesting for telecommunications and optical amplifiers.[8,9]

1.1.1. Lanthanide chemistry

Lanthanide elements form +3 oxidation states as a stable oxidation state in the whole series. The only exceptions are Ce^{4+}, Eu^{2+}, Sm^{2+}, Yb^{2+} and Tb^{4+} due to the presence of an empty, half-full or full 4f shell. The 4f orbitals are well shielded by the xenon core, transforming the valence 4f orbitals into "inner orbitals." This phenomenon is the key to the chemical and spectroscopic properties of the lanthanide metal ions.

Ionic radii of the elements in the lanthanide series decrease from atomic number 58, cerium, to 71, lutetium, which results in smaller than otherwise expected ionic radii for the subsequent elements. This phenomenon is termed as lanthanide contraction, is due to the poor shielding of nuclear charge by 4f electrons; the 6s electrons are drawn towards the nucleus, thus resulting in a smaller atomic radius. Trivalent lanthanide ions are hard Lewis acids and a binding preference is observed among the commonly used donor atoms (O > N > S). The nature of bonding in their complexes is electrostatic. As a result, steric factors determine the coordination geometry of lanthanide complexes. Water molecules and hydroxide ions are particularly strong ligands for Ln^{3+}; therefore, in aqueous solution only ligands with donor groups containing negatively charged oxygen's (such as carboxylate, sulfonate, phosphonate, and phosphinate etc.) can effectively bind to the lanthanide ion. The trivalent lanthanide ions (Ln^{3+}) share number of common coordination properties and exhibits coordination numbers from 6 to 12 with eight and nine being most common.

Due to the ionic character, Ln^{3+} ions possess weak stereo-chemical preferences and a labile coordination sphere resulting into variable coordination numbers and geometries.

In the solid state, the most common coordination geometries of the Ln^{3+} complexes are square anti-prismatic, dodecahedral, tricapped trigonal prismatic, monocapped square anti-prismatic, bicapped square antiprismatic and bicapped dodecahedral.

The coordination numbers are more difficult to predict in solution.[10] When the number of donating atoms in the ligand is too little or their electronic density too low, the lanthanide ions complete its coordination sphere with molecules of solvent or anions (water, chloride, hydroxide, etc).

The nature of donor atoms determines the coordination properties of the ligand. As the lanthanide ions show a hard acid behavior, they preferentially bind to hard bases. Therefore, the ligands having negatively charged O or N as donor atoms form stronger bonds. The preference of Ln^{3+} for hard bases is due to its hard acidic character and the predominant ionic nature of bonding interactions. In aqueous solutions, ligands bearing coordinating moieties possessing negatively charged oxygen generate complexes with large thermodynamic stability, resistant to hydrolysis.[11,12] In anhydrous media, nitrogen donors, even if softer, can coordinate lanthanides more strongly, although they undergo at least partial hydrolysis even in the presence of small amounts of water.[10]

1.1.2. Lanthanide spectroscopy

In 1906, Becquerel observed sharp absorption lines while performing absorption measurements on lanthanide ions.[13] The sharpness of these lines could not be understood till Bethe, Kramers and Becquerel suggested that the lines may be due to intraconfigurational 4fn – 4fn transitions.[14-16] Since the electrons in the 4f shell are shielded by the filled 5s and 5p shells, they do not participate in the chemical bonding between lanthanide ions and the ligands. As a result of this, lanthanide ions show sharp line like spectra of free atoms or ions. Each lanthanide ion show a characteristic absorption and emission spectra and it can emit in the near-UV, visible, near-infrared and infrared regions of the electromagnetic spectrum. These intraconfigurational 4fn – 4fn transitions are parity forbidden by the Laporte selection rule. It states that the spectral lines associated with electric-dipole transition must arise from the states of opposite parity. In the non-centrosymmetric systems, electric dipole transitions can be induced by admixture of opposite–parity configurations such as $^4f_{N-1}$- $^5d_1$ and charge transfer states.[17] In the lanthanide ions, magnetic dipole transitions are allowed. Their intensity is practically independent of the surrounding matrix and is easily calculated. An example of a purely magnetic dipolar transition is the $^5D_0 \rightarrow {}^7F_1$ emission line of Eu^{3+}. Electric dipolar transitions in lanthanide ions are induced by the ligand field and their strengths are extremely sensitive to the coordinating environment. Thus, their intensity solely depends on the ligand field. One example of such a transition is a hypersensitive transition, of the $^5D_0 \rightarrow {}^7F_2$ emission line of Eu^{3+}. The selection rules for intraconfigurational 4fn – 4fn transitions in the lanthanides are summarized below (table 1.1).

Table 1.1: Selection rules for lanthanide f-f transitions. S represents total spin angular momentum, L the total atomic orbital angular momentum and J the total angular momentum.

Electric dipolar transitions	Magnetic dipolar transitions
$\Delta S = 0$	$\Delta S = 0$
$\Delta L \leq 6$	$\Delta L = 0$
$\Delta J \leq 6$; $\Delta J = 2, 4, 6$	$\Delta J = 0, \pm 1$; $0 \leftrightarrow 0$ = forbidden

Electric dipolar as well as magnetic dipolar transitions in the lanthanides are weak due to the forbidden transitions. Their luminescence is characterized by narrow emission lines and long lifetimes (in the order of milliseconds). The absorption of the lanthanide ions is weaker due to the forbidden transitions. This makes direct photo-excitation of lanthanide ions difficult. This can be overcome by using the large absorption cross section of the organic chromophores and the energy transfer from organic chromophores to lanthanide ions can be obtained via antenna effect. Lanthanide ions can form complexes with the organic ligands such as β-diketones, polyaminopolycarboxylic acids, pyridines and calixarenes etc. Highly luminescent lanthanide complexes can be obtained by designing ligands with suitable photophysical properties. Lanthanide ions that emits in the visible spectral region are Eu^{3+} (red), Eu^{2+} (blue), Tb^{3+} (green), Sm^{3+} (orange) and Tm^{3+} (blue). Typical near-infrared emitting lanthanide ions are Nd^{3+}, Er^{3+} and Yb^{3+}.

1.1.2.1 Important terms and properties

a) Energy levels in the lanthanide ions

In the lanthanide series, going from La^{3+} to Lu^{3+}, the 4f–shell is filled from 0 to 14 electrons. As the 4f electrons are shielded by the outer 5s and 5p shells, they have only little interaction with the chemical environment of the ion and do not play role in chemical bonding. The most stable configurations are $4f^0$ (empty f-shell), $4f^7$ (half filled-f-shell) and $4f^{14}$ (filled-f-shell).

The different interactions within the lanthanide ion are responsible for the different energy levels for the same configuration. Among these interactions, electron-electron repulsions within the 4f orbitals, are the largest and yields terms with a separation in the order of 10^4 cm^{-1}. This in turn

splits into several J levels by the spin orbit coupling (figure 1.2). This is the interaction between the spin magnetic moment of the electron and the field created through the movement around the nucleus. At the free ion level, the energy states for the lanthanide ions are given by $(2S+1)\ L_j$ terms. Where S = total spin angular momentum, L = total atomic orbital angular momentum and J = total angular momentum. When the ions are present in coordination with the ligands, the spherical symmetry of the free ion is destroyed. This also causes an electrostatic interaction between the 4f electrons and the electric field of the ligands. This is referred to as the crystal field.

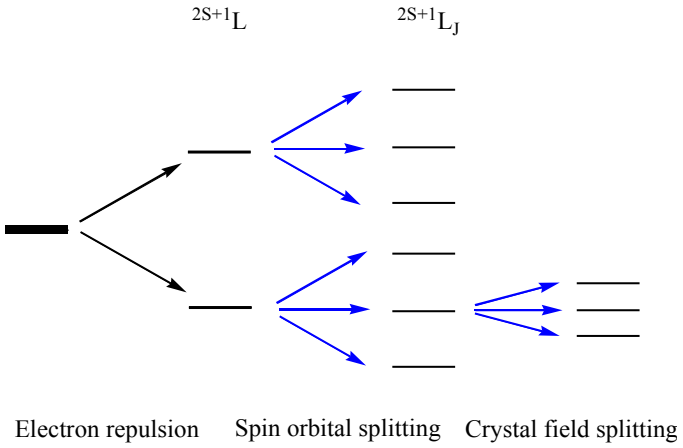

Figure 1.2: Energy levels splitting for the lanthanide ions with $4f^N$ configuration.

The energy level diagram for the selected lanthanides is shown in figure 1.3. This diagram can be used to illustrate the luminescent properties of the Eu^{3+}, Tb^{3+} and Sm^{3+} ions. These elements have the largest gaps in the energy level bands which allow the greatest luminescent intensities because they have longer decay lifetimes.

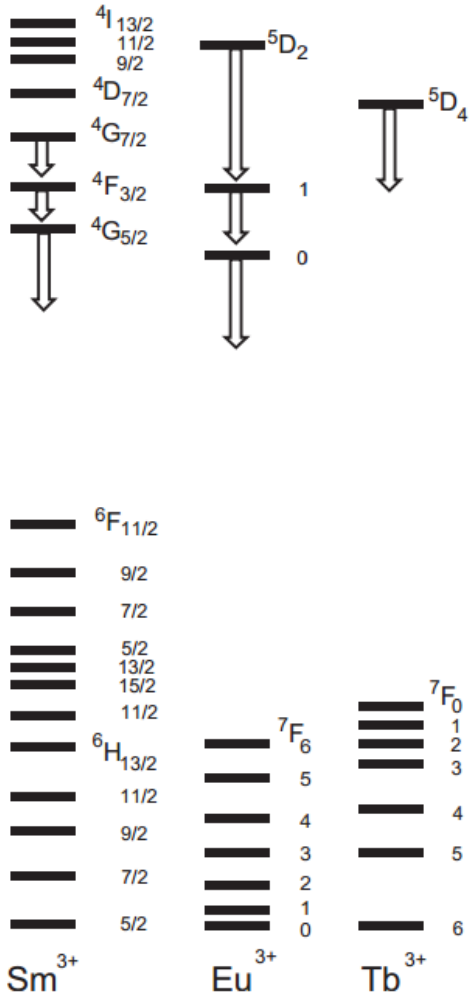

Figure 1.3: Lanthanide (III) energy level diagram adapted from Dieke diagram, showing the large energy gaps in low-lying levels. Levels that commonly luminesce are designated by downward arrows.

b) Hypersensitivity

As mentioned above, Ln(III) ions have only little interaction with the chemical environment. As a consequence, the intensities of the transitions are in general not much affected by the local environment. However, there are some exceptional transitions that are very sensitive to the small changes in the ligand coordination sphere and are more intense when the ion is complexed than they are in the corresponding aqua-ions. The oscillator strength and band shape of these transitions in Ln(III) complexes are especially sensitive to the structural details and the chemical nature of the ligand environment. These transitions are called hypersensitive transitions and the

phenomenon is generally referred to as hypersensitivity. For the lanthanide series, these transitions are normally the most sensitive spectroscopic monitors of a changing ionic environment. The hypersensitive transitions obey to the selection rules $|\Delta S| = 0$, $|\Delta L| \leq 2$ and $|\Delta J| \leq 2$. These are the useful tools in the analysis of Ln(III) spectroscopic data. Some important hypersensitive transitions are shown in table 1.2.

Table 1.2: Most important hypersensitive transitions: absorption (←) and emission (→).

Lanthanide ion	Hypersensitive transition	Wave number (cm^{-1})	Wavelength (nm)
Eu^{3+}	$^5D_2 \leftarrow {}^7F_0$	21500	465
	$^5D_1 \leftarrow {}^7F_1$	18700	535
	$^5D_0 \rightarrow {}^7F_2$	16300	613
Tb^{3+}	$^5D_4 \rightarrow {}^7F_5$	18300	546
Sm^{3+}	$^4F_{1/2}, {}^4F_{3/2} \leftarrow {}^6H_{5/2}$	6400	1562

c) Non radiative decay

The excited states of lanthanide ions do not decay solely by radiative processes. If the excited state and the next lower state energy gap is relatively small, luminescence will be in strong competition with the non-radiative decay of the excited state. The electronic excitation energy can be dissipated by vibrations of the matrix, by a process known as multiphonon relaxation.[18] It can occur through coupling of the lanthanide energy levels with the vibrational modes in the direct surrounding of the lanthanide ion. The high energy O-H vibrations are very efficient quenchers for lanthanide luminescence therefore water molecules are avoided from the first coordination sphere of the lanthanide complexes.

d) The antenna effect

The absorption coefficients of the f-f transitions in the lanthanide ions are very weak, which makes direct photo-excitation of the lanthanide ions difficult. However, this can be overcome by using the large absorption cross section of the organic chromophores and the energy transfer from organic chromophores to lanthanide ions can be obtained via antenna effect (figure 1.4).

Thus, in order to design highly luminescent Ln^{3+} complexes, prerequisite is to optimize the ligand–Ln^{3+} energy transfer process in order to maximize the emission originated from 4f–4f intraconfigurational transitions.[19]

Weissman first noticed the sensitization process in which the energy transfer takes place from coordinated ligands to the central metal ion.[20] The mechanism of energy transfer from organic ligands to the lanthanide ion involve three steps: (i) strong absorption from the ground singlet state (S_0) to the excited singlet state (S_1) of the ligand; (ii) state S_1 decays non-radiatively to the triplet state (T_1) via intersystem crossing and (iii) nonradiative energy transfer pathway from the T_1 state of the ligand to excited states of the Ln^{3+} ion.[21-23] In some cases the direct energy transfer from the S_1 singlet state to the excited Ln^{3+} levels is also observed[24]. A simplified scheme of these energy transfer processes is given in figure 1.5.

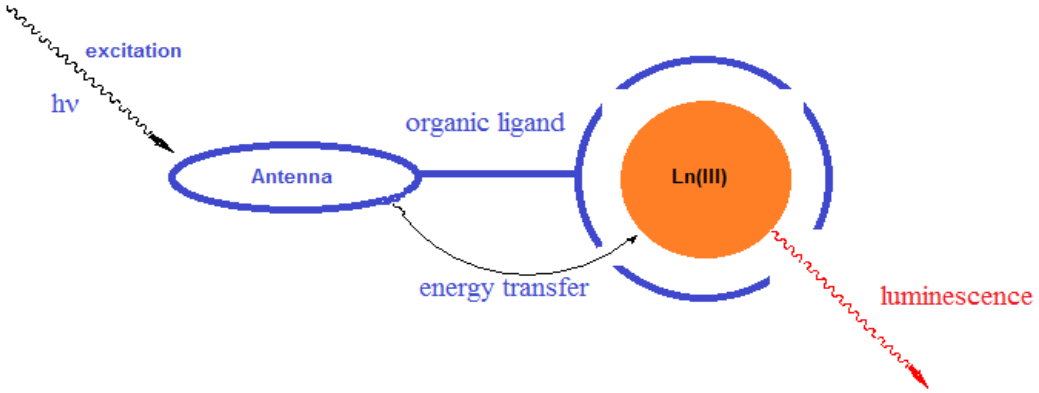

Figure 1.4: An illustration of the 'antenna' effect, the incident excitation energy is first absorbed by a coordinated organic chromophore and then transferred to the central metal atom in the lanthanide (III) complexes.

The overall process is complex and involves several mechanisms and energy levels. After the indirect excitation by energy transfer, the lanthanide ion may undergo a radiative transition to a lower 4f-state by characteristic line-like photoluminescence, or may be deactivated by radiationless processes. The scheme of the processes is shown in figure 1.5.

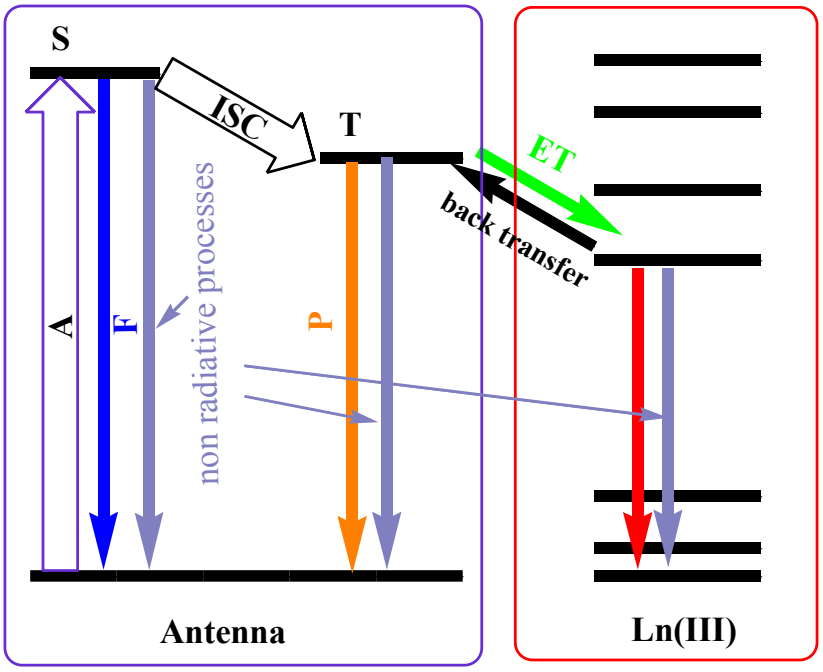

Figure 1.5: Schematic representation of photophysical processes in Ln(III) complexes (antenna effect). Abbreviations: A = absorption, F = fluorescence, P = phosphorescence, ISC = intersystem crossing, ET = energy transfer, S = singlet, T = triplet.

The β-diketonate complexes are known to be very efficient sensitizers for the lanthanide ions.[25-29] Thus, organic ligands coordinated to lanthanide ions has a twofold beneficial effect, they not only increase the light absorption cross section by ‘‘antenna effects’’ but also protects metal ions from vibrational coupling.[30-33]

1.1.3. Lanthanide based luminescent materials

A great deal of research has been carried out in the field of lanthanide based luminescent materials in the last decade. The luminescence of lanthanide ions has applications ranging from display applications to bioimaging and sensing.

The practical application of lanthanide luminescence requires the ions to be incorporated into a matrix that is robust and compatible with respect to the intended application. For instance, when lanthanide luminescence is used for the detection of biological molecules, the luminescent material needs to be compatible with biological and aqueous environments and the individual light emitters should be small enough not to interfere with any of the biochemical processes in the sample under study. These materials have been obtained either by embedding a molecular

lanthanide complex in an inorganic host matrix, or embedding inorganic lanthanide compound in an organic polymer matrix.[34] Embedding luminescent lanthanide compounds in host matrix materials are of fundamental interest because of their high potential for different applications (optical amplifiers, optical waveguides, OLEDs, etc.). In general, the hybrid materials have superior mechanical properties and have a better processability than the pure molecular lanthanide complexes. Moreover, embedding a lanthanide complex in a hybrid matrix is also beneficial for its thermal stability and luminescence output.

Complexes of lanthanide ions with organic ligands are a class of luminescent materials that are different from the inorganic materials. Organic ligand incorporates an organic chromophore to enhance the effective absorption cross section as the chromophore absorbs the light and transfers the energy to the lanthanide ion. However, the presence of molecular high-energy vibrations in organic ligands and solvents makes that non-radiative relaxation of excited lanthanide ions much more efficient in luminescent lanthanide complexes. Since the O-H vibrations of water act as quenchers of lanthanide luminescence, the lanthanide ion has to be protected from such quenchers so as to use these systems in the aqueous and biological media. Deuteration and fluorination reduce quenching to some extent.[35] Besides; these chromophores are unstable to the intense laser powers which are used to pump the lanthanide ions in order to achieve optical amplification.[36] The β-diketones complexes are the most intensively studied for the lanthanide coordination compounds. Lanthanide complexes can be designed to be sensitive to pH, temperature, oxygen or other analyte concentrations.[37-38] Organic ligands can be designed to tune their physicochemical and biological behavior.

Inorganic hosts such as glasses and crystals have less effective non-radiative deactivation channels for excited lanthanide ions than the molecular hosts. They reduce the non-radiative deactivation channels and give rise to richer lanthanide photophysics. Near IR luminescence, emissions from higher excited states are therefore more readily observed for lanthanides in inorganic hosts.

The lanthanide ions are doped into sol-gel glasses via sol-gel process. An advantage of the sol-gel process is that it enables preparation of glasses at far lower temperatures than those of the conventional melt processes. This allows avoidance of the problems of phase separation and

crystallization that are often observed for high-temperature melt processes. It is also possible to encapsulate organic compounds or metal complexes in the sol-gel glass.[39-42] The sol-gel process can be used to prepare bulk samples (monoliths) as well as thin films and fibers.[34] The encapsulation in sol-gel glasses increases the photostability of organic luminophores.[43, 44]

Hybrid organic-inorganic nanocomposites are obtained by the confinement of the non volatile solvent containing the luminescent lanthanide complexes in the porous silica network of the xerogels. Similarly, the lanthanide complexes can be incorporated into porous hosts such as zeolites or the hybrid materials with polymers can be obtained by incorporating them in the polymer matrix. Their incorporation in polymer matrix can be obtained by either blending or by covalent bonding to the polymer matrix. Lanthanide compounds are also doped in nanoparticles. Lanthanide-doped nanoparticles are interesting compounds, because they possess the excellent luminescent properties of inorganic phosphors and also because they are compatible with molecular materials. For instance, the quenching of lanthanide luminescence in sol-gel-derived materials arising due to concentration quenching and remaining hydroxyl groups can be avoided by doping lanthanide-containing nanoparticles instead of molecular lanthanide complexes in the sol-gel matrix. Nanoparticle-polymer composites can also be prepared by dispersing the luminescent nanoparticles in a polymer matrix. These are interesting materials because they combine the advantages of both polymers (good processability and good mechanical properties) and inorganic luminescent materials (high luminescence efficiency and long-term chemical stability).

Each type of host for lanthanide ions used for the construction of luminescent materials has its strengths and weaknesses.

1.2. Mesoporous silica nanoparticles as host matrix

The first part of this PhD thesis focuses on the lanthanide based luminescent hybrid materials prepared by encapsulation of lanthanide complexes in mesoporous silica host matrix. The profound interest in the use of mesoporous silica nanoparticles (MSNs) for many different applications is due to their several inherent properties such as low toxicity, excellent chemical stability and versatile functionalization chemistry. MSNs are chemically inert, thermally stable,

harmless, and inexpensive.[45] They also have the capability of being platforms for, or being integrated with, other nanomaterials.[46]

Unlike many other nanomaterials, MSNs have constant physical properties similar to those of bulk material, except the total surface area increases as the size decreases. In addition to the higher surface area, what really makes MSNs attractive is their well-defined tunable nanostructures and well-established organosilicate chemistry, which allow us to synthesize particles with functional architectures for applications in many different fields. Using the Stöber sol-gel process,[47] it is possible to grow particles from tens of nm to microns in diameter, simply by varying the precursor concentrations.

An advantageous property of MSNs is their high surface area, which allows higher loading of the active guest molecules. This greater surface area can be functionalized with specific functional groups to improve their suitability for the intended application. Since multiple types of molecules can be incorporated into a single nanoparticle surface concurrently, enabling the preparation of multifunctional materials. Mesoporous silica is an excellent host material for a wide variety of functional materials, including luminescent lanthanide complexes, fluorescent dyes, metal nanoparticles and biomolecules. These materials have been used as host materials for loading catalysts,[48, 49] polymers,[50-54] metals[55] and semiconductor nanoparticles[56-60] that have potential catalytic, environmental[61] and optoelectronic applications.[62,63]

Numerous methods have been reported for the preparation of mesoporous silica materials with various morphologies from thin films, sphere, fiber, as well as bulk form, such as the MCM series[63] and the SBA series.[65] Organosilane precursor such as tetraethylorthosilicate [TEOS] is utilized in the sol-gel process. Upon hydrolysis and condensation reactions of TEOS, formation of a new phase (sol) takes place. The condensation of the small colloidal particles within the sol leads to the gel phase.[66] The main steps involved in the sol-gel process can be described by equations 1.1,1.2 and 1.3 (figure 1.6).

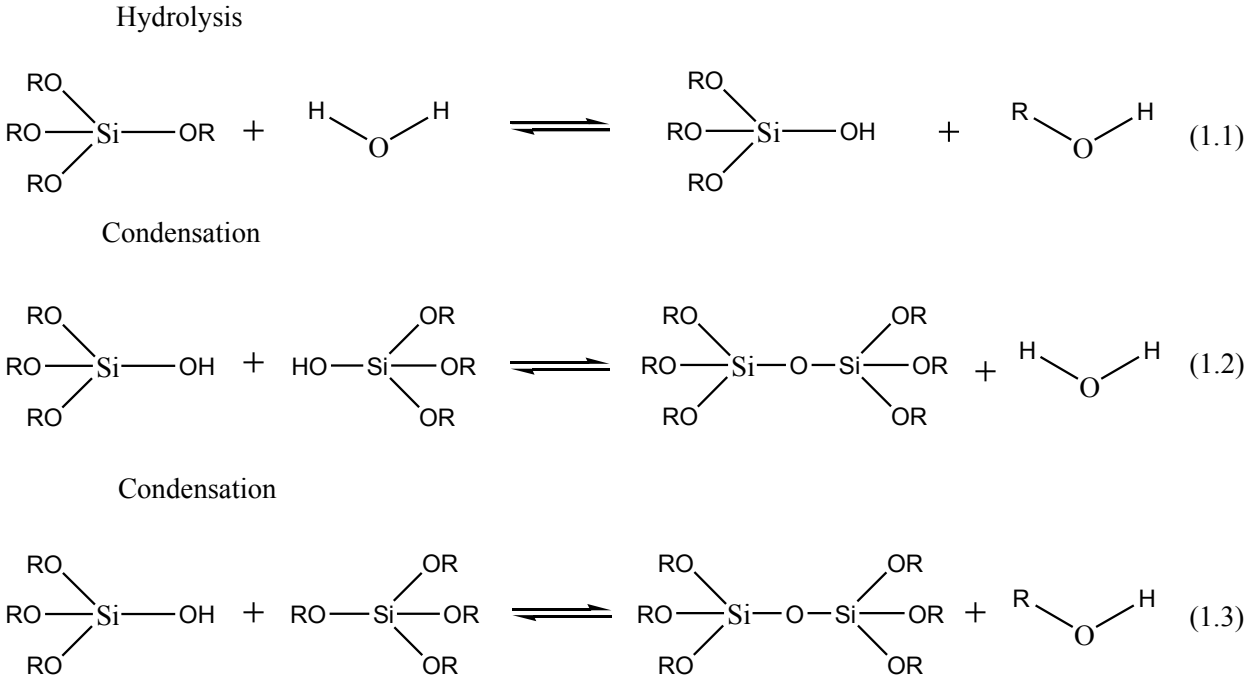

Figure 1.6: The main steps involved in the sol-gel process (1.1) hydrolysis of alkoxy groups; (1.2) condensation of two silanol groups; (1.3) condensation of a silanol and an alkoxy group.

For instance, Stöber process has been widely used to prepare monodispersed silica nanoparticles with the size in the range between 50 and 200 nm, by the ammonia-catalyzed hydrolysis of TEOS in a water-alcohol solution.[47]

In this thesis, a base-catalyzed sol–gel process reported by Qiao et al.[67] has been employed to produce silica nanoparticles. In a typical synthesis, the silica source, tetraethylorthosilicate (TEOS), is added into a heated basic aqueous alcoholic solution of the cationic templating surfactant, cetyltrimethylammonium bromide (CTAB). The templating surfactant is later removed by its decomposition by the calcination process to obtain mesoporous silica nanoparticles. The surfactant CTAB is shown in figure 1.7. It self-assembles in an aqueous environment into various regular mesophases. A silica precursor TEOS is attracted by these micelles without destroying their order or integrity, which is able to condensate around the micelles, i.e. which is able to form new chemical bonds among each other, to give a macromolecular network.

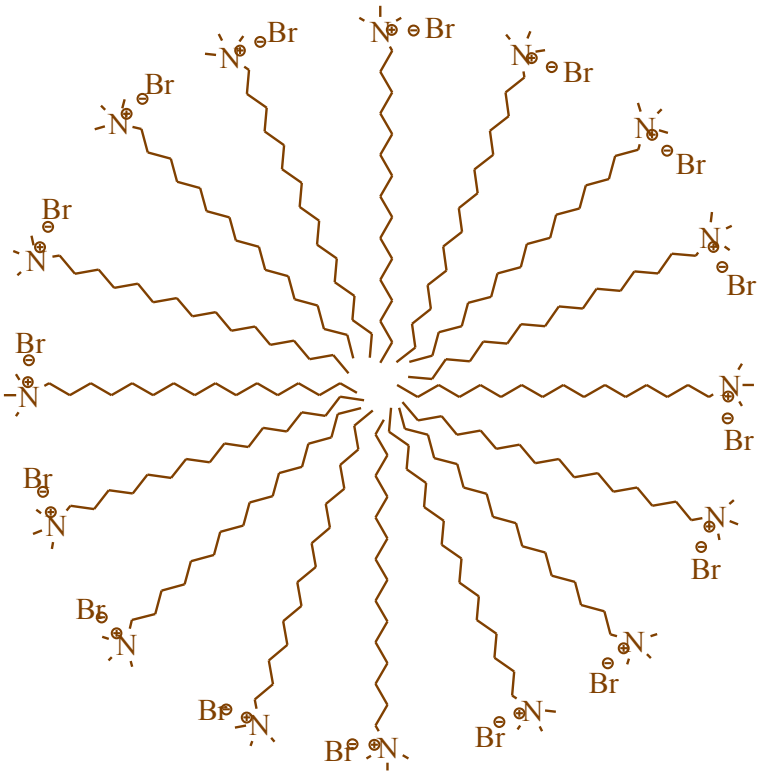

Figure 1.7: The cross section of a roughly spherical structure of CTAB surfactant micelle.

The different steps involved in the synthesis of surfactant templated MSNs are illustrated in figure 1.8. These MSNs were further used for the preparation of luminescent nanomaterials.

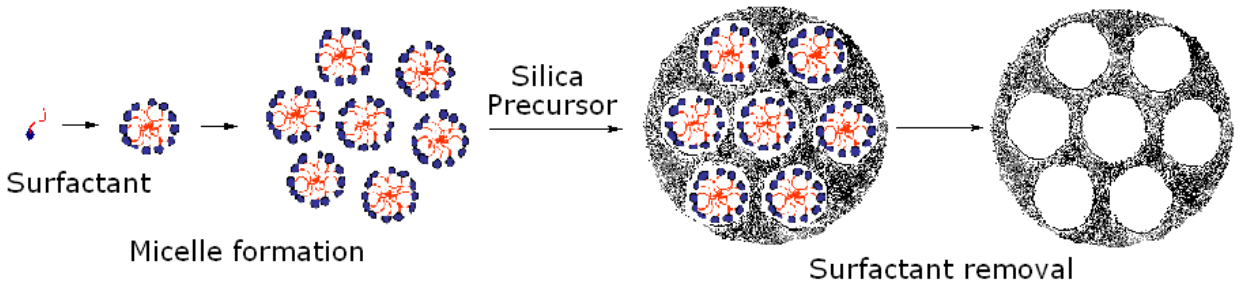

Figure 1.8: Illustration of the steps involved in the synthesis of surfactant templated MSNs.

Further, many researchers have focused on the preparation of organically functionalized MSNs by covalent attachment of a wide variety of functional groups by post-synthesis grafting on the MSNs exploiting the simple polycondensation chemistry of silica. Surface functionalization of (MSNs) with organic moieties enhance the biocompatibility of these materials.[68, 69] The surface modification of MSNs with organic moieties allows a wide range of manipulation of the surface

properties and brings controlled release and molecular recognition capabilities to these materials for drug/gene delivery and sensing applications, respectively.[70] Surface-modified nanoparticles can be used in organic and biological media for polymer optical amplifiers or biological imaging, and luminescent lanthanide complexes may generate light in electroluminescent devices, or work efficiently as near-infrared emitters.

The encapsulations of rare-earth complex in mesoporous silica matrix have been extensively studied. The most common way of encapsulation of luminescent rare earth complexes in the porous nanoparticles includes the utilization of the widely used impregnation technique. This technique is useful when the complex to be encapsulated is soluble in commonly used organic solvents. However, the complexes that are insoluble or minimally soluble in organic solvents need to be either synthesized in-situ inside the pores of presynthesized nanoparticles or they have to be synthesized during the nanoparticle synthesis process. In this thesis, luminescent nanomaterials were prepared by encapsulating the presynthesized rare earth complexes. For instance, an in situ synthesis approach for the nanoencapsulation of the scarcely soluble europium complex was used to prepare a highly luminescent europium containing nanomaterial. The surface functionalization of MSNs changes the chemical environment inside the pore structures of nanoparticles.

Literature shows improvement of luminescent properties of the encapsulated rare earth complex when it is incorporated in the organically modified porous matrix. Therefore, in this thesis a detailed study on the effect of different chemical environment on the luminescence of rare earth complex was carried out by encapsulating the $Eu(dbm)_3phen$ (tris(dibenzoylmethane) mono(1,10-phenanthroline)europium(III)) complex inside the pores of organically modified MSNs. Since the –OH vibrations on the surface of MSNs act as quenchers for the luminescence of lanthanide complexes, functional groups such as $–NH_2$, –SH, $–(CH_3)_3$ were grafted on MSNs to reduce the luminescence quenching of $Eu(dbm)_3phen$ complex. These functional groups not only reduce the luminescence quenching but also provides different chemical environments for the encapsulated $Eu(dbm)_3phen$ complex. An influence of the presence of organic functional groups grafted on surface of MSNs on the structural and photophysical properties of the encapsulated rare-earth complex has been examined. The solid state NMR study was carried out on the functionalized silica materials containing an analogous diamagnetic model complex -

($Y(dbm)_3phen$ (tris(dibenzoylmethane) mono(1,10-phenanthroline)yttrium(III)). The solid state NMR study could not be carried out on the materials containing europium complexes owing to their paramagnetism which causes dramatic broadening of the NMR peaks and shortening of the relaxation times. In order to investigate the structural behavior of the $Eu(dbm)_3phen$ doped in functionalized MSNs, an analogous diamagnetic model complex ($Y(dbm)_3phen$ complex was purposely synthesized wherein the europium is replaced by yttrium which has the similar chemical behavior and atomic radius of Eu and encapsulated in the functionalized MSNs. Three different types of nuclei were investigated, ^{1}H, ^{13}C and ^{29}Si, exploiting several SSNMR techniques, with the aim of obtaining meaningful structural and dynamic information on these materials.

1.3. Ionic liquids

In recent years, Ionic liquids (ILs) have attracted, quite justifiably, enormous attention as neoteric solvents (new types of solvents) for green synthesis. The first room-temperature ionic liquid (RTIL), ethyl ammonium nitrate $[CH_3CH_2NH_3]^+ [NO_3]^-$ (MP: 12-14 °C), was prepared by the neutralization of ethylamine with concentrated nitric acid in 1914.[71] This discovery did not arouse immediate interest in the scientific community of the day. The next half century only few reports appeared on the use of ionic liquids as solvents for organic reactions but occasional reports on its use as media for electrochemical studies.[72] As their name implies, ILs are salts that are liquid at low temperature. They are better viewed as a new type of non-aqueous solvent. Many of them are liquid at or below room temperature and that in the molten form these consist entirely of ionic species.[73,] The term room-temperature ionic liquids (RTIL), is used to describe salts that remain liquids at ambient or far below ambient temperature.[74] Due to manifold cation/anion combinations, ILs can be constructed to meet the needs of specific applications and are therefore also called tailor made or designer solvents.[75]

The RTILs are comprised of combinations of organic cations, such as imidazolium, pyridinium, pyrrolidinium, ammonium, sulfonium and phosphonium derivatives, and bulky anions, such as $[BF_4]$, $[PF_6]$, $[CF_3SO_3]$, and $[(CF_3SO_2)_2N]$ etc.[76-83] Examples of some commonly used ionic liquid systems are shown in figure 1.9.

a) Most commonly used cations

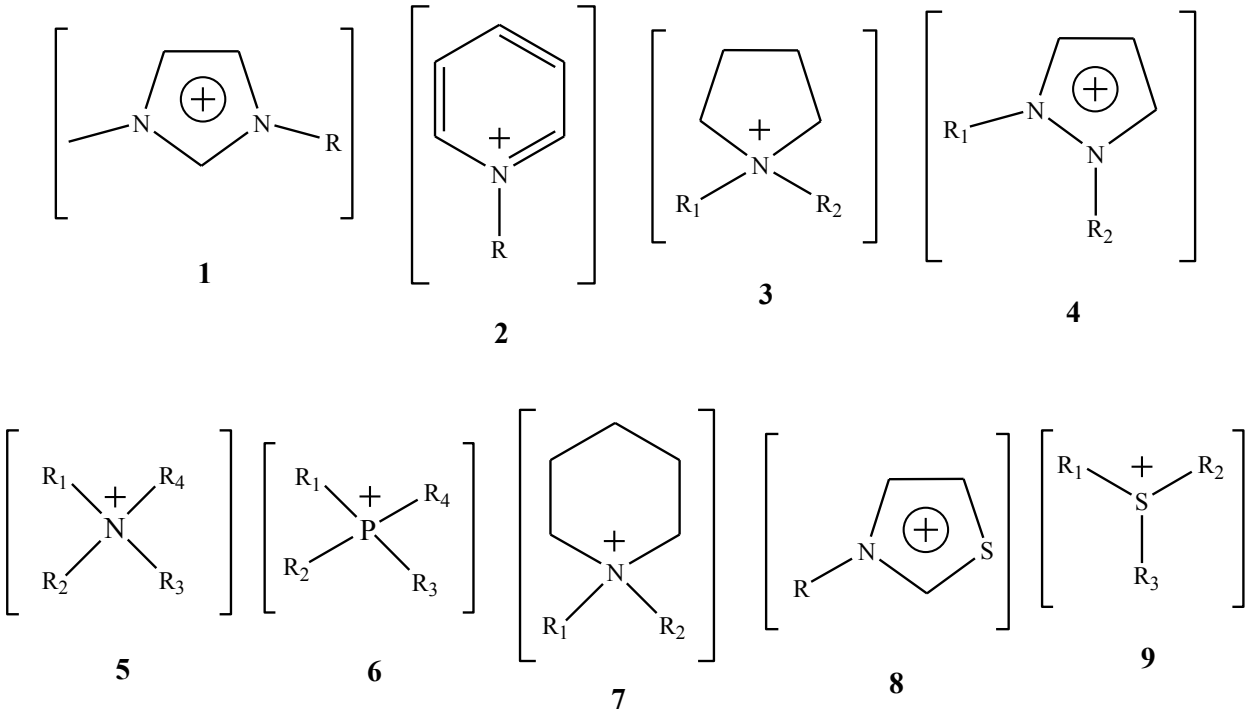

b) Some commonly used anions

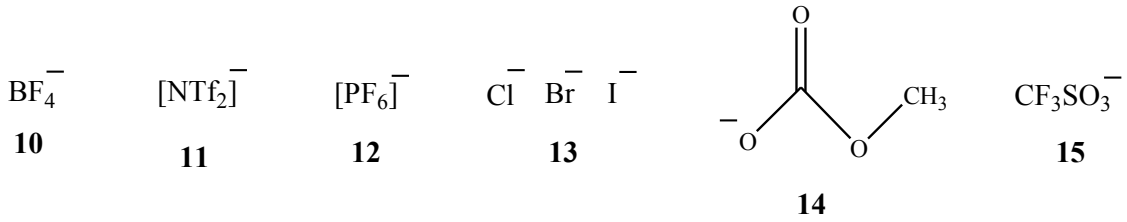

Figure 1.9: Some commonly used cations and anions in the ionic liquid systems. a) Cations: (1) 1-alkyl-3-methyl- imidazolium (2) N-alkyl- pyridinium (3) N-alkyl- N-methyl- pyrrolidinium (4) 1,2-dialkyl- pyrazolium (5) Tetraalkyl- ammonium (6) Tetraalkyl- phosphonium (7) N-alkyl- N-methyl- piperidinium (8) N-alkyl-thiazolium (9) Trialkyl- sulfonium b) Anions:(10) Tetrafluoroborate (11) Bis(trifluoromethane)sulfonimide (12) Hexafluorophosphate (13) Halide (14) Methyl carbonate (15) trifluoromethane-sulfonate.

Due to the availability of large variety of cations and anions, their combination amounts to numerous potential ionic liquids. Therefore, physicochemical properties of the ionic liquids can be easily tuned simply by changing the structure of the component ions. However, a few typical ionic liquids those containing imidazolium cations are mostly used.[84]

An understanding of the physical and chemical properties of the ionic liquids is therefore vital to establish the usefulness of the new materials.

1.3.1. Physical and chemical properties of ionic liquids

The physicochemical properties of ionic liquids depend on the constituent cations, anions and the length of the lateral alkyl groups on the heterocyclic rings; therefore it is possible to easily fine tune the physicochemical properties of ionic liquids such as viscosity, solvation, catalytic activity, hydrophobicity, and melting point etc. simply by altering the anion or the alkyl group length.[85, 86]

Ionic liquids have many fascinating properties which make them of fundamental interest to the chemists. They possess unique physicochemical properties, such as negligible vapor pressure, non-flammability, high ionic conductivity, and high thermal, chemical, and electrochemical stability, which make them so distinct from organic solvents.[73]

Due to the combined effect of greater thermal stability and non-volatility, ionic liquids tend to have much greater liquidus temperature range (Liquidus range is the span of temperatures between the freezing point and boiling point of a liquid). The lower melting point of the ionic liquid is due to the reduction in the lattice energy of the crystalline form of the salts arising from the low degree of the symmetry of cation.[87]

Ionic liquids do not emit any volatile organic compounds (VOCs). The strong Columbic forces between the anions and cations of the liquid are responsible for the lack of vapor pressure for most of the ionic liquids. They possess several properties that compel their use as reaction media. First and foremost is the great stability of salts-thermal, chemical, and electrochemical. Ionic liquid can be recycled, leading to reduction of the costs of the processes.

As stated above, the variability of the constituent ion (anion or cation) in a given IL may lead to remarkable changes in their physicochemical properties. Thus, the optimization of physical solvent characteristics such as miscibility with water and other solvents, dissolving ability, polarity, viscosity, density, etc. and coordination abilities can be achieved by different (appropriate) cation/anion combinations. Thus, they are often considered as designer solvents.[73]

An important property that changes with structure is the miscibility of water. This behavior can be of interest when carrying out solvent extractions or product separations. In general, the anion has greater role in determining hydrophobicity of the ionic liquid than the constituent cation. It is known that halide anions form ionic liquids which are miscible with water while other anions such as the bistriflimide anion ($[Tf_2N]$-) typically form hydrophobic ionic liquids, saturated by less than 2% of water.[83] Longer alkyl chains on the cation and fluorinated anions can also increase the hydrophobic character of the ionic liquid. However, regardless of their hydrophobic or hydrophilic behavior all ionic liquids are found to be hygroscopic. Therefore, careful drying of the ionic liquids before use is necessary.

1.3.2. Applications of ionic liquids

In general, ionic liquids possess good dissolution properties for most organic and inorganic compounds. Their attractive properties such as greater densities (higher than unity), nonflammability, low volatility together with the ease of handling and high ionic concentration, has enabled ionic liquids to be used for many different applications. For instance, they are proven to be excellent reaction media for a wide range of organic and inorganic reactions,[73, 88, 89] they are used as separation solvents,[90-93] in the catalysis, [94-99] materials synthesis, sensing, [100] and chemical separation.[101] The reactions in ionic liquids are often quicker and relatively easier to perform than in conventional organic solvents. They may be designed for specific applications by incorporation of functionalities in its cation or anion as well as by using suitable cation–anion combination.

Ionic liquids are ionic conductors[102] and they have been utilized as electrolytes for electrochemical devices. Their application in the devices such as lithium batteries, electric double layer capacitors, dye-sensitized solar cells, fuel cells, and actuators, has also been studied extensively during the last few years.[103-114] Ionic liquids can also dissolve enzymes,[115] form both polymers and gels for device applications.[102]

Ionic liquids possess unique physicochemical properties and their use may lead to new materials with interesting morphologies and properties that are not accessible by using conventional organic solvents. Ionic liquids find applications in the synthesis of inorganic materials,[116-118] photochemistry and spectroscopy,[119] desulfurization of fuel,[120] enzymatic syntheses,[121] rocket

propulsion,[122] thermal storage devices,[123] separation and extraction of actinide and lanthanide, and for the for the electrodeposition of the electropositive f elements.

1.3.3. Ionic liquids as spectroscopic solvents

Wilkes et al. for the first time proposed RTILs based on the 1-alkyl-3-methylimidazolium cation as spectroscopic solvents in 1982.[124] However, the work was more focused on electrochemical properties of the ionic liquids. Later he studied mixtures of I-methyl-3-ethylimidazolium chloride with aluminum chloride and reported the dependence of the chemical shifts of protons on the cations on the proportions of aluminum chloride and organic chloride salt. The interactions between the anions and cations in the melts were studied by nuclear magnetic resonance (NMR) spectroscopy.[125]

Over the past few years, research and applications of ILs have expanded tremendously. The initial impetus for this expansion was organic synthesis and the growth of green chemistry. Later, their applications in separations, chromatography, spectroscopy, and electrochemistry have been extensively studied. With the increased interest in the ionic liquids in various fields, they became a real alternative for conventional solvents in spectroscopic experiments. Detailed studies were carried out to study the polarity and solvation properties of the ionic liquids by performing UV-Vis absorption and (steady-state and time resolved) fluorescence measurements by dissolving different organic chromophores in an ionic liquid.[126-129] Some research groups studied luminescence of metal complexes in ionic liquids to get insight in the molecular dynamics of these systems.[130,132] The studies on absorption and luminescence properties of uranyl-compounds dissolved in ionic liquid have been the subject of many research papers.[133-138] The research groups of Bünzli and Binnemans used ionic liquid as spectroscopic solvent for lanthanide spectroscopy.[133] Room-temperature ionic liquids have been used as solvents for electronic absorption spectroscopy of halide complexes of transition metals.[139]

1.3.4. Phosphonium ionic liquids

In recent years, a great deal of attention has been given to imidazolium ionic liquids which is clear from the published journal literature. Perhaps, imidazolium ionic liquids are the most extensively studied class of ionic liquids and these ILs have found uses in small-scale synthesis,

catalysis and more recently in industrial applications. As a result, most of the spectroscopic studies on lanthanide compounds in ionic liquids have been performed with ionic liquids based on imidazolium ionic liquids. By comparison, phosphonium ionic liquids have previously received less attention for the spectroscopic studies. Phosphonium ionic liquids offer a good alternative to imidazolium ionic liquids for many applications.[140] An important difference between imidazolium and phosphonium ionic liquids is the acidic protons present in the former. Relative to phosphonium cations, imidazolium cations are not entirely inert and can interact with solutes either through hydrogen bonding interactions or through the aromatic nature of the ring system.[141] Tetraalkylphosphonium salts do not have such acidic protons or aromatic rings, and consequently there is little potential for interaction with solutes. Phosphonium ionic liquids combine the general properties of ionic liquids such as an inherent high thermal, chemical and electrochemical stability with a low viscosity and good solubility of metal complexes.

Phosphonium ionic liquids are found to be thermally more stable than imidazolium based ionic liquids. Thermal stability in excess of 300 °C has been reported for phosphonium ionic liquids.[140] They are found to be more robust than imidazolium based ionic liquids and do not undergo decomposition in the presence of active metals. PILs were found to have a wider electrochemical window than imidazolium based ionic liquids. Due to the higher thermal stability the traces of moisture can be easily removed.

1.3.5. Lanthanide spectroscopy in ionic liquids

Gau et. al. studied UV-Vis absorption of europium (III) complexes in an ionic liquid for the first time in 1996. They studied chloride complexes in chloroaluminate-1-ethyl-3-methyl-imidazolium chloride, $AlCl_3$-[C_2mim]Cl.[142] Since then, numerous studies have been performed on lanthanide ions dissolved in ionic liquids.[130-132,143-149] Bünzli and coworkers noticed energy transfer from ionic liquid crystals to the dissolved Eu^{3+} salts.[150] Binnemans and co-workers have shown an enhancement of the photostability of a tetrakis(2-thenoyltrifluoroacetonato) europate(III) complex in imidazolium ionic liquid [C_6mim][Tf_2N] in comparison to organic solvent (acetonitrile solvent).[151] An imidazolium ionic liquid ([C_{12}mim]Cl) doped with 1 mol. % Ln(tta)$_3$phen (Ln = Nd, Eu, Er and Yb) complexes were investigated by Bünzli and coworkers.[152]

Ionic liquids have been shown to be suitable solvents for near-infrared emission[153]. An intense near-infrared luminescence for neodymium(III) iodide and erbium(III) iodide dissolved in the ionic liquid $[C_{12}mim][Tf_2N]$ was reported by Arenz et al.[154] The observed intense near-infrared emission in the ionic liquid is attributed to the anhydrous ionic liquid samples. The absence of traces of water in the hydrophobic ionic liquid as well as to the lack of high-energy vibrations such as C-H, N-H and O-H in the first coordination sphere of the lanthanide complex improved the luminescence of these compounds.

In summary, ionic liquids have been shown to be suitable spectroscopic solvents for studying the luminescence of lanthanide compounds. By the appropriate choice of an anion of the ionic liquid a suitable environment around the lanthanide ion can be obtained. The ionic liquid anion and the anion of the lanthanide compound compete for the first coordination sphere of lanthanide compound. Weakly coordinating ionic liquids are therefore preferred. The dissolution of lanthanide compounds in ionic liquids significantly improves luminescence properties of the lanthanide compounds. Improvement of the properties such as photostability, electrochemical stability, energy transfer from the ionic liquid and better resolution for infrared luminescence is reported. However, these properties are not yet studied in detail. Moreover, the published journal literature shows very few studies on comparative studies of luminescence of lanthanide compounds in ionic liquids with the commonly used organic solvents. Majority of the published work focused on more common imidazolium and other nitrogen-containing ILs and the quaternary phosphonium ILs have not received the required attention for studying luminescence of lanthanide compounds. As, they have been used extensively in different areas of chemistry for many years, particularly catalysis and phase transfer reactions and extractions,[155-157] these can also find applications for studying lanthanide compounds.

1.4. Scope of this thesis

The core of this thesis (Chapters 3, 4, 5 and 6) is based on the preparation of lanthanide based luminescent hybrid materials. In particular, two kinds of lanthanide based materials are studied The first part is focused on the studies on silica based luminescent nanocomposite materials. These materials have been prepared by different ways either by incorporation of the presynthesized lanthanide complexes into the silica pore structures or by the *in situ* synthesis of

low soluble lanthanide complex in the pores of mesoporous silica nanoparticles. The use of ionic liquid as a spectroscopic solvent to study luminescence of the ionic complexes has been explored in the second part of the PhD thesis. In particular, a luminescent soft material was prepared by encapsulating lanthanide complexes into trioctylmethylphosphine ionic liquid.

The problem of limited solubility of highly luminescent europium based scorpionate complex that hampers its incorporation into mesoporous silica nanoparticles is addressed through *in situ* synthesis approach inside the pore structures of nanoparticles. In Chapter 3, a route for europium (III) tris(pyrazol-1-yl)borate complex [$Eu(Tp)_3$] formation inside the pores of mesoporous silica nanoparticles (MSNs) has been established to produce a highly luminescent nanostructured hybrid. Photoluminescence spectroscopy, X-ray diffraction, N_2 adsorption, FTIR spectroscopy, and TEM were used to characterize the material.

In chapter 4, the structural and photophysical properties of the $Eu(dbm)_3phen$ complex encapsulated into functionalized mesoporous silica nanoparticles has been studied in detail. In order to understand the interfacial interactions between the $Eu(dbm)_3phen$ complex and organically modified silica nanoparticles and the effect of these interactions on its photophysical properties, analogous diamagnetic complex $Y(dbm)_3phen$ has been impregnated in organically modified mesoporous silica nanoparticles. The solid state NMR (SSNMR) studies were carried on yttrium/silica nanocomposite in order to understand the structural and dynamic information for these systems which can be extended to the europium/silica composites.

In chapter 5, systematic study was carried out to understand the effect of $Tb(dbm)_3phen$ doping on the luminescence of $Eu(dbm)_3phen$ containing nanoparticles. Two approaches have been used to optimize the luminescence of europium complex doped into MSN. The maximum possible loading concentration of $Eu(dbm)_3phen$ complex has been determined by doping the europium complex alone in the MSN. The MSN nanomaterial containing appropriate ratio and total amount of $Eu(dbm)_3phen$ and $Tb(dbm)_3phen$ has been established through the photoluminescence spectroscopic studies. The material was fully characterized with XRD, TEM, UV-Vis absorption spectroscopy, N_2 adsorption-desorption techniques.

Based on a survey of published work, it appears that imidazolium based ionic liquids have been mostly used as spectroscopic solvents for studying lanthanide compounds. This work was aimed

at the synthesis of new phosphonium based tetrakis anionic lanthanide complexes and the study of their luminescence properties in an asymmetric phosphonium cation based hydrophobic ionic liquid. In chapter 6, Investigations of the properties such as melting point, thermal behavior, FTIR, crystal structure analysis were carried out on new tetrakis lanthanide complexes and their luminescence properties has been studied in solid state as well as in the ionic liquid.

In summary, the scope of this PhD thesis was to study the luminescence properties of lanthanide based silica nanocomposite materials and lanthanide doped ionic liquids as new luminescent soft materials.

1.5. References

[1] S. Shionoya and W. M. Yen, Phosphor Handbook, CRC Press Inc., Boca Raton, FL, 33431, USA, 1999.

[2] Reyes, R.; Cremona, M.; Teotonio, E. E. S.; Brito, H. F, Malta, O. L. Chem. Phys. Lett., 2004, 396, 54-58.

[3] Kido, J.; Okamoto, Y. Chem. Rev., 2002, 102, 2357-2368.

[4] Faulkner, S.; Pope, S. J. A.; Burton-Pye, B. P. Appl. Spectrosc. Rev., 2005, 40, 1-31.

[5] K. Matsumoto and J. G. Yuan, Lanthanide Chelates as Fluorescent Labels for Diagnostics and Biotechnology, Metal Ions in Biological Systems, eds. A. Sigel and H. Sigel, Vol. 40, Ch. 6, Marcel Dekker Inc., New York, 2003.

[6] S. Faulkner and J. L. Matthews, in Comprehense Coordination Chemistry II, ed. M. D. Ward, Elsevier Pergamon, Amsterdam, 2004, Vol. 9, Ch. 9.21, 913-44.

[7] V. W. W. Yam and K. K. W. Lo, Coord. Chem. Rev., 1999, 184, 157.

[8] J.C.G. Bünzli, S. Comby, A.S. Chauvin, C.D.B. Vandevyver, Journal of Rare Earths, 2007, 25, 257-274.

[9] Ken Kuriki, Yasuhiro Koike and, Yoshi Okamoto, Chemical Reviews, 2002, 102, 2347-2356.

[10] J.-C.G. Bünzli, A. Milicic-Tang., Solvation and anion interaction in organic solvents. In Handbook on the Physics and Chemistry of Rare Earths, Karl A. Gschneidner; Eyring, L., Eds. Elsevier, Amsterdam, 1995, 305-366.

[11] Caravan, P.; Ellison, J.J.; Mcmurry, T.J.; Lauffer, R.B., Chemical Reviews, 1999, 99, 2293-352.

[12] Bruce, J.I.; Lowe, M.P.; Parker, D., Photophysical Aspects of Lanthanide(III) Complexes. In The Chemistry of Constrast Agents in Medical Magnetic

Resonance Imaging, Merbach, A.E.; Toth, E., Eds. John Willey & Sons, 2001, 437-460.

[13] J. Becquerel, Compt. Rend. Hebd. Acad. Sci., 1906,142, 775-779.

[14] H. Bethe, Z. Physik, 1930, 60, 218.

[15] H. A. Kramers, Proc. Acad. Sci. Amsterdam, 1930, 32, 1176.

[16] J. Becquerel, Z Physik, 1929, 58, 205.

[17] J. H. van Vleck, J. Chem. Phys., 1937, 41, 67.

[18] Blasse, G.; Grabmaier, B. G. Luminescent Materials; Springer-Verlag: Berlin, Heidelberg, 1994.

[19] G. F. Sa, O. L. Malta, C. D. Donega, A. M. Simas, R. L. Longo, P. A. Santa-Cruz and E. F. SilvaJr, Coord. Chem. Rev., 2000, 196, 165.

[20] Weissman, S. I., The Journal of Chemical Physics, 1942, 10, 214-217.

[21] Whan, R. E.; Crosby, G. A. J. Mol. Spectrosc., 1962, 8, 315.

[22] Crosby, G. A.; Whan, R. E.; Alire, R. M. J. Chem. Phys., 1961, 34, 743.

[23] Crosby, G. A.; Whan, R. E.; Freeman, J. J. J. Phys. Chem., 1962, 66, 2493.

[24] H. F. Brito, O. L. Malta, M. C. F. C. Felinto and E. E. S. Teotonio, in Patai Series: The Chemistry of Metal Enolates, ed. J. Zabicky, John Wiley & Sons Ltd., Chichester, England, 2009, ch. 3, pp. 131-184.

[25] Binnemans, K. In Handbook on the Physics and Chemistry of Rare Earths; Gschneidner, K. A. J., Bünzli, J.-C. G., Pecharsky, V. K., Eds.; Elsevier: Amsterdam, 2005, 35, 107-272.

[26] Melby, L. R.; Rose, N. J.; Abramson, E.; Caris, J. C. J. Am. Chem. Soc., 1964, 86, 5117-5125.

[27] Bauer, H.; Blanc, J.; Ross, D. L. J. Am. Chem. Soc., 1964, 86, 5125-5131.

[28] McGehee, M. D.; Bergstedt, T.; Zhang, C.; Saab, A. P.; O'Regan, M. B.; Bazan, G. C.; Srdanov, V. I.; Heeger, A. J. Adv. Mater., 1999, 11, 1349-1354.

[29] Bünzli, J.-C. G. J. Alloys Compd., 2006, 408-412, 934-944.

[30] V. Bekiari and P. Lianos, Adv. Mater., 1998, 10, 1455.

[31] N. Sabbatini, A. Mecati, M. Guardigli, V. Balazani, J. M. Lehn, R. Zeissel and R. Ungaro, J. Lumin., 1991, 48-49, 463.

[32] N. Sabbatini, M. Guardigli and J. M. Lehn, Coord. Chem. Rev., 1993, 123, 201.

[33] K. Driesen, R. V. Deun, C. Go¨rller-Walrand and K. Binnemans, Chem. Mater., 2004, 16, 1531.

[34] Koen Binnemans, Chem. Rev., 2009, 109, 4283-4374.

[35] Hasegawa, Y.; Ohkubo, T.; Sogabe, K.; Kwamura, Y.; Wada, Y.; Nakashima, N.; Yanagida, S. Angew. Chem. Int. Ed., 2000, 39, 357.

[36] Slooff, L. H.; Polman, A.; Klink, S. I.; Grave, L.; van Veggel, F. C. J. M.; Hofstraat, J. W. J. Opt. Soc. Am. B, 2001, 18, 1690.

[37] Dossing, A. (2005), Eur. J. Inorg. Chem., 1425-1434.

[38] Parker, D., Senanayake, K. and Williams, J. A. G. (1998); J. Chem. Soc. Perkin Trans., 2, 2129-2139.

[39] Dunn, B.; Zink, J. I. J. Mater. Chem. 1991, 1, 903; Reisfeld, R. Opt. Mater., 2001, 16, 1.

[40] Reisfeld, R. J. Fluoresc., 2002, 12, 317.

[41] Reisfeld, R. J. Non-Cryst. Solids, 1990, 121, 254.

[42] Reisfeld, R.; Jørgensen, C. K. Struct. Bonding (Berlin), 1992, 72, 207.

[43] Avnir, D.; Levy, D.; Reisfeld, R. J. Phys. Chem., 1984, 88, 5956.

[44] Avnir, D.; Kaufman, V. R.; Reisfeld, R. J. Non-Cryst. Solids, 1985, 74, 395.

[45] F. Iskandar, I.W. Lenggoro, T.O. Kim, N. Nakao, M. Shimada, K. Okuyama, J. Chem. Eng. Jpn., 2001, 34, 1285.

[46] Y. Piao, A. Burns, J. Kim, U. Wiesner and T. Hyeon, Adv. Funct. Mater., 2008, 18, 3745-3758.

[47] W. Stober, A. Fink and E. Bohn, J. Colloid Interface Sci., 1968, 26, 62-69.

[48] W. Zhou, J. M. Thomas, D. S. Shephard, B. F. Johnson, D. Ozkaya, T. Maschmeyer, R. G. Bell and Q. Ge, Science, 1998, 280, 705.

[49] S. Kim, S. Son, S. I. Lee, T. Hyeon and Y. K. Chung, J. Am. Chem. Soc., 2000, 122, 1550.

[50] C. Wu and T. Bein, Science, 1994, 264, 1757.

[51] K. Kageyama, J. Tamazawa and T. Aida, Science, 1999, 285, 2113.

[52] M. J. MacLachlan, P. Aroca, N. Coombs, I. Manners and G. A. Ozin, Adv. Mater, 1998, 10, 144.

[53] K. Moller and T. Bein, Chem. Mater., 1998, 10, 2950.

[54] S. A. Johnson, D. Khushalani, N. Coombs, T. E. Mallouk and G. A. Ozin, J. Mater. Chem., 1998, 8, 13.

[55] Y. Plyuto, J. Berquier, C. Jacquiod and C. Ricolleau, Chem. Commun., 1999, 1653.

[56] M. Froba, R. Kohn, G. Bouffaud, O. Richard and G. V. Tendeloo, Chem. Mater., 1999, 11, 2858.

[57] J. A. Aggr, M. W. Anderson, M. E. Pemble, O. Terasaki and Y. Nozue, J. Phys. Chem. B, 1998, 102, 3345.

[58] V. I. Srdanov, I. Alxneit, G. D. Stucky, C. M. Reaves and S. P. Denbaars, J. Phys. Chem. B, 1998, 102, 3341.

[59] G. D. Stucky and J. E. MacDougall, Science, 1990, 247, 669.

[60] R. Leon, D. G. Margolese, G. D. Stucky and P. M. Petroff, Phys. Rev. B, 1995, 52, R2285.

[61] X. Feng, G. E. Fryxell, L. Q. Wang, A. Y. Kim, J. Liu and K. M. Kemner, Science, 1997, 276, 923.

[62] P. Chakraborty, J. Mater. Sci., 1998, 33, 2235.

[63] P. Yang, G. Wirnsberger, H. C. Huang, S. R. Cordero, M. D. McGehee, B. Scott, T. Deng, G. M. Whitesides, B. F. Chmelka, S. K. Buratto and G. D. Stucky, Science, 2000, 287, 465.

[64] J. Yu, J.L. Shi, H.R. Chen, J.N. Yan, D.S. Yan, Micropor. Mesopor. Mater., 2001, 46, 153.

[65] A. Katiyar, S. Yadav, P.G. Smirniotis, N.G. Pinto, J. Chromatogr. A, 2006, 13, 1122.

[66] C. J. Brinker, G. W. Scherer, Academic Press, Inc., San Diego, 1990.

[67] Z. A. Qiao, L. Zhang, M. Guo, Y. Liu, Q. Huo, Chem. Mater., 2009, 21, 3823-3829.

[68] Diamente, P. R., Burke, R. D. and Van Veggel, F. C. J. M., Langmuir, 2006, 22, 1782-1788.

[69] Lim, S. F., Riehn, R., Ryu, W. S., Khanarian, N., Tung, C.-K., Tank, D. and Austin, R. H., Nano Lett., 2006, 6, 169-174.

[70] Igor I. Slowing, Brian G. Trewyn, Supratim Giri, and Victor S.-Y. Lin, Adv. Funct. Mater., 2007, 17, 1225-1236.

[71] P. Walden, Bull. Acad. Imper. Sci. (St Petersburg), 1914, 1800.

[72] C. M. Gordon, Appl. Catal. A, 2001, 222, 101.

[73] Wasserscheid, P.; Welton, T. Ionic Liquids in Synthesis; Wiley-VCH, Weinheim: New York, 2003.

[74] Welton, T., Chem.Rev., 1999, 99, 2071-2084.

[75] M. Freemantle. Chem. Eng. News, 1998, 76, 32-37.

[76] Holbrey, J. D.; Seddon, K. R. Clean Prod. Process., 1999, 1, 223-236.

[77] Wilkes, J. S.; Zaworotko, M. J. Chem. Soc., Chem. Commun., 1992, 965-967.

[78] MacFarlane, D. R.; Meakin, P.; Sun, J.; Amini, N.; Forsyth, M. J. Phys. Chem. B, 1999, 103, 4164-4170.

[79] Sun, J.; Forsyth, M.; MacFarlane, D. R. J. Phys. Chem. B, 1998, 102, 8858-8864.

[80] Matsumoto, H.; Yanagida, M.; Tanimoto, K.; Nomura, M.; Kitagawa, Y.; Miyazaki, Y. Chem. Lett., 2000, 922-923.

[81] Matsumoto, H.; Matsuda, T.; Miyazaki, Y. Chem. Lett., 2000, 1430-1431.

[82] Holbrey, J. D.; Seddon, K. R. J. Chem. Soc., Dalton Trans., 1999, 2133-2139.

[83] Bonhoˆte, P.; Dias, A.-P.; Papageorgiou, N.; Kalyanasundaram, K.; Gra¨tzel, M. Inorg. Chem., 1996, 35, 1168-1178.

[84] J. Dupont, P. A. Z. Suarez, Phys. Chem. Chem. Phys., 2006, 8, 2441.

[85] Bradley AE, Hardacre C, Holbrey JD, Johnston S, McMath SEJ, Nieuwenhuyzen M., Chem Mater, 2002, 14, 629.

[86] Ngo HL, LeCompte K, Hargens L, McEwen AB., Thermochim Acta, 2000, 97, 357

[87] K. R. Seddon. In Molten Salt Forum: Proceedings of 5th International Conference on Molten Salt Chemistry and Technology, Vol. 5-6, H. Wendt (Ed.), 1998, 53-62.

[88] R. D. Rogers, K. R. Seddon, Eds., Ionic Liquids as Green Solvents: Progress and Prospects (ACS Symp. Ser. 856, American Chemical Society, Washington, DC, 2003).

[89] R. D. Rogers, K. R. Seddon, Eds., Ionic Liquids: Industrial Applications for Green Chemistry (ACS Symp. Ser. 818, American Chemical Society, Washington, DC, 2002).

[90] A. E. Visser, R. P. Swatloski and R. D. Rogers, Green Chem., 2001, 2, 1.

[91] Ann E. Visser, Richard P. Swatloski and Robin D. Rogers, Green Chem., 2000, 2, 1-4.

[92] Jonathan G. Huddleston and Robin D. Rogers, Chem. Commun., 1998, 1765-1766.

[93] Wassersheid, P.; Keim, W. Angew. Chem., Int. Ed., 2000, 39, 3772-3789.

[94] J. Dupont, R. F. de Souza, P. A. Z. Suarez, Chem. Rev., 2002, 102, 3667.

[95] D. B. Zhao, M. Wu, Y. Kou, E. Z. Min, Catal. Today, 2002, 74, 157.

[96] T. Welton, Coord. Chem. Rev., 2004, 248, 2459.

[97] V. I. Paˆrvulescu, C. Hardacre, Chem. Rev., 2007, 107, 2615.

[98] Ionic Liquids in Synthesis, 2nd ed. (Eds: P. Wasserscheid, T. Welton), Wiley-VCH, Weinheim 2008.

[99] Ionic Liquids in Synthesis, 2nd ed. (Eds.: P. Wasserscheid, T. Welton), Wiley-VCH, Weinheim, 2007.

[100] C. D. Liang, C. Y. Yuan, R. J. Warmack, C. E. Barnes, S. Dai, Anal. Chem., 2002, 74, 2172.

[101] J. F. Huang, H. M. Luo, C. D. Liang, D. E. Jiang, S. Dai, Ind. Eng. Chem. Res., 2008, 47, 881.

[102] H. Ohno, Ed., Ionic Liquids: The Front and Future of Material Developments (CMC, Tokyo, 2003).

[103] Koch, V. R.; Nanjundiah, C.; Appetecchi, G. B.; Scrosati, B. J. Electrochem. Soc., 1995, 142, L116-L118.

[104] Sakaebe, H.; Matsumoto, H. Electrochem. Commun., 2003, 5, 594-598.

[105] Koch, V. R.; Dominey, L. A.; Nanjundiah, C.; Ondrechen, J. J. Electrochem. Soc., 1996, 143, 798-803.

[106] Nanjundiah, C.; McDevitt, S. F.; Koch, V. R. J. Electrochem. Soc., 1997, 144, 3392-3397.

[107] Ue, M.; Takeda, M.; Toriumi, A.; Kominato, A.; Hagiwara, R.; Ito, Y. J. Electrochem. Soc., 2003, 150, A499-A502.

[108] Papageorgiou, N.; Athanassov, Y.; Armand, M.; Bonhoˆte, P.; Pettersson, H.; Azam, A.; Gra¨tzel, M. J. Electrochem. Soc., 1996, 143, 3099-3108.

[109] Kawano, R.; Watanabe, M. Chem. Commun., 2003, 330-331.

[110] Kawano, R.; Matsui, H.; Matsuyama, C.; Sato, A.; Susan, M. A. B. H.; Tanabe, N.; Watanabe, M. J. Photochem. Photobiol. A, Chem., 2004, 164, 87-92.

[111] Doyle, M.; Choi, S. K.; Proulx, G. J. Electrochem. Soc., 2000, 147, 34-37.

[112] Noda, A.; Susan, M. A. B. H.; Kudo, K.; Mitsushima, S.; Hayamizu, K.; Watanabe, M. J. Phys. Chem. B, 2003, 107, 4024-4033.

[113] Susan, M. A. B. H.; Noda, A.; Mitsushima, S.; Watanabe, M. Chem. Commun., 2003, 938-939.

[114] Lu, W.; Fadeev, A. G.; Qi, B.; Smela, E.; Mattes, B. R.; Ding, J.; Spinks, G. M.; Mazurkiewicz, J.; Zhou, D.; Wallace, G. G.; MacFarlane, D. R.; Forsyth, S. A.; Forsyth, M. Science, 2002, 297, 983-987.

[115] R. A. Sheldon, R. M. Lau, M. J. Sorgedrager, F. van Rantwijk, K. R. Seddon, Green Chem., 2002, 4, 147.

[116] A. Taubert, Acta Chim. Slov., 2005, 52, 183.

[117] M. Antonietti, D. Kuang, B. Smarsly, Y. Zhou, Angew. Chem., 2004, 116, 5096.

[118] Markus Antonietti, Daibin Kuang, Bernd Smarsly and Yong Zhou, Angew. Chem. Int. Ed., 2004, 43, 4988-4992.

[119] C. M. Gordon and A. J. McLean, Chem. Commun., 2000, 1395.

[120] A. Bösmann, L. Datsevich, A. Jess, A. Lauter, C. Schmitz and P. Wasserscheid, Chem. Commun., 2001, 2494.

[121] R. Sheldon, Chem. Commun., 2001, 2399.

[122] G. Gamero-Castaño and V. Hruby, J. Propulsion Power, 2001, 5, 977.

[123] B. Wu, R. G. Reddy and R. D. Rogers, Sol. Eng., 2001, 445.

[124] Wilkes, J. S.; et al. Inorg. Chem., 1982, 21, 1263-1264.

[125] Armand A. Fannin, Jr., Lowell A. King, Joseph A. Levisky, and John S. Wilkes, Journal of Physical Chemistry, 1984, 88, 1984.

[126] Chowdhury, P. K.; Halder, M.; Sanders, L.; Calhoun, T.; Anderson, J. L.; Armstrong, D. W.; Song, X.; Petrich, J. W. J. Phys. Chem. B, 2004, 108, 10245-10255.

[127] Chakrabarty, D.; Hazra, P.; Chakraborty, A.; Seth, D.; Sarkar, N. Chem. Phys. Lett., 2003, 381, 697-704.

[128] Arzhantsev, S.; Jin, H.; Ito, N.; Maroncelli, M. Chem. Phys. Lett., 2006, 417, 524-529.

[129] Mandal, P. K.; Paul, A.; Samanta, A. Res. Chem. Intermed., 2005, 31, 575-583.

[130] Gaillard, C.; Billard, I.; Chaumont, A.; Mekki, S.; Ouadi, A.; Denecke, M. A.; Moutiers, G.; Wipff, G. Inorg. Chem., 2005, 44, 8355-8367.

[131] Samikkanu, S.; Mellem, K.; Berry, M.; May, P. S. Inorg. Chem., 2007, 46, 7121-7128.

[132] Billard, I.; Mekki, S.; Gaillard, C.; Hesemann, P.; Moutiers, G.; Mariet, C.; Labet, A.; Bünzli, J.-C. G. Eur. J. Inorg. Chem., 2004, 1190-1197.

[133] Binnemans, K. Chem. Rev., 2007, 107, 2592-2614.

[134] Dai, S.; Shin, Y. S.; Toth, L. M.; Barnes, C. E. Inorg. Chem. 1997, 36, 4900-4902

[135] Nikitenko, S. I.; Cannes, C.; Le Leaour, C.; Moisy, P.; Trubert, D. Inorg. Chem., 2005, 44, 9497-9505.

[136] Servaes, K.; Hennig, C.; Billard, I.; Gaillard, C.; Binnemans, K.; Görller-Walrand, C.; Van Deun, R. Eur. J. Inorg. Chem., 2007, 5120-5126.

[137] Hopkins, T. A.; Berg, J. M.; Costa, D. A.; Smith, W. H.; Dewey, H. J. Inorg. Chem., 2001, 40, 1820-1825.

[138] Nockemann, P.; Servaes, K.; Van Deun, R.; Van Hecke, K.; Van Meervelt, L.; Binnemans, K.; Görller-Walrand, C. Inorg. Chem., 2007, 46, 11335-11344.

[139] Denise Appleby, Charles L. Hussey, Kenneth R. Seddon, Janet E. Turp, Nature, 1986, 323, 614-616.

[140] Christine J. Bradaric , Andrew Downard , Christine Kennedy , Allan J. Robertson and Yuehui Zhou, Green Chemistry, 2003, 5, 143-152.

[141] A. G. Avent, P. A. Chaloner, M. P. Day, K. R. Seddon and T. Welton, J. Chem. Soc., Dalton Trans., 1994, 3405.

[142] Wei-Jyh Gau and I-Wen Sun, J. Electrochem. Soc., 1996, 143, 914-919.

[143] A. Chaumont and G. Wipff, Inorganic Chemistry, 2009, 48, 4287.

[144] Koen Binnemans, Chem. Rev., 2007, 107, 2592-2614.

[145] Jean-Claude G. Bünzli and Claude Piguet, Chem. Soc. Rev., 2005, 34, 1048-1077.

[146] Alain Chaumont, Georges Wipff Prof., Chem. Eur. J., 2004, 10, 3919-3930.

[147] A. Chaumont and G. Wipff, Phys. Chem. Chem. Phys., 2005, 7, 1926-1932.

[148] Alain Chaumont and Georges Wipff, J. Phys. Chem. B, 2004, 108, 3311-3319.

[149] Nagaishi, R.; Arisaka, M.; Kimura, T.; Kitatsuji, Y. J. Alloys Compd., 2007, 431, 221-225.

[150] E. Guillet, D. Imbert, R. Scopelliti, J.-C. BNnzli, Chem. Mater., 2004, 16, 4063.

[151] P. Nockemann, E. Beurer, K. Driesen, R. Van Deun, K Van Hecke, L. Van Meervelt, K. Binnemans, Chem. Commun., 2005, 4354-4356.

[152] Puntus, L. N.; Schenk, K. J.; Bünzli, J.-C. G. Eur. J. Inorg. Chem., 2005, 4739-4744.

[153] K. Driesen, P. Nockemann, K. Binnemans, Chem. Phys. Lett., 2004, 395, 306.

[154] S. Arenz, A. Babai, K. Binnemans, K. Driesen, R. Giernoth, A.-V. Mudring, P. Nockemann, Chem. Phys. Lett., 2005, 402, 75.

[155] N. Karodia, S. Guise, C. Newlands, J. Andersen, Chem. Commun., 1998, 2341.

[156] D.E. Kaufmann, M. Nouroozian, H. Henze, Chem. Syn. Lett., 1996, 1091.

[157] J. McNulty, A. Capretta, J. Wilson, J. Dyck, G. Adjabeng, A. Robertson, Chem., Commun., 2002, 1986-1987.

Chapter-2

Instrumentation, Procedures, Materials and Synthesis

2.1. Instrumentation

2.1.1. UV/VIS spectroscopy

UV-visible spectra of solutions were recorded with a Agilent diode array spectrometer 8453 using a 1 mm quartz cell. Diffuse reflectance UV-visible spectra (DRS) were recorded at room temperature on a JASCO V-570 spectrophotometer equipped with an integrating sphere and $BaSO_4$ was used as reference. The Kubelka-Munk function $F(R) = (1-R)^2/2R$ was obtained from reflectance to approximate the optical absorbance.

2.1.2. Luminescence spectroscopy

Photoluminescence measurements were performed with a Fluorolog 3-21 system (Horiba Jobin Yvon). A 450 W xenon arc lamp was used as a broadband excitation source and a double Czerny-Turner monochromator was used to select the excitation wavelength for photoluminescence excitation. All emission spectra were obtained using the same amount of powder, measured at room temperature and recorded under the same conditions.

The analysis of the emitted luminescence signal from the samples was performed by using a iHR320 single grating monochromator and a R928 Hamamatsu PMT for the visible range, while R5509 Hamamatsu PMT for the near infrared range. The excitation spectra were recorded in the 250–450 nm range with 1 nm band pass resolution, dividing the PMT signal by the intensity of

the lamp, measured by using a calibrated photodetector. On the other hand, the emission spectra were recorded in the 550-750 nm range with 1 nm band-pass resolution and corrected for the response of the instrument, keeping into account the wavelength dependent efficiencies of the optical elements and detectors.

Time resolved characterization was obtained by exciting the sample with a SpectraLED-03 laser diode, providing a 377 nm excitation; with 12 nm spectral bandwidth. The excitation pulse duration was set at 5 ms and the photoluminescence decay was acquired for about 20 ms, which was sufficient to allow the signal going to zero. These measurements were obtained by working in multi channel single photon counting (MCSPC) mode.

2.1.3. Solid State NMR Spectroscopy (SSNMR)

All the experiments were performed on a double-channel Varian Infinity Plus 400 spectrometer working at 400.02 MHz for hydrogen-1, 79.47 MHz for silicon-29 and 100.59 MHz for carbon-13, equipped with either a 7.5 mm or a 3.2 mm Cross-Polarization Magic Angle Spinning (CP-MAS) probe head.

High-resolution experiments on $Y(dbm)_3phen$ complex and modified MSNs were performed on the 7.5 mm CP-MAS probe head, with ^{1}H and ^{13}C 90 degree pulse durations of 5 μs. For the ^{29}Si and ^{13}C CP spectra, 50000 and 10000 transients were accumulated, respectively, and a contact time of 1 ms and a relaxation delay of 5 s were used.

Experiments on composites were performed on the 3.2mm CP-MAS probe head with ^{1}H and ^{13}C 90 degree pulse durations of 2.5 μs. ^{13}C CP spectra were recorded accumulating 25000 transients and using a, contact time of 1 ms and a recycle delay of 3 s.

^{13}C direct excitation (DE) MAS spectra were recorded with a recycle delay of 2 s in order to select signals arising from ^{13}C nuclei with short spin-lattice relaxation times (T_1), accumulating 20000-25000 transients.

Proton T_1's were measured under low-resolution conditions by using a saturation recovery pulse sequence and accumulating 32 transients for each delay.

^{13}C T_1 measurements were performed by the Torchia pulse sequence[1] accumulating about 1500 transients for each delay.

All the measurements were performed at 25 °C unless otherwise stated. Temperatures were controlled within ±0.4 °C. Air was used as either spinning or heating gas.

2.1.4. Nitrogen physisorption measurements

Nitrogen adsorption–desorption measurements were performed at liquid nitrogen temperature (-196 °C) with an ASAP 2010 apparatus from Micromeritics. The analysis procedure is fully automated and operates with the static volumetric technique. Before each measurement, the samples (100 mg) were out gassed at 130 °C for 12 h at 5 $\times 10^{-3}$ Torr and then at room temperature for 2 h at 0.75 $\times$ 10^{-6} Torr. The N_2 isotherms were used to determine the specific surface areas by using the BET equation,[2] micropore volume, using t-plot and the specific pore volume (Vs), calculated at P/P0 = 0.98. The pore-size distribution was calculated following the BJH method,[3] assuming a cylindrical pore model.

2.1.5. CH-Elemental Analysis

Elemental analyses were performed with a Perkin–Elmer 2400 CHN microanalyser at the University of Padova, Italy.

2.1.6. Single crystal X-Ray structure determination

Data collections were performed at the X-ray diffraction beamline (XRD1) of the Elettra Synchrotron, Trieste (Italy) with a Pilatus 2M image plate detector. Complete datasets have been collected at a monochromatic wavelength of 0.6526 Å through the rotating crystal method. The crystals of compounds were dipped in N-paratone and mounted on the goniometer head with a nylon loop. The diffraction datasets were collected at 100 K, using a nitrogen stream supplied through an Oxford Cryostream 700. The diffraction data were indexed and integrated using XDS,[4] and scaled with SCALA. The structures were solved by direct methods using SIR2011,[5] Fourier analyzed and refined by the full-matrix least-squares based on F2 implemented in SHELXL-97.[6] Coot program has been used for modeling.[7] Empirical absorption correction has been applied as implemented in the XABS2 program.[8] Anisotropic thermal motion modeling was then applied to atoms with full occupancy and occupancy greater than 80%. In the final

refinement, all non-hydrogen atoms were treated anisotropically and the hydrogen atoms were included at calculated positions with isotropic Ufactors = 1.2 Ueq.

2.1.7. Powder X-Ray Diffraction

X-ray diffraction analyses were performed on disc shaped pressed powdered samples using a Philips X'Pert vertical goniometer with Bragg–Brentano geometry, connected to a highly stabilized generator. A focusing graphite monochromator and a proportional counter with a pulse-height discriminator were used. Nickel-filtered Cu Kα radiation and a step-by-step technique were employed (steps of 0.05° 2θ), with collection times of 10 s/step. The size of the crystallites was evaluated by line broadening analysis (LBA) using our previously published method.[9]

2.1.8. Thermal analysis (TGA)

Thermogravimetric analysis (TGA) was performed with Netzsch STA 409 instrument using alumina as the inert standard TGA analyses were carried out within a temperature between 40 °C to 1000 °C, and with the heating rate of 10 °C min^{-1}, and an air to N_2 flow ratio of 1:2 (40:80 mL min^{-1}).

2.1.9. Transmission Electron Microscope (TEM)

TEM images were taken with a JEOL 3010, operating at 300 kV, equipped with a GATAN (Warrendale, PA, USA) multi-scan CCD camera. TEM specimens were prepared by ultrasonically dispersing the powdered samples in ethanol (approximately 10 mg mL^{-1}) and depositing several drops of the suspension on a holey carbon film supported by a copper grid.

2.1.10. Energy-dispersive X-ray spectroscopy (EDS)

EDS spectra were recorded by Oxford EDS microanalysis detector equipped on JEOL 3010 system.

2.1.11. Fourier Transform Infrared Spectroscopy (FTIR)

Infrared spectra were recorded by using a Thermo Nicolet Magna IR™ spectrometer in the range 4000 - 400 cm^{-1} at a resolution of 2 cm^{-1} in KBr background using diffuse reflectance infrared Fourier transform (DRIFT) spectroscopy.

2.1.12. Raman Spectroscopy

Raman spectra were recorded with a Renishaw inVia microRaman spectrometer using a 50x magnification and the 633 nm line of a He-Ne laser as exciting line.

2.1.13. Nuclear Magnetic Resonance Spectroscopy (NMR)

^{1}H and ^{13}C NMR spectra were recorded on a Varian Unity Spectrometer (400 MHz). The spectra are recorded in deuterated chloroform ($CDCl_3$). All chemical shifts are given in ppm with respect to tetramethylsilane (TMS).

2.2. Procedures

2.2.1. Luminescence decay times

The decay curves were fitted with the least squares method, by using a monoexponential or a biexponential equation. In all cases, χ^2 values close to 1 confirmed the high quality of the fitting procedure. Standard quartz 1 cm fluorescence cuvets were used for liquid samples. Luminescence lifetime data were extracted from the decay curves using the program Origin software.

2.2.2. Quantum yield determination

Quantum efficiency values for the lanthanide complex containing samples were obtained by using an integrating sphere coupled to the same Fluorolog-3 system and by measuring the rate between the number of emitted photons and the number of absorbed photons.

2.2.3. Density determination

The absolute densities of the lanthanide complexes were determined by using Micromeritics Multivolume Pycnometer 1305.

2.3. Materials

Tetraethyl orthosilicate (TEOS, Aldrich, 98%)

Hexadecyl-trimethylammonium bromide (CTAB, Aldrich)

Europium trichloride hexahydrate ($Eu{\cdot}Cl_3{\cdot}6H_2O$, Aldrich, 99.9%)

Samarium trinitrate hexahydrate ($Sm{\cdot}(NO_3)_3{\cdot}6H_2O$, 99.9%, Aldrich)

Terbium trichloride hexahydrate ($Tb{\cdot}Cl_3{\cdot}6H_2O$, Aldrich, 99.9%)

Yttrium trichloride hexahydrate ($Y{\cdot}Cl_3{\cdot}6H_2O$, Aldrich, 99.99%)

Sulphuric acid (Carlo Erba, 96%)

Sodium hydroxide (Sigma-Aldrich, 98%)

Ammonium hydroxide solution (Fluka, 28 wt% in water)

Hydrogen peroxide (Sigma-Aldrich, 30%)

n-propylamine (Aldrich, 99%)

Tri-n-octylphosphine (TOP, 97%, Aldrich),

Dimethyl carbonate [DMC, ≥99%, Sigma–Aldrich]

(trifluoromethane)sulfonimide lithium salt bis(trifluoromethane)sulfonimide lithium salt (99.95%, Aldrich), [$LiNTf_2$]

Potassium borohydride [99.9% Aldrich]

Pyrazole [98%, Aldrich]

(3-aminopropyl)-triethoxysilane (APTES, Aldrich, 99%)

(3-Mercaptopropyl)-trimethoxysilane (MPTMS, Aldrich, 95%)

Ethoxytrimethylsilane (ETMS, Aldrich, 98%)

1,10 phenanthroline (phen, Aldrich, 99%)

Dibenzoylmethane (dbm, Aldrich, 98%)

Dichloromethane (Carlo Erba, 99.5%)

Absolute ethanol (99.8%, Carlo Erba)

Hexane (Carlo Erba)

Cyclohexane (Fluka, 99%)

Toluene (Fluka, 99%)

Distilled water

All the reagents and solvents were used as received.

2.4. Synthesis

2.4.1. Synthesis of mesoporous silica nanoparticles (MSNs)

Mesoporous silica nanoparticles were prepared according to the method by Qiao et al.[10] To a 500 mL round bottom flask was added 128 mL distilled water, 22.8 mL ethanol, 5.73 g CTAB previously dissolved in 17.2 mL water, and 1.25 mL 28% ammonia solution. The reaction contents were stirred at 60 ^{o}C for 30 min, followed by the addition of 14.6 mL TEOS. Stirring was continued for an additional two hours at 60 ^{o}C. The obtained solid was recovered by repeated centrifugation (20 min at 9000 rpm) and sonication (30 min) by washing once with distilled water and three times with ethanol. The solid was dried under reduced pressure (10^{-1} mbar for 1 h) and calcinated at 600 ^{o}C for 6 h to remove the templating surfactant from the pores.

2.4.2. Ionic liquids

Phosphonium ionic liquids were synthesized using procedure reported by Perosa et al.[11]

2.4.2.1.[TOMP][CH_3OCOO]

TOP (25 mL, 20.8 g, 56 mmol), DMC (30 mL, 32.1 g, 356 mmol) and methanol (30 mL) were combined (two phases) in a sealed 200 mL steel autoclave fitted with a pressure gauge and a thermocouple for temperature control. Three freeze–pump–thaw cycles were carried out to ensure complete degassing of the mixture and air removal. The empty volume was then filled with nitrogen. The autoclave was heated for 20 h at 140 C with magnetic stirring, after which time it was cooled and vented. Methanol and residual DMC were removed from the mixture by rotary evaporation, to give [TOMP][CH_3OCOO] (27.5 g, 100%) as a viscous clear colourless

liquid. ^{1}H NMR (neat, 60 °C, 400 MHz, [D_6] DMSO): δ = 3.15 (s, 3H; C*H*$_3$OCOO), 2.33 (br t, 6H; P-C*H*$_2$), 1.88 (d, *J*(P,H) = 14 Hz, 3H; P-C*H*$_3$), 1.42 (br, 6H), 1.27 (br, 6H), 1.11 (br, 24H), 0.70 ppm (br t, 9H); ^{13}C{^{1}H} NMR (neat, 60 °C, 100 MHz, [D_6]DMSO, CH_2 assigned by 2D INADEQUATE): δ = 155.8 (1 C; C=O), 50.0 (1 C; *C*H$_3$ O), 30.9 (3 C; C_6), 29.9 (d, *J*(P,C)=15 Hz, 3 C; C_3), 28.2 (3 C; C_5), 28.0 (3 C; C_4), 21.6 (3 C; C_7), 20.7 (d, *J*(P,C)=4 Hz, 3 C; C_2), 19.0 (d, *J*(P,C)=48 Hz, 3 C; C_1), 12.8 (3 C; C_8), 2.6 ppm (d, *J*(P,C)= 53 Hz, 3 C; P-*C*H$_3$); FTIR (neat): 2900, 2856, 1669 cm^{-1}.

2.4.2.2.[TOMP][NTf$_2$]

The [TOMP][NTf_2] ionic liquid was prepared by a metathesis reaction between [TOMP][CH_3OCOO] IL (8.0 g, 16.26 mmol) and Bis(trifluoromethane)sulfonimide lithium salt [$LiNTf_2$] (4.66 g, 16.26 mmol) in water. The mixture was stirred at 70 °C for 2 h. The resulting white precipitate was extracted with CH_2Cl_2 and the solvent was removed under reduced pressure to afford pure, and dry [TOMP][NTf_2] as a clear liquid. (6.10 g, 60%) ^{1}H NMR (neat, 60 °C, 400 MHz, [D_6]DMSO): δ = 1.96 (br, 6H; P-CH_2), 1.55 (d, *J*(P,H) = 13 Hz, 3H; P-CH_3), 1.34 (br, 6 H), 1.24 (br, 6 H), 1.09 (br, 24H), 0.68 ppm (br t, 9H); ^{13}C{^{1}H} NMR (neat, 60 °C, 100 MHz, [D_6]DMSO): d=119.1 (q, *J*(F,C)=321 Hz, 2C; *C*F_3), 30.6 (3C; C_6), 29.3 (d, *J*(P,C) = 15 Hz, 3C; C_3), 27.8 (3C; C_5), 27.5 (3C; C_4), 21.4 (3C; C_7), 20.2 (d, *J*(P,C)=5 Hz, 3C; C_2), 19.0 (d, *J*(P,C)=48 Hz, 3C; C_1), 12.6 (3C; C_8), 2.3 ppm (d, *J*(P,C)=52 Hz, 3C; P-*C*H$_3$); FTIR (neat): = 2930, 2859, 1468, 1352 cm^{-1}.

2.4.2.3.[TOMP][DBM]

To a 50 mL round bottomed flask was added [DBM] (2.27 g. 10.14 mmol) and [TOMP][CH_3OCOO] (5 g. 10.14 mmol). The mixture was stirred at RT for 2 h. It was then stirred under high vacuum to eliminate co-products such as MeOH and CO_2 formed during the reaction. FTIR: 3055, 3028, 2955, 2925, 2854, 2731, 1608, 1565, 1493, 1465, 1431, 722.

2.4.3. Potassium hydrotris(pyrazol-1-yl)borate K[Tp]

Potassium hydrotris(pyrazol-1-yl)borate K[Tp] was prepared according to the literature method[12] by reacting potassium borohydride with pyrazole.

2.4.4. Lanthanide complexes

2.4.4.1.Synthesis of europium tris(pyrazolylborate) complex [Eu(Tp)$_3$][13]

$EuCl_3 \cdot 6H_2O$ (0.086 g 0.235 mmol) was dissolved in distilled water (10 mL) with stirring. K[Tp] (0.182 g 0.721 mmol), pre-dissolved in distilled water (5 mL), was added to the stirring solution. A white precipitate formed and was recovered by filtration. The obtained powder was washed firstly with water, then ethanol (10 mL), and finally it was dried under reduced pressure to give a white solid of the pure complex with a yield of 46 % (0.086 g) (scheme 2.1).

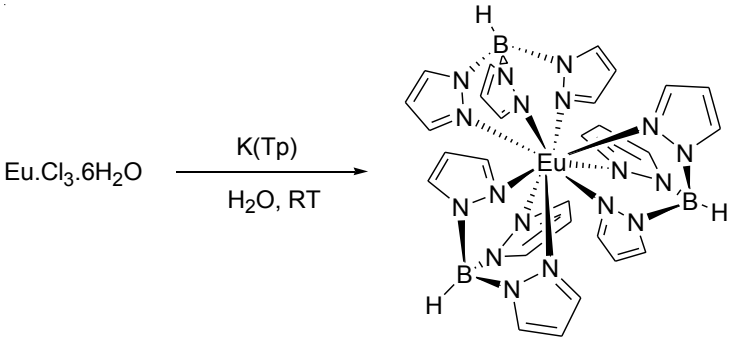

Scheme 2.1 Synthesis of the europium tris (pyrazolylborate) complex [Eu(Tp)$_3$]

2.4.4.2.Synthesis of Ln(dbm)$_3$phen complexes

Eu(dbm)$_3$phen has been synthesized by the method reported earlier[14] with some modifications. A solution of dibenzoylmethane (2.21 g, 9.8 mmol), 1,10 phenanthroline (0.593 g, 3.29 mmol), and NaOH (0.4 g, 9.88 mmol) in ethanol (35 mL) was warmed (60 ^{o}C) with stirring for two hours. $Eu.Cl_3.6H_2O$ (1.205 g, 3.29 mmol) was dissolved in distilled water (3 mL) and added drop-wise to the above solution resulting into precipitation of complex Eu(dbm)$_3$phen. The crude product was suspended in dichloromethane and centrifuged (2 X 9000 rpm / 30 min) to remove the formed NaCl. Solvent was removed under reduced pressure and the Eu(dbm)$_3$phen complex was recovered as a yellow powder.

Tb(dbm)$_3$phen was prepared as above substituting $Eu \cdot Cl_3 \cdot 6H_2O$ by $Tb \cdot Cl_3 \cdot 6H_2O$.

Tris(dibenzoylmethane)(monophenanthroline)yttrium(III) [Y(dbm)$_3$phen] was prepared by using the same procedure as that of Eu(dbm)$_3$phen substituting $Eu \cdot Cl_3 \cdot 6H_2O$ by $Y \cdot Cl_3 \cdot 6H_2O$. The

$Eu(dbm)_3phen$, $Tb(dbm)_3phen$ and $Y(dbm)_3phen$ complexes are shown schematically in figure 2.1.

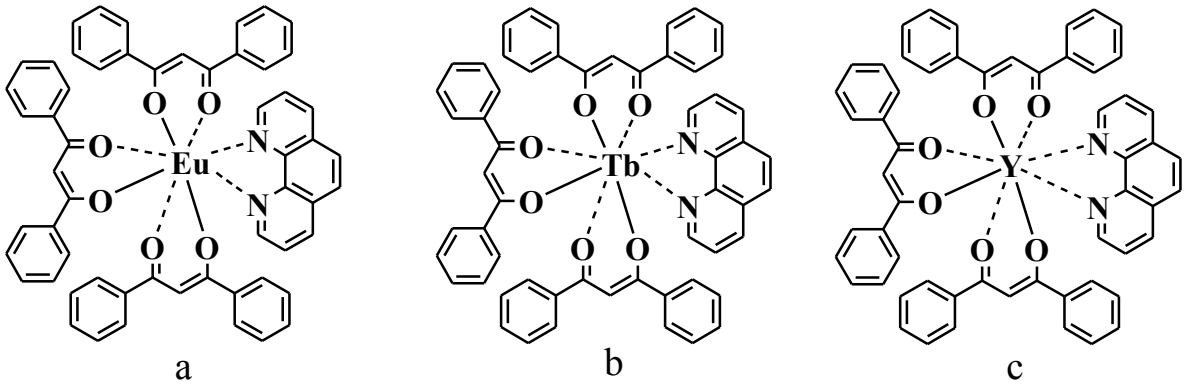

Figure 2.1: Molecular structure of the $Eu(dbm)_3phen$, (a) $Tb(dbm)_3phen$, (b) and $Y(dbm)_3phen$ (c) complexes.

2.4.4.3.TOMP[Eu(dbm)$_4$]

An aqueous solution (6 mL) of $Eu.Cl_3.6H_2O$ (0.57 g. 1.58 mmol) was added dropwise to [TOMP][dbm] (3.88 g. 6.32 mmol) in ethanol (10 mL). The reaction mixture was stirred for 2 h; precipitated complex was filtered and dried under high vacuum (10^{-1} mbar/1 h). The crystals of TOMP[Eu(dbm)$_4$] were suitable for single-crystal X-ray structure determination (scheme 2.2). ($C_{85}H_{98}EuO_8P$: Mr: 1430.62) (Scheme 2) Yield (1.56g, 69%). MP: 190-206 °C FTIR: 3060 (νs(C-H)ar, 3029, 2954, 2925, 2856 (νs(C-H); 1957, 1896; 1600, 1552, 1515 (νs(C-O); 1470, 1425, 1310 νs(C-O···M); 1280, 1220; 1180 (νs(C-P); 1066 (νs(C-O); 1030 ν(Ring deformation), 940, 780, 720 cm^{-1}, Raman: 1595 (ν(C=C)ar; 1556; 1488, 1443 w (ν(C=C)ar; 1309 s (ν(C-H)ar; 1274, 1178; 1059, 1000 (Ring deformation); 940, 788, 682 (Ring deformation); 617, 460 m (ν(Eu-O); 240, 190 ν(Eu-O chelate ring deformation); 133, MP: 109-206 °C. Anal. Calcd: C, 71.2 %; H, 6.85 %. Found: C, 69.94 %; H, 6.70 %.

2.4.4.4.TOMP[Sm(dbm)$_4$]

An aqueous solution (6 mL) of $Sm(NO_3)_3.6H_2O$ (0.96 g. 2.16 mmol) was added dropwise to [TOMP][dbm] (5.263 g. 8.64 mmol) in ethanol (6 mL). The reaction mixture was stirred for 2 h; precipitated complex was filtered, washed with ice-cold water and the sticky solid was first dried under reduced pressure (10^{-1} mbar/4h) and crystallized from ethanol (2.59g, 84%) (Scheme 2.2).

The complex showed red/orange luminescence under the UV lamp (366 nm). ($C_{85}H_{98}SmO_8P$: Mr: 1429.016) M.P.: 236 – 249.8 °C; FTIR (KBr): = 3062, 2927, 2854 (C-H), 1760 (C=O), 1616, 1596, 1554, 1515, 1465, 1423, 1307, 1276, 1218, 1176, 1068 (C-P), 1025, 941, 717, 690 cm-1; Raman: 1595, 1488, 1443, 1312, 1274, 1179, 1060, 997, 938, 785, 670, 617, 402, 241, 196, 127. Anal. Calcd: C, 71.37; H, 6.85 %,. Found: C, 71.35 %; H, 6.80.

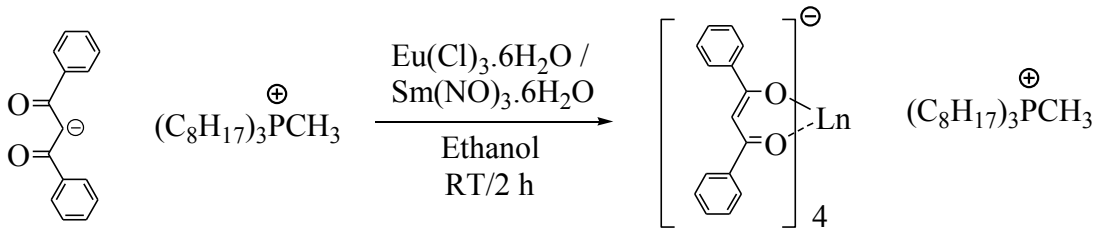

Ln = Eu (I), Sm (II)

Scheme 2.2: reaction scheme of the formation of [TOMP][Eu(dbm)$_4$] **(I)** and [TOMP][Sm(dbm)$_4$] **(II)**.

2.4.5. References

[1] Torchia, D.A. J.Magn.Reson., 1979, 30, 613-616

[2] Brunauer, S.; Emmett, P. H.; Teller, E. J. Am. Chem. Soc., 1938, 60, 309-319

[3] Barrett, E. P.; Joyner, L. G.; Halenda, P. P. J. Am. Chem. Soc., 1951, 73, 373-380

[4] W. Kabsch, Acta Cryst. D, 2010, 66, 125-132

[5] M. C. Burla, R. Caliandro, M. Camalli, B. Carrozzini, G. L. Cascarano, C. Giacovazzo, M. Mallamo, A. Mazzone, G. Polidori, R. Spagna, J. Appl. Cryst., 2012, 45, 357-361

[6] G. M. Sheldrick, T. R. Schneider, Methods Enzymol., 1997, 277, 319-343

[7] P. Emsley, K. Cowtan, Acta Cryst. D, 2004, 60, 2126-2132

[8] S. Parkin, B. Moezzi, H. Hope, J. Appl. Cryst., 1995, 28, 53-56

[9] S. Enzo, S. Polizzi, A. Benedetti, Z Kristallogr, 1985, 170, 275-287

[10] Z. A. Qiao, L. Zhang, M. Guo, Y. Liu, Q. Huo, Chem. Mater., 2009, 21, 3823-3829

[11] Massimo Fabris, Vittorio Lucchini, Marco Noè, Alvise Perosa, Maurizio Selva, Chem. Eur. J., 2009, 15, 12273-12282

[12] S. Trofimenko, J. Am. Chem. Soc., 1967, 89, 3170-3177

[13] K. W. Bagnall, A. C. Tempest, J. Takats, A. P. Masino, Inorg. Nucl. Chem. Lett., 1976, 12, 555-557

[14] L. R. Melby, N. J. Rose, E. Abramson, J. C. Caris, J. Am. Chem. Soc., 1964, 86, 5117-5125

Chapter 3

In situ synthesis of highly luminescent scorpionate complex [Eu(Tp)$_3$] inside the pores of mesoporous silica nanoparticles

Abstract

A route for europium (III) tris-pyrazolyl borate complex [Eu(Tp)$_3$] formation inside the pores of mesoporous silica nanoparticles (MSNs) has been established to yield a highly luminescent nanostructured hybrid. Two different in situ chemical precipitation techniques have been explored for the nanoencapsulation of the Eu^{3+} complex [Eu(Tp)$_3$] inside the pore channels of mesoporous silica nanoparticles, by varying the sequence order of precursor impregnation. In the first method, the Eu salt is introduced into the pores by wet impregnation and removal of the solvent, followed by wet impregnation of the ligand. In the second approach, the addition sequence is reversed. The importance of the addition sequence was demonstrated by the successful formation of the europium (III) tris-pyrazolyl borate complex in the pore network by following the first approach. The observed pyrazol-1-yl borate (Tp) to Eu^{3+} intramolecular energy transfer, i.e., the antenna effect, verified the formation of the complex. Photoluminescence spectroscopy, X-ray diffraction, N_2 adsorption, FT-IR spectroscopy, and TEM were used to characterize the material.

3.1. Introduction

Luminescent nanomaterials have received ever-increasing attention in recent years, due to a growing demand for new functional nanomaterials.[1] Amongst these, lanthanide based luminescent nanomaterials have been widely investigated because of their application in many different fields.

Mesoporous silica nanoparticles (MSNs) that are prepared by surfactant templating methods[2] display many attractive features and are ideal as host matrices for optical materials. Lanthanide complexes with organic ligands possess unique optical properties, and are widely used for biological applications. In particular, Eu (III) complexes with tailored antenna-ligands have been widely studied for applications that include biolabeling[3,4]. Although prior reports have been given for the doping of different Eu(III)-β-diketonates within inorganic matrices[5-7], their application as biolabels has been limited due to their poor stability in biological media. This inherent instability arises from their high sensitivity to aqueous environments, and to acidic and alkaline conditions. In contrast, highly symmetric pyrazole based scorpionate complexes show excellent stability under such conditions, which arises from their highly symmetric structure and ligand coordination sphere. Their intense luminescence emission[8,9] and elevated stability therefore makes them viable candidates for use in biolabeling applications. In this context, their incorporation into an inorganic host which may be readily dispersed in different media and modified on the surface is of interest. However, the pyrazole based scorpionate complexes have limited solubility in commonly used organic solvents, which means that the wet impregnation technique is unsuitable for their introduction into inorganic matrices.

MSNs have shown to be a promising matrix material. They provide a protective structure which prevents the incorporated guest molecules from coming into contact with the immediate external environment[10] and a chemically and mechanically stable vehicle. In some cases they have also shown to enhance the photophysical properties of the encapsulated fluorophores[11-14].

In the last few years, numerous examples of lanthanide complexes being incorporated into the pore structure of silica nanoparticles have been reported, with their preparation most commonly and conveniently achieved by wet impregnation[5]. This procedure requires good solubility of the

lanthanide complex, however, due to the low solubility of $Eu(Tp)_3$ in most common solvents, alternative routes for its incorporation into the matrix are required.

In this chapter we report a procedure for the in situ synthesis of $Eu(Tp)_3$ inside the pore channels of MSNs by two different routes: Eu salt impregnation followed by ligand impregnation (method A) and ligand impregnation followed by Eu salt impregnation (method B). The luminescent nanostructured material obtained by method A was characterized by photoluminescence spectroscopy, XRD, TEM, and FTIR spectroscopy, demonstrating the successful formation of the complex within the MSNs pores. The study was systematically carried out as follows: a) the bare MSNs were prepared and characterized, b) the bare MSNs were loaded with different amounts of $Eu(Tp)_3$ via method A, c) the maximum nominal complex loading for which all of the $Eu(Tp)_3$ was confined inside the pores of the MSNs was determined by XRD and TEM analysis, d) the MSNs were loaded with the same nominal concentration of $Eu(Tp)_3$ determined in step c via method B, and e) a comparison between the samples comprising the same nominal loading, prepared by the two different methods (A and B) was performed.

3.2. Experimental

3.2.1. Synthesis of $Eu(Tp)_3$ in the pore channels of MSNs

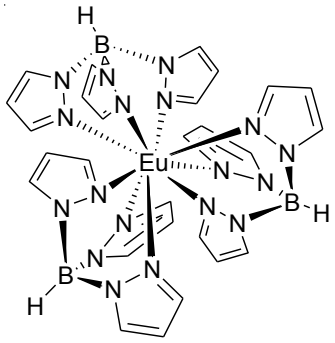

Figure 3.1: Molecular structure of the europium tris (pyrazolylborate) complex [$Eu(Tp)_3$] complex.

Method A: The general synthesis is described for sample Si-A-6: $EuCl_3 \cdot 6H_2O$ (2 mg, 0.006 mmol) was dissolved in distilled water (2 mL) and added to MSNs (0.100 g). The solution was stirred overnight and the water was then removed under reduced pressure. An aqueous solution containing 3 mol equivalents of KTp (4.5 mg, 0.018 mmol) in 2 mL of distilled water was added

to the residual solid. The resulting suspension was stirred overnight, and then the water was removed under reduced pressure. The resulting solid was washed twice with distilled water (10 mL). Samples Si-A-12 to Si-A-117 were prepared via the same procedure and the nominal concentrations are listed in Table 3.1. The theoretical % wt of the complex has been determined with respect to a 0.1 g silica matrix for each sample.

Method B: A solution of KTp (0.072 mmol) in distilled water (2 mL) was added to 0.100 g of MSNs and the suspension was stirred overnight. The solvent was subsequently removed under reduced pressure. To the obtained solid was added a solution containing $EuCl_3 \cdot 6H_2O$ (0.024 mmol) in 2 mL of distilled water. The resulting suspension was stirred overnight, and the water was then removed under reduced pressure. The resulting solid was washed twice by distilled water (10 mL). The obtained powder is named Si-B-24.

Table 3.1: Samples Si-A-6 to Si-A-117 prepared by method A. Sample Si-B-24 prepared by method B. (The maximum percentage of the occupied pores is evaluated by using the measured mass density of the Eu complex of 1.62 gr cm^{-3}).

Sample	Nominal concentration of $Eu(Tp)_3$ (mmol/0.1 g MSN)	Nominal wt% $Eu(Tp)_3$	Nominal % of pore volume occupied by $Eu(Tp)_3$
Si-A-6	0.006	4.5 %	1.8 %
Si-A-12	0.012	8.7 %	3.6 %
Si-A-24	**0.024**	**16 %**	**7.3 %**
Si-A-42	0.042	27.5 %	14.6 %
Si-A-84	0.084	43 %	29.3 %
Si-A-117	0.117	51 %	40.8 %
Si-B-24	**0.024**	**16 %**	**7.3 %**

3.3. Results and discussion

The morphology of the bare MSNs was shown to be spherical to elliptical in shape with diameters ranging 50-70 nm, as illustrated in the TEM micrograph (figure 3.2). The BET surface area was determined as 1286 m^2/g and the average pore volume was 4 nm.

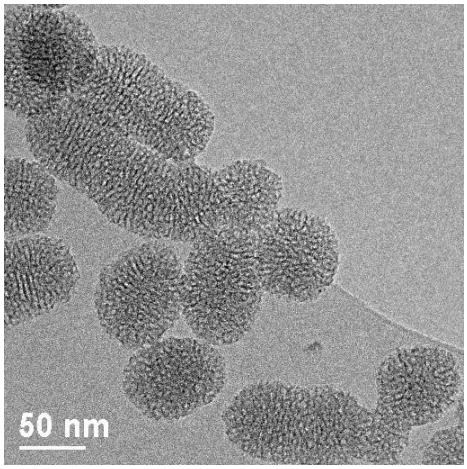

Figure 3.2: TEM micrograph of MSN powder.

In order to study the distribution of the Eu complex inside or outside the MSNs pores, the samples obtained by route A were examined by powder XRD and TEM analysis. Powder diffraction analysis can give indications as to whether the complex is present and where it is located with respect to the pore structure. The differentiation is made on the basis that large crystal growth can only occur outside the pores, while the confined internal space of the pores (*ca*. 3 nm) prevents the formation of crystals with sizes greater than the pore domain. In the latter case, the diffraction peaks would be extremely broad and difficult to discriminate from the amorphous pattern of the MSN matrix.

3.3.1. Powder X-ray diffraction analysis

Representative XRD patterns corresponding to sample Si-A-24, sample Si-A-42 and the pure complex are given in figure 3.3. The pure $Eu(Tp)_3$ showed a powder diffraction pattern which is typical of a material with large and well-formed crystals. In the pattern of sample Si-A-42, the narrow peaks in the spectrum were attributed to $Eu(Tp)_3$ crystallites greater than 30 nm, as determined by Scherrer analysis. All of the samples prepared by method A with $Eu(Tp)_3$ concentrations greater than 0.042 mmol showed similar patterns to that of sample Si-A-42 (not shown). In contrast, the characteristic peaks of the $Eu(Tp)_3$ complex could not be detected in the XRD pattern of sample Si-A-24, despite its presence being supported by PL and PLE data (see the discussion of the luminescence data). This is coherent with the presence of the complex

inside the pores of the MSNs. Similar XRD patterns were observed for the samples prepared with lower concentrations of the complex.

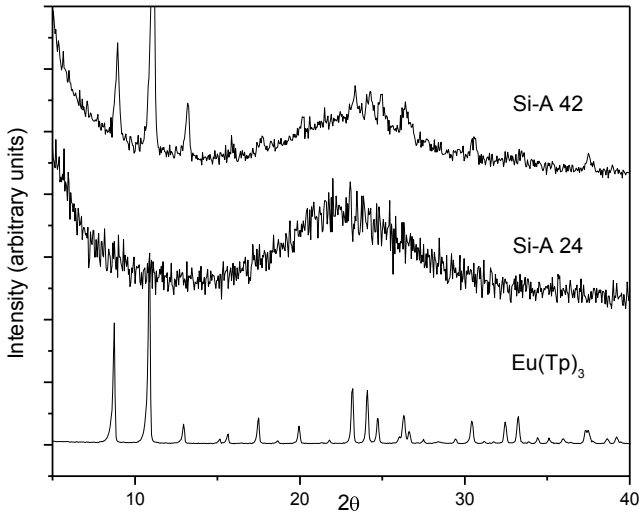

Figure 3.3: XRD pattern of $Eu(Tp)_3$, Si-A-24 (0.024 mmol of $Eu(Tp)_3$ complex), Si-A-42 (0.042 mmol of $Eu(Tp)_3$ complex).

3.3.2. TEM images:

TEM micrographs of the samples Si-A-24 and Si-A-42, prepared via route A, are respectively depicted in figure 3.4a and figure 3.4b. Micrograph figure 3.4b revealed the presence of large $Eu(Tp)_3$ crystals for the sample prepared with a nominal complex concentration of 0.042 mmol. This further corroborated the results obtained by XRD, which indicated that complex formation occurred outside of the pores. EDS microanalysis was performed by focusing on the large structures visible in the vicinity of the silica nanoparticles and supported the presence of Eu, C, N, O, and Si elements (figure 3.4c), which were attributed to the $Eu(Tp)_3$ complex. Copper peaks which were also visible in the spectra were ascribed to the support grid. In the samples prepared with $Eu(Tp)_3$ concentrations below 0.024 mmol (sample Si-A-24 is representatively shown in figure 3.4a), the presence of crystals could not be visually detected. Nevertheless, the EDS microanalysis which was focused on the MSNs revealed the presence of Eu, C, N, O, and Si elements, supporting the formation of the complex within the pore channels.

The XRD and TEM results show that the sample Si-A-24 contains all the loaded Eu within the pores of the MSNs. Since greater loading led to the formation of large complex crystals outside of the pores, the nominal concentration of $Eu(Tp)_3$ complex (i.e., 0.024 mmol) was used to prepare the comparative sample by method B.

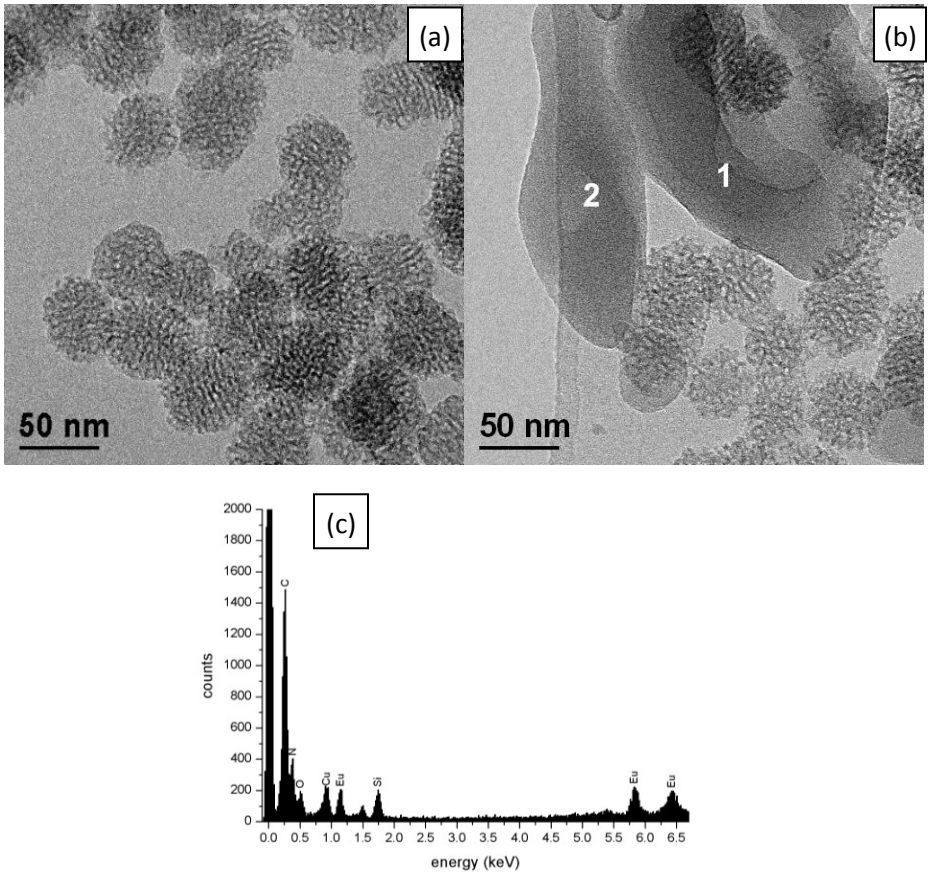

Figure 3.4: TEM images of (a) Si-A-24 and (b) Si-A-42 samples. The latter demonstrates the formation of the complex outside the silica pore channels. c) EDS spectrum for sample Si-A-42 focalized on point 1 in **4b**. This spectrum is identical to the one obtained on point 2.

3.3.3. N_2 adsorption desorption analysis

As described in the experimental section, the difference between the two proposed in situ routes is based on the addition sequence of the precursors by wet impregnation, as required to generate the $Eu(Tp)_3$ complex within the pores. In route A, impregnation of $EuCl_3$ is performed in a first step, followed by the addition of the ligand in a proceeding separate step. In route B, the addition sequence is reversed by introducing the ligand to the pore structure of the MSNs before the

addition of the Eu salt. The two samples, Si-A-24 and Si-B-24, contain the same nominal concentration of $Eu(Tp)_3$ complex (i.e., 0.024 mmol) despite their different preparation. N_2 adsorption data for sample Si-A-24 showed that the pore volume decreased markedly from 1.6 to 1.2 cm^3g^{-1}, and that the average pore diameter increased from 4.0 to 7.5 nm (Table 3.2). While this suggests that complex formation may have occurred within the pore structure, further examination of the materials' optical properties would also be necessary for confirmation. This observed increase in average pore diameter and decrease in pore volume can be explained by volume shrinkage, which eliminates some of the smaller pores. The apparent formation of the complex in the pores led to a decrease in the specific surface area from 1286 to 669 m^2g^{-1}. A similar trend was observed for sample Si-B-24. This similarity in reduced surface area and pore volume for the two samples should be expected since they were prepared using the same precursor concentration loading, notwithstanding the different addition sequences.

Table 3.2: N_2 adsorption desorption analysis results for the mesoporous silica nanoparticles and samples obtained with route A (Si-A-24) and route B (Si-B-24) with the 0.024 mmol concentration of $Eu(Tp)_3$.

Sample	BET Surface Area (m^2/g)	Single Point Adsorption Total Pore Volume (cm^3/g)	Adsorption Average Pore Diameter (nm)
MSN	1286	1.6	4.0
Si-A-24	669	1.2	7.5
Si-B-24	702	1.1	6.3

3.3.4. Photoluminescence properties

In order to probe the outcome of the two different methods tested for the in situ formation of the complex within the MSN pores, the photoluminescence properties of Si-A-24 (method A), Si-B-24 (method B) and the pure complex in the absence of silica were compared. The room temperature PLE (λ_{em}: 618 nm) spectra, and PL measured at both λ_{exc}: 318 nm and λ_{exc}: 394 nm are shown in figure 3.5a, 3.5b and 3.5c, respectively.

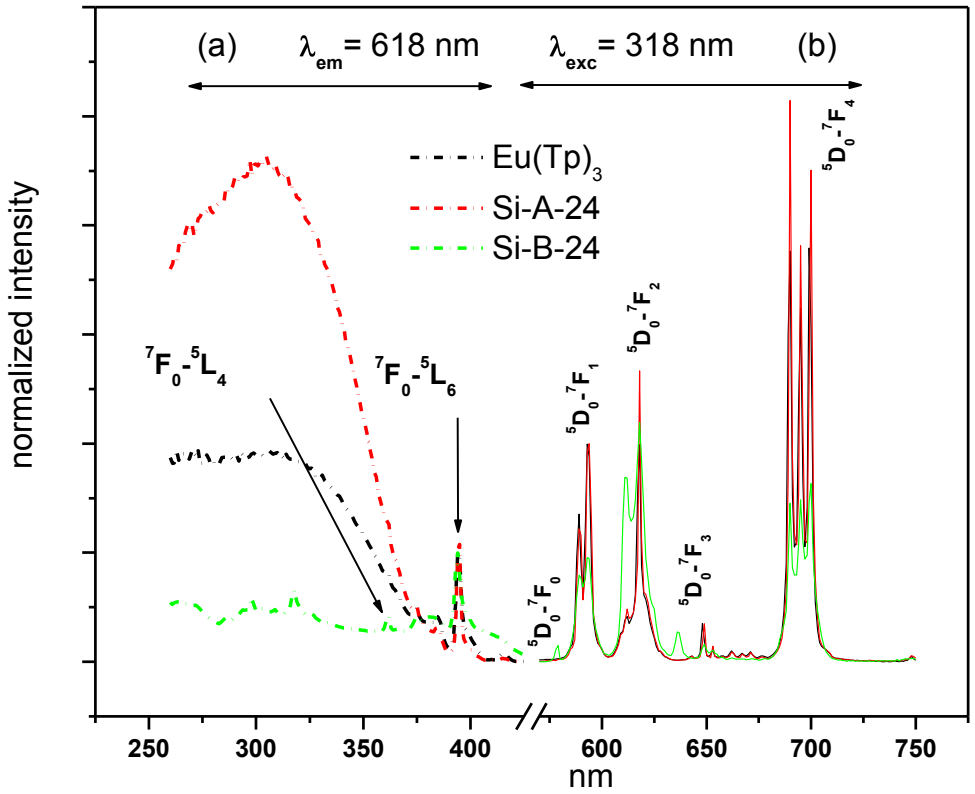

Figure 3.5: (a, left) room temperature PLE (λ_{em}: 618 nm) spectra, and (b, right) PL measured at λ_{exc}: 318 nm for solid samples of pure complex $Eu(Tp)_3$, Si-A-24 and Si-B-24.

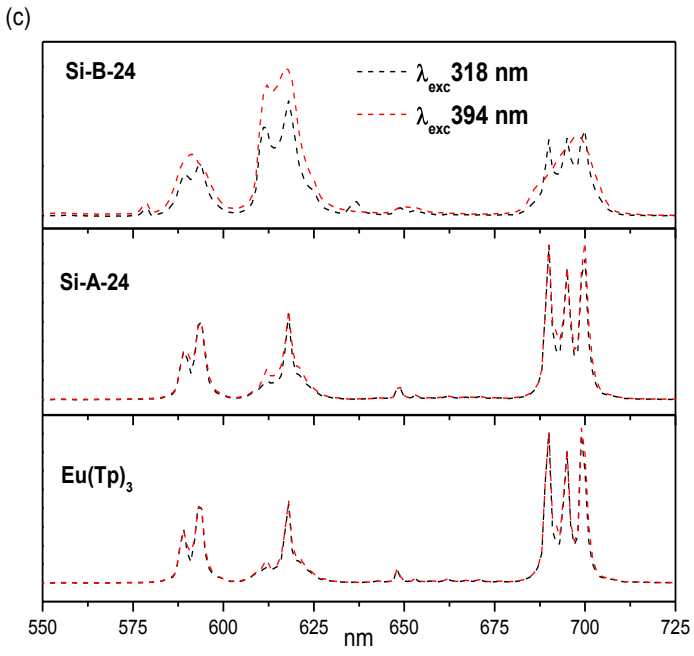

Figure 3.5: (c) comparison of room temperature luminescence emission spectra of complex $Eu(Tp)_3$, Si-A-24 and Si-B-24 measured at 318 nm and 394 nm.

In figure 3.5a, the excitation spectrum of the complex consists of a broad band which arises from the absorption of the ligands and from direct f–f electron transitions of Eu^{3+} ions. This absorption band is ascribed to the $\pi \rightarrow \pi^*$ band of the Tp ligand, most probably with contributions from a ligand-metal charge transfer (LMCT). The peak at 394 nm arises from direct excitation of the $^5L_6$ level of Eu^{3+} ions. Since this peak is related to the total amount of Eu^{3+} ions present, it was used to normalize the spectra of all three samples. A comparison of the normalized excitation spectra for Si-A-24, Si-B-24 and the pure complex revealed notable differences between the two samples (figure 3.5a). The spectrum of sample Si-A-24 resembled that of the $Eu(Tp)_3$ complex, whereby it showed the presence of an intense broad charge-transfer band in the UV region. In contrast, the spectrum of sample Si-B-24 displayed a markedly different excitation profile in which a clear absorption band was absent, and as a consequence the Eu^{3+} absorption peak appeared more prominent (figure 3.5a). The absence of the antenna effect for sample Si-B-24 is in agreement with the presence of Eu^{3+} ions that are not coordinated to the Tp ligands. This would also suggest that the in situ formation of $Eu(Tp)_3$ via method B is less efficient, resulting in the presence of Eu^{3+} ions with different local environments within sample Si-B-24. On this basis, the emission

spectra were collected at two different excitation wavelengths (318 nm and 394 nm) for both Si-A-24 and Si-B-24, and compared with the emission from the pure complex with the objective of probing the chemical environment surrounding the Eu^{3+} ions (figure 3.5b and figure 3.5c). In the case of excitation at 318 nm, the emission is expected to arise exclusively from the Eu^{3+} ions which belongs to the $Eu(Tp)_3$ complex. This would occur by the antenna effect from the ligand. While, the excitation at 394 nm would allow for direct excitation of all Eu^{3+} ions present in the sample, regardless of whether they are coordinated to ligands or not.

Following excitation at 318 nm, the $Eu(Tp)_3$ complex exhibited its characteristic emission spectrum as previously reported[8,9]. The typical peaks related to the electronic transitions from the $^5D_0$ excited state to the fundamental state ^7F_J (J = 1, 2, 3, and 4) of the Eu^{3+} ion were visible, while the $^5D_0 \rightarrow {}^7F_0$ transition appeared to be absent (figure 3.5c). Specifically, a doublet at 589 nm, 593 nm which corresponds to $^5D_0 \rightarrow {}^7F_1$ transitions, a band at 618 nm due to $^5D_0 \rightarrow {}^7F_2$ transitions, a band at 648 nm due to $^5D_0 \rightarrow {}^7F_3$ transitions, and a characteristic intense band centered at 695 nm and split in three peaks 690, 695, 699 nm due to the $^5D_0 \rightarrow {}^7F_4$ transitions could be detected. For the Eu^{3+} ion, the $^5D_0 \rightarrow {}^7F_j$ transitions are predominantly electric dipole for j even and completely magnetic dipole for j odd. The intensities of electric dipole transitions, in particular for j = 0 and for j = 2, are strongly sensitive to the rare earth surrounding environment. They are absent (j = 0) or small (j = 2) in high symmetry sites, while the intensities of magnetic dipole transitions are almost independent of their environment[15]. In the emission spectrum reported in figure 3.5b, the $^5D_0 \rightarrow {}^7F_0$ transition is lacking and the $^5D_0 \rightarrow {}^7F_2$ is unusually small with respect to the high intensity of the $^5D_0 \rightarrow {}^7F_4$ triplet, thus indicating a very high symmetry of the site occupied by Eu^{3+} ions in the $Eu(Tp)_3$ complex.

The emission spectra for sample Si-A-24, collected by excitation at 394 nm and 318 nm (figure 3.5c), were in excellent agreement with the spectra of the pure complex $Eu(Tp)_3$. This supports the success of route A synthesis, indicating that all of the Eu ions in sample Si-A-24 were present as coordinated ions in the $Eu(Tp)_3$ complex. Contrastingly, different emission profiles were observed for sample Si-B-24 when it was excited at the two different wavelengths (figure 3.5c). This variation in emission for sample Si-B-24 indicated the presence of at least two different local environments surrounding the Eu^{3+} ions. We suggest that one of these could be related to the Eu^{3+} ion coordinated to the ligands, and another to non-coordinated Eu^{3+} ions. Indeed, when

the sample Si-B-24 was excited at 318 nm (figure 3.5b), the characteristic three peaks of the $^5D_0 \rightarrow {}^7F_4$ transitions around 695 nm were visible. This suggested the presence of the $Eu(Tp)_3$ complex, despite the visibly lower PL intensity of the signals of interest with respect to the other measured samples. However, when sample Si-B-24 was excited at 394 nm it displayed a different pattern from that of the pure complex (figure 3.5c), showing that many Eu ions were not coordinated to the ligands in the sample prepared via route B. Moreover, the $^5D_0 \rightarrow {}^7F_0$ transition emerges in the spectrum of this sample as a clear indication for reduction in the site symmetry surrounding the rare earth ion. As further proof, the ratio (*R*) between the integrated intensity of the electric dipole transitions $^5D_0 \rightarrow {}^7F_2$ (hypersensitive forced electric dipole transition) and the pure magnetic dipole transitions $^5D_0 \rightarrow {}^7F_1$, centered respectively at 606 nm and 590 nm, gives an indicative measure of the symmetry of the coordination polyhedron of the Eu^{3+} ion. As determined from the PL profiles (figure 3.5c), *R* drastically changes from Si-B-24 (*R*=3.0) to Si-A-24 (*R*=1.3) and the pure complex [$Eu(Tp)_3$] (*R*=1.0), supporting a change for the site symmetry surrounding the Eu^{3+} ions in the three samples.

The time-resolved photoluminescence curves for the samples Si-A-24, Si-B-24 and the pure complex are shown in figure 3.6. The PL lifetime for Eu^{3+} ions was measured (λ_{em}: 618 nm) under 330 nm excitation. For the sample Si-A-24, the decay curve is a single exponential one and the lifetime value is 2.04 ms, giving further evidence that the Eu^{3+} ions are present in a single coordination environment. The decay curve for pure $Eu(Tp)_3$ in its solid state is also a single exponential one with a lifetime of 1.78 ms, which is in close agreement with the lifetime value previously reported for the complex (1.84 ms)[8,9]. The lifetime value for Si-A-24 is higher than that of the pure $Eu(Tp)_3$ complex in the solid state and significantly higher than the reported lifetimes of several isolated β–diketonate complexes[16,17], and those incorporated into sol-gel/silica matrices[18]. Contrastingly, a two exponential decay curve was required to fit the Si-B-24 sample decay profile, giving the following parameters; τ_1: 0.32 ms, τ_2: 1.20 ms with relative weights A_1: 0.914 and A_2: 0.086. The use of a multi exponential function agrees with the presence of more than one site for Eu^{3+} ions in the sample Si-B-24. Population analysis has been carried out by a method reported by Bünzli et al,[19] to determine populations of different Eu^{3+} sites in the sample B. Populations of two species derived by using the decay curve are P_1: 0.745 and P_2: 0.255.

Since the photoluminescence lifetime of a sample is an indication of its quantum efficiency, the efficiency for sample Si-A-24 should be similar to the efficiency of the pure complex, while that for sample Si-B-24 is expected to be lower. To confirm this statement, we measured the quantum yields (which correspond to the rate of emitted photons vs. absorbed photons) in the spectral region of ligand absorption at 345 nm excitation. The obtained values were 14 ± 2 % for both the pure $Eu(Tp)_3$ complex and for sample Si-A-24, and 3 ± 2 % for the sample Si-B-24.

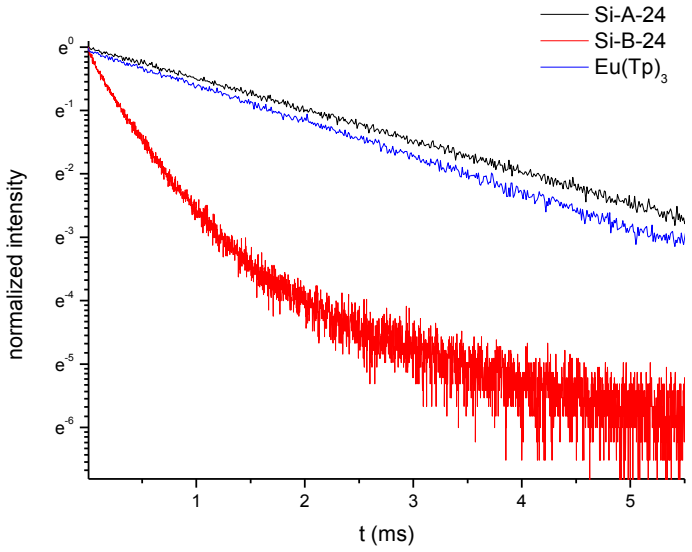

Figure 3.6: Decay curves for the Eu^{3+} in samples Si-A-24, Si-B-24, and $Eu(Tp)_3$ measured at 330 nm excitation wavelength and 618 nm emission.

3.3.5. FTIR spectroscopy:

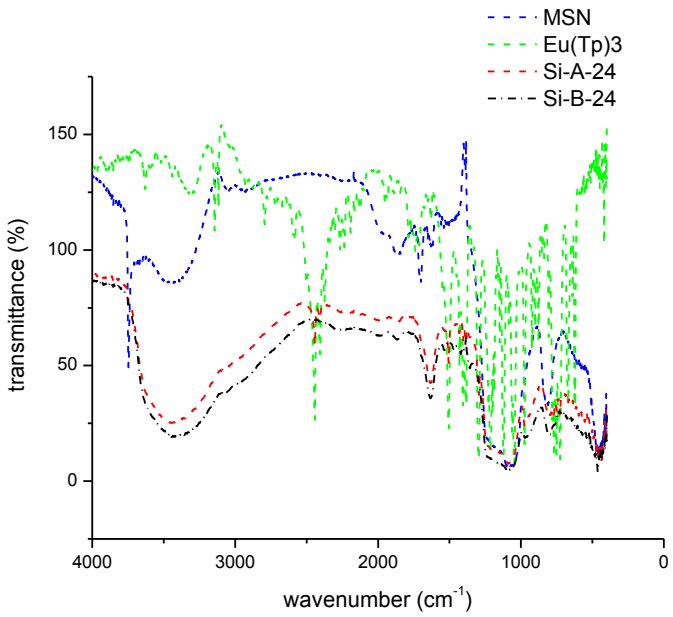

Figure 3.7: FTIR spectrum of MSNs, $Eu(Tp)_3$ and samples Si-A-24 and Si-B-24.

The FTIR spectra of the bare MSNs, $Eu(Tp)_3$ and the two samples Si-A-24 and Si-B-24, are compared in figure 3.7. An absorption band observed at 2440 cm^{-1} is assigned to the B-H stretching of the tris(pyrazolylborate) ligand in the pure $Eu(Tp)_3$ complex[8]. The presence of the B-H stretching band is also noted for sample Si-A-24, in agreement with the presence of the complex. Contrastingly, its presence is not observed in the spectrum of sample Si-B-24, suggesting that the complex has either not formed or is present in a lower quantity. In the latter case, the characteristic bands of the complex would be relatively weak and therefore obscured by those of the MSNs.

Following confirmation by PL and PLE of the successful formation of $Eu(Tp)_3$ via route A, we examined the emission intensity as a function of the complex concentration within the pores of MSNs (figure 3.8). The series of concentrations loaded in MSNs via method A are included in table 3.1. The relative emission intensity of the obtained luminescent nanomaterials recorded at 699 nm increased steadily up to the concentration of 0.084 mmol $Eu(Tp)_3$. Thereafter, no significant increase in the intensity was observed which is most likely ascribed to saturation by concentration quenching (figure 3.8).

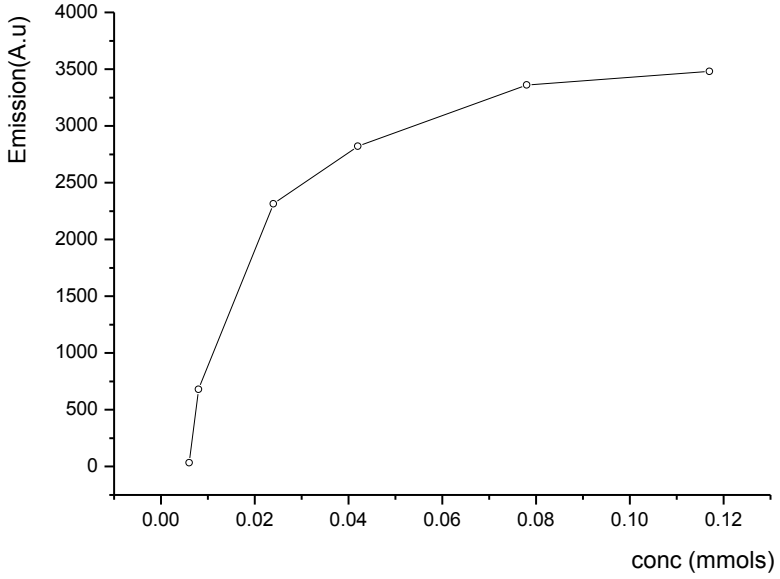

Figure 3.8: Dependence of the relative intensity of emission with the $Eu(Tp)_3$ loading in MSN matrix for samples prepared by method A: $Eu(Tp)_3$ concentrations, 0.006, 0.012, 0.024, 0.042, 0.084, 0.117 mmol.

Based on the aforementioned results, we can suggest a plausible mechanism for the in situ formation of the complex via method A. When the Eu salt is introduced into the pores of MSNs in the first step (method A), it interacts with the surface silanol groups to form coordination bonds with the silanol oxygen atoms. As such, Eu^{3+} is accessible to the nitrogen atoms in the tris-pyrazolyl borate ligand which is introduced in the second step. The addition of the ligand in the second step subsequently proceeds with the formation of the complex in the pore structure of the MSNs. On the contrary, when the ligands are introduced in the first step as conducted in method B, nitrogen atoms in the tris-pyrazolyl borate form hydrogen bonds with the protons of the silanol groups. Consequently, Eu^{3+} ions have limited access to the ligand nitrogen atoms, thus hampering the formation of the complex inside the pores. This hypothesis was supported by pH measurements performed for the aqueous solutions of the Eu salt and ligand, in addition to the suspensions obtained by addition of these to the MSNs. A decrease in the pH from 4.9 (±0.02) to 3.58 (±0.02) was noted for the MSN suspension after the addition of the aqueous Eu salt solution (pH 5.37±0.02). This decrease in the suspension pH is thought to arise from the generation of hydrogen chloride by reaction of silanol protons with Cl^- ions liberated from the Eu salt. Change

in the pH for aqueous tris-pyrazolyl borate solution from 9.6 (±0.02) to 8.02 (±0.02) was noted on addition of ligand solution to MSNs in the first step during method B. This decrease in pH was most likely due to the acidic properties of the silica nanoparticles.

3.4. Conclusion

Europium (III) tris-pyrazolyl borate complex $Eu(Tp)_3$ was successfully synthesized inside the pores of mesoporous silica nanoparticles (MSNs). It was found that the wet impregnation of the MSNs with the Eu salt in a first step, followed by separate impregnation of the ligand (method A) could be applied to efficiently synthesize the complex within the pores. The confinement of the complex within the pore structure was achieved for $Eu(Tp)_3$ concentrations up to 0.024 mmol, which corresponded to 7.3 % of the pore volume being occupied. Exceeding this concentration resulted in complex formation outside the MSN pores, as verified by XRD and TEM analysis. The photoluminescence emission spectrum of the sample Si-A-24 was identical to that of the pure complex $Eu(Tp)_3$ in its solid state, while its radiative lifetime was found to be greater. The importance of the precursor addition sequence was demonstrated, whereby the reverse sequence of ligand addition followed by Eu salt addition (method B) led to lower formation of the complex in the pores and gave the presence of different Eu^{3+} emitting species.

3.5. References

[1] W.C.W. Chan, D.J. Maxwell, X. Gao, R.E. Bailey, M. Han, S. Nie, Curr. Opin. Biotech. 13 (2002) 40.

[2] C.T. Kresge, M.E. Leonowicz, W.J. Roth, J.C. Vartuli, J.S. Beck, Nature 359 (1992) 710.

[3] G.A. Kumar, R. Riman, E. Snitzer, J. Ballato, J. Appl. Phys. 95 (2004) 40.

[4] C.W. Lu, Y. Hung, J.K. Hsiao, M. Yao, T.H. Chung, Y.S. Lin, S.H. Wu, S.C. Hsu, H. M. Liu, C.Y. Mou, C.S. Yang, D.M. Huang, Y.C. Chen, Nano Lett. 7 (2007) 149.

[5] K. Binnemans, Chem. Rev. 109 (2009) 4283.

[6] L. Armelao, S. Quici, F. Barigelletti, G. Accorsi, G. Bottaro, M. Cavazzini, E. Tondello, Coord. Chem. Rev. 254 (2010) 487.

[7] K. Binnemans, in: K.A. Gschneidner Jr., J.-C.G. Bünzli, V.K. Pecharsky (Eds.), Handbook on the Physics and Chemistry of Rare Earth, 25, Elsevier, Amsterdam, 2005, pp. 107–272.

[8] M. Bortoluzzi, G. Paolucci, S. Polizzi, L. Bellotto, F. Enrichi, S. Ciorba, B. S. Richards, Inorg. Chem. Commun. 14 (2011) 1762.

[9] M. Bortoluzzi, G. Paolucci, M. Gatto, S. Roppa, F. Enrichi, S. Ciorba, B. S. Richards, J. Lumin. 132 (2012) 2378.

[10] J. Lei, L. Wang, J. Zhang, ACS Nano 5 (2011) 3447.

[11] D.R. Larson, H. Ow, H.D. Vishwasrao, A.A. Heikal, U. Wiesner, W.W. Webb, Chem. Mater. 20 (2008) 2677

[12] W. Tan, K. Wang, X. He, X.J. Zhao, T. Drake, L. Wang, R.P. Bagwe, Med. Res. Rev. 24 (2004) 621

[13] J. Yan, M.C. Estévez, J.E. Smith, K. Wang, X. He, L. Wang, W. Tan, Nano Today 2 (2007) 44

[14] X.L. Guével, B. Hötzer, G. Jung, M. Schneider, J. Mater. Chem. 21 (2011) 2974.

[15] S. Cotton, Lanthanide and Actinide Chemistry, John Wiley & Sons Ltd, Chichester, West Sussex, England, 2006.

[16] L.R. Melby, N.J. Rose, E. Abramson, J.C. Caris, J. Am. Chem. Soc. 86 (1964) 5117

[17] H. Bauer, J. Blanc, D.L. Ross, J. Am. Chem. Soc. 86 (1964) 5125.

[18] K. Binnemans, P. Lenaerts, K. Driesen, C.G.Walrand, J. Mater. Chem. 14 (2004) 191.

[19] Basics of lanthanide photophysics. Lanthanide luminescence: Photophysical, analytical and biological aspects, JCG Bünzli, SV Eliseeva, in: P Hänninen, H Härmä (Eds.), Spinger Series on Fluorescence, Springer Verlag, Berlin, (8) 2010, 1-45.

Chapter 4

Studies on the structural and photo-physical properties of rare-earth complex encapsulated into surface modified mesoporous silica nanoparticles

Abstract:

The encapsulation of the rare-earth complex [Eu(dbm)$_3$phen] into functionalized mesoporous silica nanoparticles (MSN) has been carried out to study the effect of chemical environment in the mesoporous silica on the photoluminescence properties of encapsulated Eu(dbm)$_3$phen complex. Surface functionalization was achieved by the reaction of the silanol groups on surface of mesoporous silica with different organosilylating agents such as (3-aminopropyl)-triethoxysilane (APTES), (3-Mercaptopropyl)-trimethoxysilane (MPTMS), and ethoxytrimethylsilane (ETMS). An enhancement in the luminescence properties of the Eu(dbm)$_3$phen complex have been observed on its encapsulation into surface modified mesoporous silica nanoparticles. The modification of photophysical properties are attributed to interaction of Eu(dbm)$_3$phen with the different chemical environment in the functionalized mesoporous silica nanoparticles. The luminescence properties of rare-earth complex in surface-modified mesoporous silica nanoparticles (MSN) increase in the order of MSN < MSN-ETMS < MSN-MPTMS < MSN-APTES. The encapsulated Eu(dbm)$_3$phen complex shows enhanced luminescence with the higher intensity of the peak due to $^5D_0 - {}^7F_2$ transition and exhibits increased lifetime in the functionalized mesoporous silica nanoparticles compared to the pure rare-earth complex in solid state and that in unmodified MSN. This implies that some interactions of the lanthanide complexes takes place in their incorporation process into the organically modified mesoporous silica nanoparticles. The organically modified mesoporous

silica nanoparticles were characterized with powder X-ray diffraction (XRD), Fourier transform infrared spectroscopy (FTIR), N_2 adsorption desorption etc. and the luminescence properties of the $Eu(dbm)_3phen$ encapsulated in these functionalized materials is studied. Moreover, Solid state nuclear magnetic resonance (SSNMR) techniques were used to investigate the structural behavior of the $Eu(dbm)_3phen$ doped in functionalized MSNs by doping analogous diamagnetic model complex $Y(dbm)_3phen$ into the pore structures of modified MSNs. These studies indicates that the encapsulated rare-earth complex show some interactions with the functional groups anchored on the surface of MSNs.

4.1. Introduction

There is an increasing interest in the development of lanthanide based luminescent materials; especially those of Eu^{3+} and Tb^{3+} with organic ligands which often show excellent luminescence characteristics.[1-5] Weissman first reported the light-emission characteristics of lanthanide complexes of β-diketonates in 1942.[6] However, the lanthanide complexes have been excluded from practical applications due to their poor thermal stability and mechanical properties. In attempting to solve these problems, some research groups have incorporated the complexes into inorganic[5, 7-11] and polymeric matrix materials.[2,12,13] The incorporation of lanthanide complexes within silica matrices[14] or organic-inorganic hybrid matrices[15] has also been extensively investigated. These studies have indicated that the matrix not only improves the thermal stability[16] and mechanical properties[17] of the complexes but it also significantly improves the photophysical properties of the lanthanide complexes.[18-21] Consequently, the incorporation of luminescent lanthanide complexes in solid matrices is of great interest as it allows the construction of functional materials with improved optical properties. In particular, the use of porous inorganic nanoparticles as scaffolds for the lanthanide complexes incorporation can improve the interactions between the lanthanide complex and the matrix. Many researchers have focused on the preparation of organically functionalized mesoporous silica nanoparticles (MSNs) by covalent attachment of a wide number of functional groups by post-synthesis grafting on the MSNs exploiting the simple alkoxysilane chemistry.[22,23] Surface functionalization of MSNs with organic moieties allows a wide range of manipulations of the surface properties and enhances the biocompatibility of these materials.[24] Moreover, surface modification with organic functional groups changes the chemical environment inside the pore structures of these nanoparticles.[32]

Although numerous studies have reported the encapsulation of rare earth complexes in the MSNs, there have been only a few reports about the influence of different chemical environments due to the functionalization in the pore structure of MSNs on the structural and photophysical properties of encapsulated rare earth complex.

To this aim, the combination of photoluminescence and solid state NMR spectroscopy can be very useful. In particular, solid state NMR allows structural features of the surface functionalized MSNs and their interactions with the encapsulated complex to be investigated. Unfortunately, the solid state NMR study cannot be easily carried out on materials containing, for example, europium complexes that usually show excellent optical properties, owing to their paramagnetism which causes dramatic broadening of the NMR peaks and shortening of the relaxation times. A good alternative could consist in studying by NMR the structurally analogous Yttrium complexes that, albeit not showing good optical properties, are not paramagnetic. This allows detailed structural and dynamic information to be obtained from high-resolution spectra and relaxation time measurements, respectively.

In this chapter, we aim to examine the influence of the presence of organic functional groups grafted on the surface of MSNs on an encapsulated rare-earth complex. In particular, we report a detailed study, carried out mainly by combining photoluminescence and solid-state NMR techniques, on the photophysical properties of $Eu(dbm)_3phen$ and the structural properties of $Y(dbm)_3phen$, both encapsulated in organically modified mesoporous silica nanoparticles. The $Eu(dbm)_3phen$ complex was chosen for this study as it shows excellent luminescence properties and good solubility in commonly used solvents, which allows its incorporation into MSNs with the impregnation technique. On the other hand, in order to get insights into the structural and dynamic behavior of the $Eu(dbm)_3phen$ incorporated into functionalized MSNs, an analogous diamagnetic model complex, $Y(dbm)_3phen$, was purposely synthesized and encapsulated into functionalized MSNs. In this complex the europium is replaced by yttrium, which has a similar chemical behavior and atomic radius to europium, but it is more suitable for a solid state NMR analysis. The systematic study was carried out as follows: a) the bare MSNs were prepared and characterized, b) the surface modification of bare MSNs was achieved by functionalization with different organosilylating agents such as APTES, MPTMS, and ETMS; and the resulting functionalized MSNs were characterized by solid state NMR (SSNMR), FTIR, BET, XRD and

TEM etc. c) the encapsulation of $M(dbm)_3phen$ complexes (M = Eu, Y) into the bare MSNs and functionalized MSNs was carried out by wet impregnation technique, d) the SSNMR technique was used to study the structural and dynamic properties of the composite nanomaterials obtained by incorporating the analogous diamagnetic $Y(dbm)_3phen$ complex into MSNs, e) the photophysical properties of the $Eu(dbm)_3phen$ complex doped MSNs were studied by luminescence and UV-Vis reflectance spectroscopy.

4.2. Experimental

4.2.1. Functionalization of MSNs:

4.2.1.1.Functionalization of MSNs with APTES [MSN-APTES]

The functionalization has been performed by adaptation of the method by Chen and Brauer.[25] Surface grafting of APTES was achieved by addition of a cyclohexane (5 mL) solution containing 2% v/v APTES and 2% v/v *n*-propylamine to the powdered MSN (100 mg). The suspension was stirred at ambient temperature for 2 h, after which it was recovered and purified by repeated (3 times) centrifugation (30 min at 9000 rpm), hexane washing and sonication (30 min). The obtained sample, MSN-APTES was dried under reduced pressure (10^{-1} mbar for 4 h).

4.2.1.2.Functionalization of MSN with MPTMS [MSN-MPTMS]

The functionalization has been performed by using procedure similar to that used for APTES functionalization. Surface grafting of MPTMS was achieved by addition of a cyclohexane (5 mL) solution containing 2% v/v MPTMS and 2% v/v *n*-propylamine to the powdered MSNs (100 mg). The suspension was stirred at ambient temperature for 2 h, after which it was recovered and purified by repeated (3 times) centrifugation (30 min at 9000 rpm), hexane washing and sonication (30 min). The obtained sample, [MSN-MPTMS] was first air dried overnight and then under reduced pressure (10^{-1} mbar for 4 hr).

4.2.1.3.Functionalization of MSN with Ethoxytrimethylsilane ETMS [MSN-ETMS]

Capping of surface -OH groups on MSNs was carried using ethoxy trimethylsilane to tune its hydrophobicity using the procedure similar to that of W. Shen et al.[26] In a typical method, predried MSN (0.89 g) and ethoxytrimethylsilane (1 mL) were added to the dry toluene (15 mL)

and the resulting solution mixture was refluxed under the nitrogen atmosphere for 12 hours. The hydrophobicity modified MSN was filtered and washed by toluene and anhydrous ethanol in turn. At last, the solid [MSN-ETMS] was air dried overnight and then under reduced pressure (10^{-1} mbar for 4 hr).

Synthesis procedures for the surface functionalization of mesoporous silica nanoparticles (MSN) using organic silylating agents are shown in scheme 4.1.

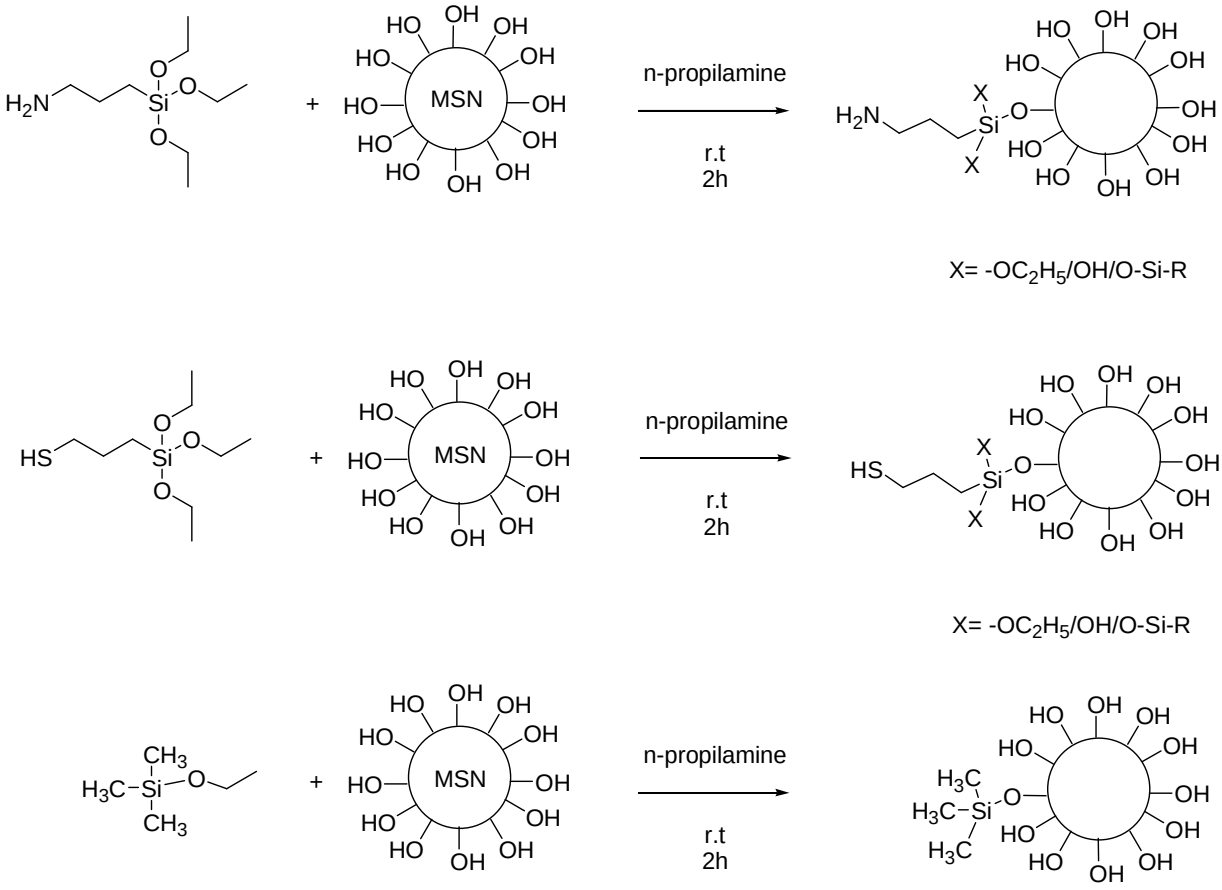

Scheme 4.1: Scheme of the synthesis procedures for the surface functionalization of mesoporous silica nanoparticles (MSN) using organic silylating agents

4.2.2. Preparation of Eu(dbm)$_3$phen-MSN and Y(dbm)$_3$phen-MSN composites:

4.2.2.1.Preparation of Eu(dbm)$_3$phen-MSN composites:

Incorporation of Eu(dbm)$_3$phen complex in MSNs has been carried by using wet impregnation method, where the functionalized MSNs sample [100 mg] was stirred overnight with (1 mL, 8

mM) Eu(dbm)$_3$phen complex solution in dichloromethane. Finally, the solid was dried under reduced pressure (10^{-1} mbar for 4 h).

4.2.2.2.Preparation of Y(dbm)$_3$phen-MSN composites:

Y(dbm)$_3$phen-MSN composites were prepared using the similar procedure used for preparing Eu(dbm)$_3$phen-MSN composites.

4.3. Results and Discussion:

4.3.1. Characterization of the Eu(dbm)$_3$phen and Y(dbm)$_3$phen complexes:

As a first step for the study of the composites of M(dbm)$_3$phen (M = Eu^{3+} and Y^{3+}) and surface-modified MSNs, a characterization of Eu(dbm)$_3$phen and Y(dbm)$_3$phen bare complexes was carried out by means of FTIR, XRD and SSNMR. Although Eu(dbm)$_3$phen complexes have been widely used and well characterized**,** there are only few reports on Y(dbm)$_3$phen and no characterization is available for this complex in the literature.

4.3.1.1.FTIR spectra:

As shown in figure 4.1, both the complexes display similar FTIR spectra owing to the dibenzoylmethane and phenanthroline ligands that are responsible for the vibrations of these complexes. Strong absorption bands between 3250 cm^{-1} and 2950 cm^{-1} are observed mainly due to the C-H stretching vibrations of the phenyl ring, and numerous strong and medium absorptions below 1700 cm^{-1} are observed for the dibenzoylmethane and phenanthroline ligands. Detailed information of all the observed peaks is given in table 4.1.

Table 4.1: Absorption bands of rare earth complexes: Eu(dbm)$_3$phen (a) and Y(dbm)$_3$phen (b).

3058 cm-1: Ar C-H str. Vibrations, 1594 cm-1 (ν_{as} C=O), 1548 cm-1 (ν_s C=C), 1517 cm-1 (ν_s C=O), 1460 cm-1 (δ_{as} C-H), 1414 cm-1 (ν C=N of phen), 1309 cm-1 (ν_{as} C=C), 1220 cm-1 (δ C-H), 1023 cm-1 (ν N-C-C), 752 cm-1 (π C-H), 723 cm-1 (π C-H of phen)

ν_s (ν_{as}): symmetrical (asymmetrical) stretching vibrations
δ: in plane bending vibrations

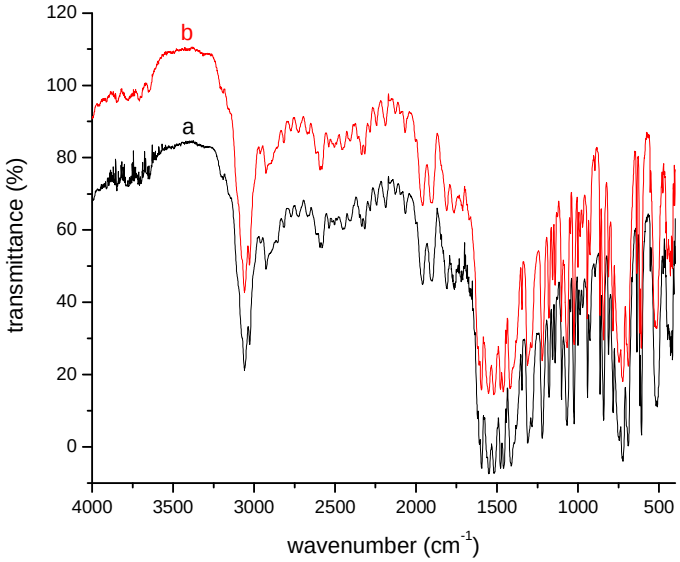

Figure 4.1: FTIR spectra of rare earth complexes: Eu(dbm)$_3$phen **(a)** and Y(dbm)$_3$phen **(b).**

4.3.1.2.Powder X-ray diffraction analysis:

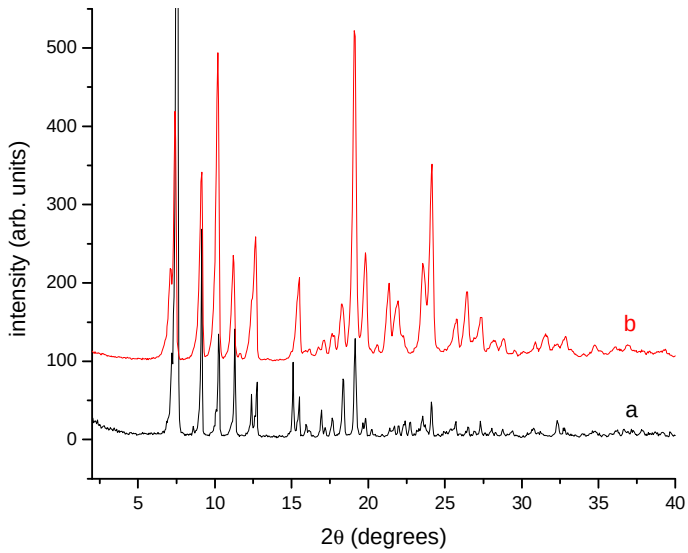

Figure 4.2: X-ray diffraction pattern of Eu(dbm)$_3$phen **(a)** and Y(dbm)$_3$phen **(b)** complexes.

The crystalline nature of the rare earth complexes were evaluated by X-ray diffraction (XRD) experiments. The XRD pattern of the $Y(dbm)_3$phen complex showed the well defined crystalline behavior similar to that of $Eu(dbm)_3$phen reported earlier.[27]

The X-ray diffraction analysis and FTIR study reveals the structural similarity between the two rare earth complexes (figure 4.2).

4.3.1.3. ^{13}C CPMAS spectra of the $Y(dbm)_3$phen complex

In figure 4.3, the ^{13}C CPMAS spectrum of the $Y(dbm)_3$phen complex is reported along with its chemical structure. To the best of our knowledge, in the literature there are no ^{13}C spectra of similar complexes in the solid state with the exception of that reported in reference [28] recorded on a complex where dibenzoylmethane ligands are coordinated with the transition metal cations. Four main peaks can be found in the spectrum, and assigned to: dibenzoylmethane carbons (93 ppm), the carbons of benzoyl ring and phenanthroline e, g, h carbons (127 ppm), phenanthroline d and i carbons (140 ppm), and phenanthroline f carbons (150 ppm). Peaks due to b and c carbons of dibenzoylmethane could not be clearly observed due to overlap with spinning sidebands. Even if the resolution of the spectrum is quite poor, it appears well compatible with the occurrence of a single resonance structure for the three dibenzoylmethane ligands, in agreement with X-ray data reported for similar complexes.[29] In figure 4.3 (b), the ^{13}C DE-MAS spectrum of the complex, recorded with a very short relaxation delay of 2 s, is also reported. In this experiment only the signals of ^{13}C nuclei characterized by a short T_1 (typically in a mobile environment) are present: in our case the peak which seems mostly favored in the DE experiment is that at 127 ppm, suggesting that benzoyl rings experience a quite high mobility in the complex.

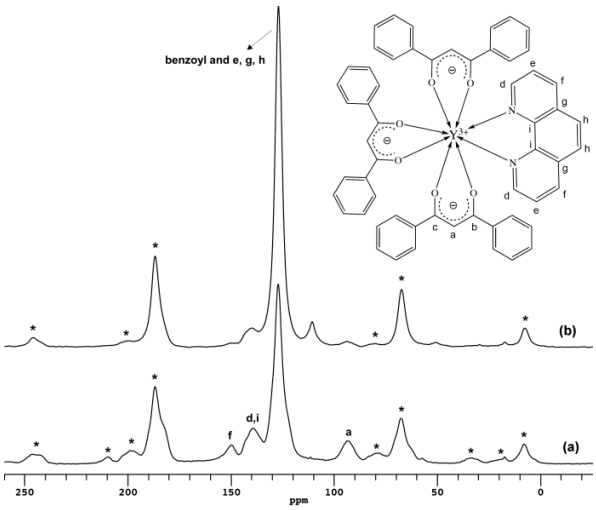

Figure 4.3: ^{13}C spectra of Y(dbm)$_3$phen complex; (a) CP acquired at a spinning frequency of 6 kHz and (b) DE with a recycle delay of 2 s, acquired at a spinning frequency of 6 kHz. The small signal at ≈ 110 ppm in (b) arises from incomplete suppression of the probe and rotor background signal. Spinning sidebands are marked with asterisks.

4.3.2. Characterization of composites of surface-modified MSNs and M(dbm)$_3$phen complexes.

The structural, morphological and dynamic properties of MSNs, surface-modified with alkoxysilanes (APTES, MPTMS, ETMS), and their composites with either Eu(dbm)$_3$phen or Y(dbm)$_3$phen complex have been investigated by means of several techniques.

4.3.2.1.FTIR spectroscopy

The grafting of different functional groups on the silica surface was qualitatively confirmed by FTIR spectroscopy. FTIR spectra taken in transmission mode for the unmodified mesoporous silica (MSN), MSN-APTES, MSN-MPTMS, and MSN-ETMS are illustrated in figure 4.4.

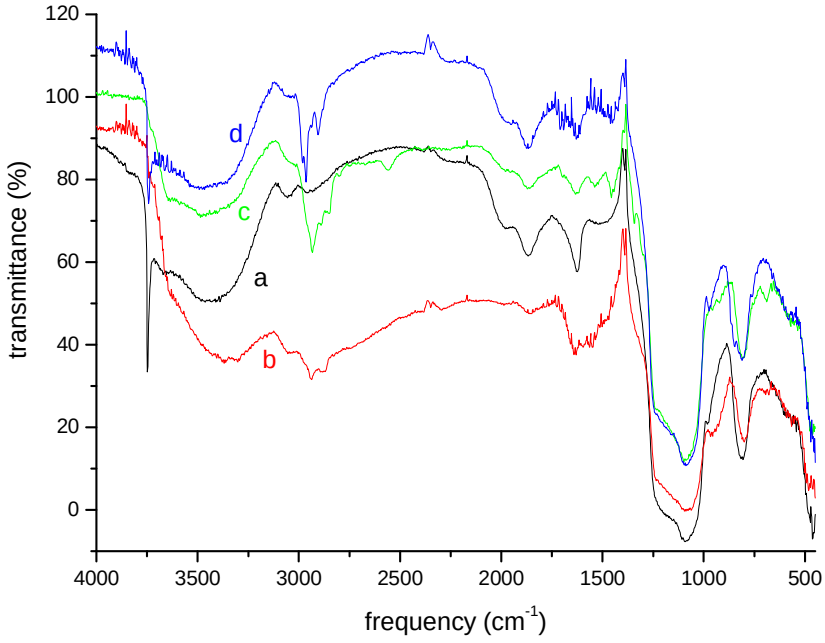

Figure 4.4: FTIR spectra of: a) the unmodified mesoporous silica nanoparticles (MSN); b) MSN-APTES; c) MSN-MPTMS; d) MSN-ETMS.

Mesoporous silica exhibits a strong absorption band of siloxane (Si-O-Si) bonding at 1200 cm^{-1} and the silanol –OH band at 3743 cm^{-1} and other peaks in range and 3700-3000 cm^{-1} due to adsorbed or hydrogen-bonded water molecule.[30, 31] This peak almost disappears on grafting different functional groups on the silica surface. For MSN-APTES a weak peak at 673 cm^{-1} can be assigned to the deformation of the N-H bonds.[32] The C-N stretching vibration peak at 1000-1200 cm^{-1} was not resolved due to the overlay with the IR absorptions of Si-O-Si in the range 1130-1000 cm^{-1} and of Si-CH_2-R in the range 1250-1200 cm^{-1}.[33] Nevertheless, the broadened nature of the peak in the region 1130-1000 cm^{-1} indicates the possible overlap of peaks. In addition, an intense peak at 1650 cm^{-1} was observed due to N-H bending vibration that further confirms the presence of N-H groups. The broadening of this peak can be ascribed to the overlap of the N-H bending vibration band with the peak due to adsorbed water in the MSN-APTES sample.[33, 34] A broad band centered at 3350 cm^{-1} is assigned to the N-H stretching vibrations of the -NH_2 group in the MSN-APTES.[35] The spectrum of MSN-MPTMS shows peaks at 2552 and 686 cm^{-1} for the S-H stretching and C-S bending vibrations, respectively. Both MSN-APTES and

MSN-MPTMS spectra show the presence of –CH stretching vibration bands in the region 3100 - 2700 cm^{-1} due to the propyl group introduced by the functionalization of the silica surface.[36] The FTIR spectrum of MSN-ETMS show C-H stretching vibration peaks between 3010 and 2860 cm^{-1} and C-H deformation vibrations at 1460 cm^{-1}.[37] The Si-C stretching vibration band appears at 834 - 810 cm^{-1}.

4.3.2.2.N_2 adsorption–desorption analysis:

The average pore diameter obtained by pore size distribution curve, calculated by the Barrett–Joyner–Halenda (BJH) model, the Brunauer–Emmett–Teller (BET) surface area and pore volume for MSN, functionalized MSNs and their composites with Eu and Y complexes are presented in the table 4.2.

Functionalized MSNs exhibit a smaller specific surface area and a smaller pore volume in comparison with the pure silica nanomaterial, which further confirms the successful functionalization of nanoparticles. The pore diameter increases after the surface modification arising from higher average pore diameter resulting due to occupying smaller pores with functional groups. The nitrogen adsorption isotherm of the MSN and surface modified mesoporous silica nanoparticles is shown in the figure 4.5 (a). It suggests a multi-stage adsorption process and show type IV isotherm characteristics. Isotherm shows an initial surface adsorption process, in which the nitrogen adsorption amount increases slowly up to relative pressure p/p_0= 0.85. In the pressure range of p/p_0 = 0.85–0.99, the adsorption amount of nitrogen sharply increases resulting from an enhanced adsorption in the larger pores.

Table 4.2: Pore structure parameters of MSN, functionalized MSNs, and their composites with either $Eu(dbm)_3phen$ or $Y(dbm)_3phen$ complex, derived from N_2 adsorption–desorption isotherms.

Sample	BET S.A.[a] (m^2/g)	SPATPV[b] (cm^3/g)	AAPD[c] (nm)
MSN	944	1.6	2.17
MSN-APTES	468	1.1	2.0
MSN-MPTMS	471	0.89	1.8
MSN-ETMS	908	1.5	1.99
MSN-Eu	442	1.0	2.0
MSN-APTES-Eu	132	0.94	1.8
MSN-MPTMS-Eu	150	0.7	1.8
MSN-ETMS-Eu	797	1.4	1.99
MSN-Y	388	1.09	2.16
MSN-APTES-Y	102	0.7	1.8
MSN-MPTMS-Y	112	0.66	1.8
MSN-ETMS-Y	722.8	1.48	2.15

a: BET specific surface area, b: BJH pore volume, and c: BJH average pore diameter.

When lanthanide complexes are incorporated into functionalized MSNs smaller specific surface areas and pore volumes are observed in comparison with those of functionalized and pure silica nanomaterial, which might be due to the presence of lanthanide complex on the surface as well as in the surface of pores (table 4.2). On the other hand, pore diameter increases after doping which is due to the fact that smaller pores are filled first with the lanthanide complex and then the larger pores resulting into higher average pore diameter, which further confirms that the lanthanide complex is encapsulated in the silica nanoparticles.

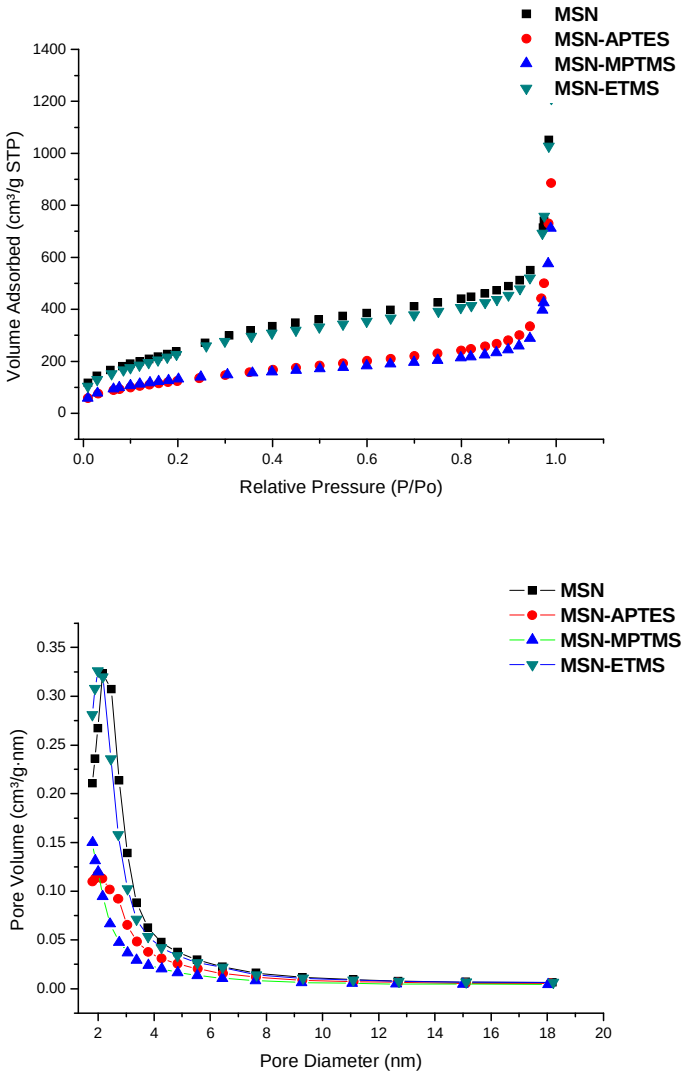

Figure 4.5: a) N_2 adsorption–desorption isotherms of MSN and functionalized MSNs; **b)** and corresponding pore size distribution curves determined by BJH method.

4.3.2.3.TEM images

Transmission electron microscopy (TEM) images of the bare MSN showed a typical morphology consisting of spherical to elliptical shapes with diameters ranging from 50 to 70 nm (figure 4.6). Representative TEM images of $Y(dbm)_3phen$ and $Eu(dbm)_3phen$ containing composites are shown in figure 4.7 (a) and (b).

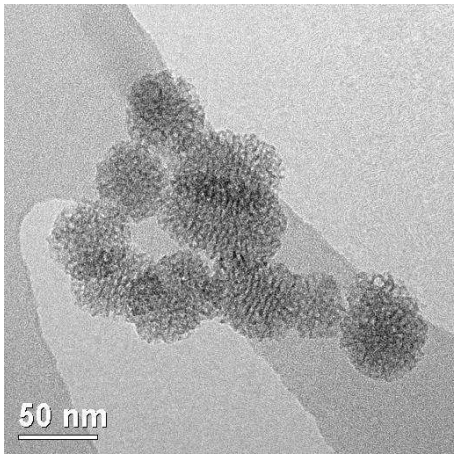

Figure 4.6: TEM micrograph of MSN powder.

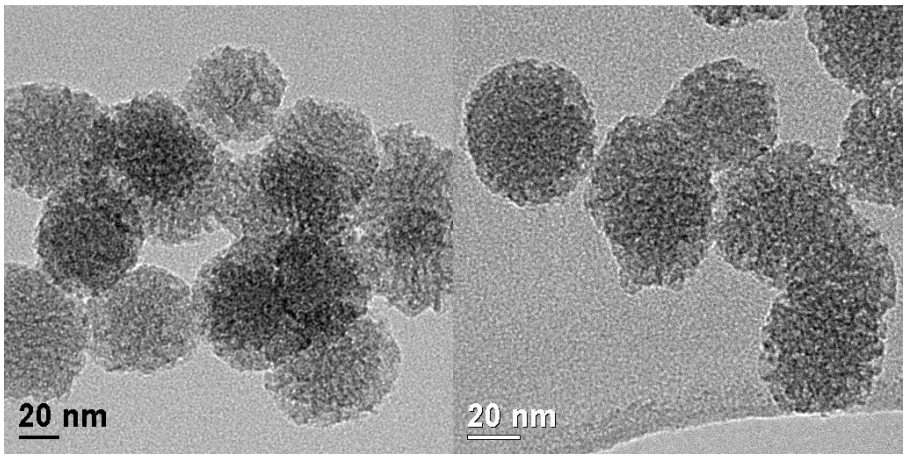

Figure 4.7: TEM images of (a) MSN-MPTMS-Eu and (b) MSN-MPTMS-Y samples.

4.3.2.4.Solid state NMR: ^{29}Si and ^{13}C spectra

In order to characterize the results of the surface-modification reactions of MSN with the different silanes and of the incorporation of the Y complex by the modified MSNs, ^{29}Si and ^{13}C spectra were recorded.

The ^{29}Si CPMAS spectra of MSN and the three functionalized MSNs are reported in figure 4.8.

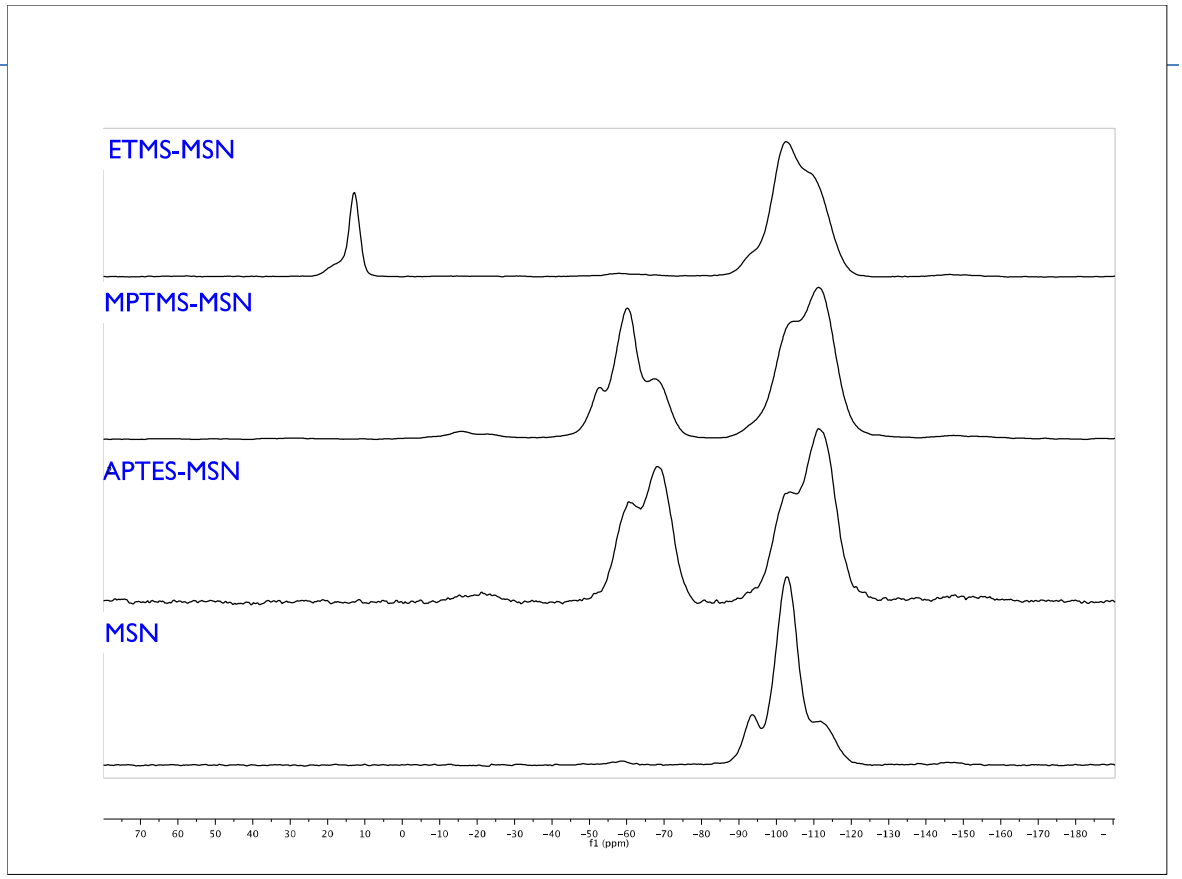

Figure 4.8: ^{29}Si CPMAS spectra of bare and functionalized MSNs. A MAS frequency of 3.5 kHz was used.

The assignment of the different peaks is straightforward: peaks at about -111, -103 and -93 ppm are due to Q^4, Q^3 and Q^2 silicon nuclei, respectively; peaks at about -68, -61, and - 53 ppm to T^3, T^2 and T^1 silicon nuclei; peaks at about 13 and 17 ppm to M^1 and M^0 silicon nuclei. The letter indicates the number of oxygen atoms directly bonded to a given silicon atom (4, 3, and 1 for Q, T, and M): it is interesting to note that all Q signals arise from silica (MSN), while all T signals are due to APTES or MPTMS, and all M signals to ETMS. Furthermore, the superscript close to each letter reflects the number of Si-O-Si bonds formed by each silicon nucleus. A ^{29}Si spectrum therefore allows us to detect all the possible silicon-species present in a sample. Moreover, from the integrals of the different signals it is possible to obtain: a) the relative ratio of the different silicon-containing species present in a sample; b) the degree of condensation (ratio between the number of Si-O-Si bonds and that of Si-O bonds) of each silicon-containing species. However, it must be pointed out that the integrals taken from CPMAS spectra cannot be straightforwardly considered quantitative in terms of number of silicon nuclei present in the sample. In order to obtain quantitative results much longer experiments (either Direct Excitation spectra with relaxation delays as long as 5 minutes or full CP dynamics curves) should be performed, which

was out of the scope of the present work. Nonetheless, provided that the spectra are recorded under the same conditions, we can draw some partially quantitative results by comparing the ratios between the integrals of the different peaks in the spectra of different materials.

In table 4.3, we report the integrals of the different peaks, as obtained from the deconvolutions of CPMAS spectra.

In the spectrum of MSN, as expected, only Q signals are observed, corresponding to fully condensed ($\underline{Si}(OSi)_4$) silicon atoms (Q^4), single silanols ($\underline{Si}(OSi)_3OH$) (Q^3) and geminal silanols ($\underline{Si}(OSi)_2(OH)_2$) ($Q^2$). The strong presence of single silanols is evident, but, on the other hand, it must be considered that signals of protonated species are intrinsically favored in CPMAS spectra. In the ^{29}Si spectrum of APTES-MSN we can observe the appearance of the signals due to T silicon nuclei of APTES; it is also evident a strong decrease of the silanol signals of MSN, especially that of Q^3, corresponding to an increased condensation degree that passes from 0.76 to 0.91 (table 4.3). These results confirm the occurrence of the grafting reaction of APTES to MSN.

Table 4.3: Areas underlying the different peaks of ^{29}Si CPMAS spectra, as obtained from spectral deconvolutions. For each group of silicon sites it is also reported the condensation degree, i.e. the ratio between the number of Si-O-Si bonds and that of Si-O bonds, calculated as $\sum_{k=1}^{i} kI_k / i\sum_{k=0}^{i} I_k$, with i=4,3,1 for Q, T and M, respectively, where I is the area of the corresponding peaks. The maximum error on the peak areas is ±1.

Silicon site	MSN	APTES-MSN	MPTMS-MSN	ETMS-MSN
Q^4	19	38	37	45
Q^3	67	18	20	34
Q^2	14	2	3	6
Q c.d.	0.76	0.91	0.89	0.86
T^3	-	26	11	-
T^2	-	15	22	-
T^1	-	1	7	-
T c.d.		0.87	0.7	
M^1	-	-	-	12
M^0	-	-	-	3
M c.d.				0.8

Moreover, we can observe that the condensation degree of APTES, which reasonably arises from both the grafting to silica and the self-condensation between APTES molecules[38-40] is quite high. The absence of a T^0 signal allows us to rule out the presence of unreacted APTES.

In MPTMS-MSN, the condensation degree of the Q silicon's is very similar to that of APTES-MSN. On the other hand, the T region is different, showing increased T^2 and T^1 signals, corresponding to a T condensation degree that passes from 0.87 in APTES-MSN to 0.7 in MPTMS-MSN. Therefore, although also in this case no unreacted MPTMS is present, MPTMS shows a much lower degree of condensation than APTES. This result and the similar degree of

condensation of silica in the two samples can be explained with a lower self-condensation of MPTMS with respect to APTES.

The MSN condensation degree in ETMS-MSN is lower (0.86) than in the previous cases, mostly because of the lower number of potential condensation sites in ETMS (1) with respect to APTES and MPTMS (3). Moreover, the presence of a small M^0 signal (about 17 ppm) indicates that part of unreacted ETMS remained entrapped in the solid MSN.

^{13}C CPMAS and DE-MAS spectra have been recorded for both the three modified MSNs and the three composites containing APTES, MPTMS and ETMS (see figures 4.9-4.11). In APTES-MSN all the signals can be easily assigned to APTES carbons: the peaks at 15 and 58 ppm arise from unhydrolyzed ethoxy groups of either TEOS or APTES. The comparison between CPMAS and DE-MAS spectra indicates that both ethoxy and APTES propyl groups are very mobile. In the CPMAS spectrum of the corresponding composite, the peaks of the complex are clearly recognizable (120-170 ppm), confirming that the complex was successfully incorporated into the pore structures of the MSN matrix. However, as far as complex resonances are concerned, no differences could be detected between the spectrum of the pure complex and that of APTES composite. From the DE-MAS spectrum of the composite it is possible to see that the benzoyl groups of the complex remain very mobile also in the composite.

Similar considerations can be done for MPTMS-MSN and its corresponding composite (figure 4.10): in the CPMAS spectrum of MPTMS-MSN the signals of the three carbon nuclei of the mercaptopropyl group can be clearly recognized, along with that, at about 49 ppm, due to unhydrolyzed methoxy groups. An unidentified signal at about 41 ppm could possibly arise from a reactant used in the preparation of MPTMS-MSN, n-propylamine. All these carbon nuclei are in mobile environments, as shown by the comparison with the corresponding DE spectrum. It is interesting to notice that in this case the absence of signals at about 15 and 58 ppm indicates that no residual ethoxy groups from unhydrolyzed TEOS are present. The spectra of the corresponding composite appear slightly more crowded, not only for the presence of the signals of the complex, but also of other signals (e.g. 37 ppm), possibly due to hexane residues.

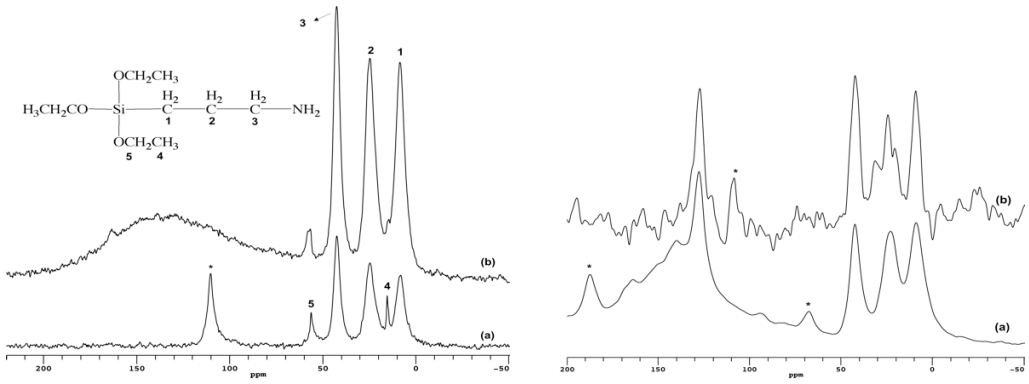

Figure 4.9: On the left: ^{13}C MAS spectra of APTES-MSN (a) DE with a recycle delay of 2 s (b) CP. Both the spectra were acquired with a spinning frequency of 5.5 kHz. The signal marked with asterisk in DE spectrum and the broad signals present in CP spectrum are due to incomplete suppression of probe background signal. On the right: ^{13}C MAS spectra of APTES-MSN/Y(dbm)$_3$phen composite (a) CP acquired with a MAS frequency of 6 kHz (b) DE with a recycle delay of 2 s and MAS frequency of 15 kHz. The spinning sidebands and background signal at ≈ 110 ppm are marked with asterisks.

In figure 4.11, the CPMAS spectrum of ETMS-MSN shows three peaks at -2.6, 15 and 58 ppm, the first being ascribable to ETMS methyl carbons, and the other two to the ethoxy groups of unhydrolyzed TEOS and/or of unreacted ETMS, whose presence has been detected by ^{29}Si NMR, as previously discussed. By comparison with the DE-MAS spectrum of ETMS-MSN, we can see that all of these carbons are in mobile environments. In the CPMAS spectrum of the composite, signals from both ETMS and complex components can be recognized, confirming the successful impregnation. Moreover, by comparison with the DE-MAS spectrum, it is possible to observe that both ETMS methyl groups and complex benzoyl groups are in mobile environments within the composite.

Thus, SSNMR study confirms the surface functionalization of MSNs and the successful incorporation of the rare-earth complex in the silica nanomaterial.

4.3.2.5.Solid state NMR: relaxation times

In order to try to obtain more specific dynamic information, ^{1}H and ^{13}C spin-lattice relaxation times (T_1), sensitive to motions in the MHz-GHz regime, have been measured using either low-

and high-resolution techniques. ^{1}H T_1's are strongly affected by the spin diffusion process, which tends to average them to a single value. On the contrary, ^{13}C T_1's are not affected by spin diffusion since ^{13}C is a rare nucleus, and therefore they contain site-specific dynamic information.

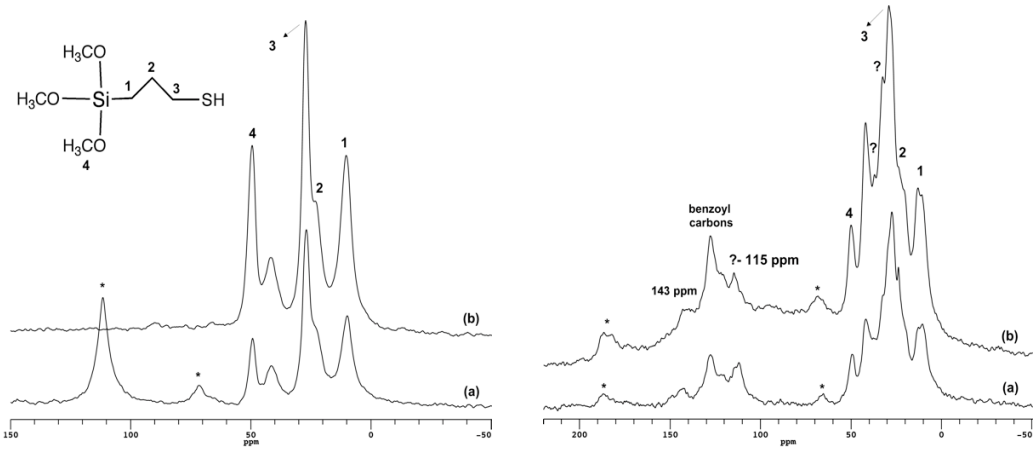

Figure 4.10: On the left: ^{13}C MAS spectra of MPTMS-MSN **(a)** DE acquired with a recycle delay of 2 s, and **(b)** CP. Both spectra were recorded with a spinning frequency of 4 kHz. The signals from background are marked with asterisks. On the right: ^{13}C MAS spectra of MPTMS-MSN/Y(dbm)$_3$phen composite **(a)** DE acquired with recycle delay of 2 s **(b)** CP. Both the spectra were recorded with a spinning frequency of 6 kHz. Spinning sidebands are marked with asterisks.

For all samples, the ^{1}H T_1 relaxation trends were always well reproduced by a monoexponential trend, indicating a complete averaging carried out by the spin-diffusion process. The proton T_1's measured at different temperatures in the range 20-70 °C are reported in figures 4.12-4.14. It is possible to notice how the trends for the complex and for the three modified MSN's are always increasing with increasing temperature, indicating that the motions mostly contributing to the relaxation are in the "fast-motional side" of the T_1 curve, i.e. they have a characteristic frequency higher than the proton Larmor frequency (400 MHz). Moreover, the values measured for the three modified MSNs are always much less than those of the complex, which means that the motions contributing to T_1 in the modified MSNs have a characteristic frequency closer to 400 MHz than those present in the complex. We will try to understand which motions are mostly responsible for proton T_1 relaxation in the following, when ^{13}C T_1 data will be discussed. In

order to understand whether a change in the MHz-GHz dynamics of both complex and silanes moieties takes place in passing from modified MSN and complex to the composite, which could be a proof of interactions between the two components, we compared the experimental T_1's measured for the composites with those "calculated" from the T_1's of the single components hypothesizing that no changes in motions occur, and estimating the fraction of protons of the modified MSN ($w_{H,\mathrm{mod}MSN}$) and complex ($w_{H,complex}$) in the composite as described in the note.1

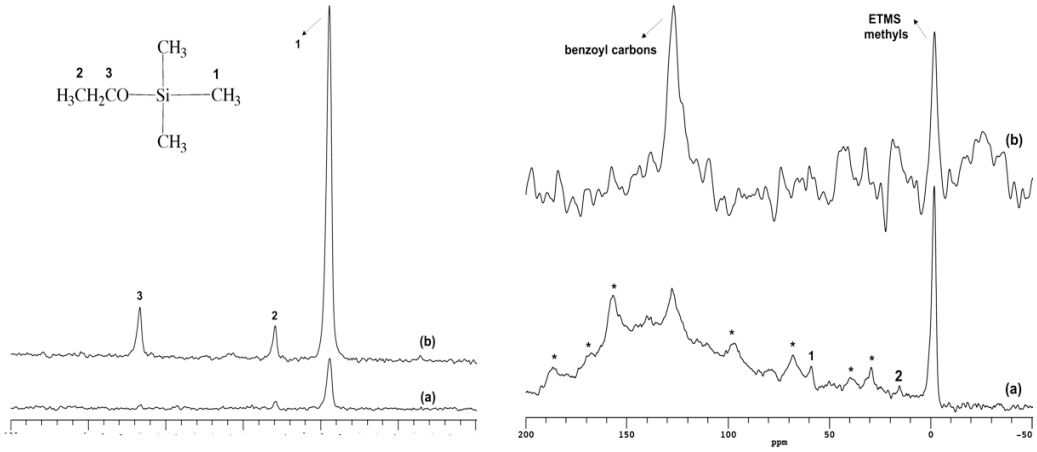

Figure 4.11: On the left: ^{13}C MAS spectra of ETMS-MSN **(a)** DE acquired with a recycle delay of 2 s, **(b)** CP. Both experiments were recorded with a spinning frequency of 3 kHz.

On the right: ^{13}C MAS spectra of ETMS-MSN/Y(dbm)$_3$phen composite **(a)** CP acquired at 3 kHz of spinning frequency **(b)** DE acquired with recycle delay of 2 s and spinning frequency of 15 kHz. Spinning sidebands are marked with asterisks.

$$\frac{1}{T_{1,calc}} = \frac{w_{H,complex}}{T_{1,complex}} + \frac{w_{H,\mathrm{mod}\,MSN}}{T_{1,\mathrm{mod}\,MSN}}$$

It is possible to see from figures 4.12-4.14 that in all cases the experimental values are of the same order of magnitude of the calculated ones, indicating that no dramatic changes in the dynamics should occur. However, the trend of experimental and calculated T_1's *vs* temperature is

1 The relative fractions of protons of silica, of the organic modifier and of the Yttrium complex in the three different composites were roughly calculated estimating the relative amount of complex and modifier from ^{13}C CPMAS spectra (from the ratio between the integrals of representative signals) and the relative amount of silica and modifier from the ratio between the integrals of Q and T or M signals in the ^{29}Si CPMAS spectra; for both silica and modifiers the protons content was calculated by taking into account their condensation degree and assuming full hydrolysis of the modifier and neglecting the water possibly adsorbed on silica.

clearly different, in all the three cases the increase with temperature being much steeper for the calculated values. This suggests that the motions mostly responsible for T_1 relaxation, presumably those occurring in the modified MSN's, do experience a partial slowering as a consequence of the interaction with the complex.

The measurement of ^{13}C T_1's allowed some additional considerations to be drawn. First of all it must be stated that, in the case of ^{13}C, the spin-lattice relaxation decay is not mono-exponential, and two or three exponential functions are needed to reproduce the experimental decays. This greatly complicates the analysis of the experimental data, so we choose to discuss ^{13}C T_1's in terms of 1/PWRA, i.e. the inverse of the population weighted relaxation rate (PWRA):

$$PWRA = \sum_i \frac{w_i}{T_{1,i}}$$

where the sum runs over the number of exponentials, and the i-th exponentials has a fractional weight w_i and a relaxation time $T_{1,i}$.

All the experimental data and calculated 1/PWRA's are reported in table 4.4.

Table 4.4: Values of ^{13}C T_1 (each component is reported with its weight percentage) and 1/PWRA as obtained at room temperature for all samples. C_{benz} refers to the complex carbon nuclei resonating at 128 ppm.

T_{1a}(s)	T_{1b}(s)	1/pwra	T_{1a}(s)	T_{1b}(s)	1/pwra	T_{1a}(s)	T_{1b}(s)	1/pwra	T_{1a}(s)	T_{1b}(s)	1/pwra
wa %	wb%	(s)	wa %	wb%	(s)	wa %	wb%	(s)	wa %	wb%	(s)
Y COMPLEX											
C_{benz}											
0.86	24.0	1.73									
48	52										
APTES-MSN											
			C1			C2			C3		
			0.42	2.6	0.60	0.45	2.5	0.53	0.59	6.9	0.67
			60	40		70	30		89	11	
Y COMPLEX/APTES-MSN COMPOSITE											
C_{benz}			C1			C2			C3		
0.97	22.5	1.57	0.44	4.2	0.64	0.12	1.6	0.28	0.50	2.7	0.65
60	40		59	41		31	69		72	28	
MPTMS-MSN											
			C1			C2			C3		
			0.64	3.3	0.71	0.29	1.1	0.35	0.88		
			87	13		78	22		100		
Y COMPLEX/MPTMS-MSN COMPOSITE											
C_{benz}			C1			C2			C3		
0.57	9.8	0.85	0.61	4.1	0.73	0.46	1.4	0.59	0.58	4.49	0.61

65	35		81	19		68	32		95	5	
ETMS-MSN											
			C1								
			5.3								
			100								
Y COMPLEX/ETMS-MSN COMPOSITE											
C_{benz}			C1								
0.67	15.3	1.04	4.2								
63	37		100								

All the relaxation times, for both complex and modified MSN carbons, remain of the same order of magnitude in passing from pure components to the corresponding composite, indicating that no dramatic change in MHz dynamics occurs. Detectable changes can be observed for carbons C2 in APTES-MSN, C2 and C3 in MPTMS-MSN, which are, however, difficult to be rationalized. As far as benzoyl carbons of the complex are concerned, their T_1 decrease in passing from the pure complex (1.73 s) to the three composite, and particularly to those with MPTMS (0.85 s) and with ETMS (1.04 s). In order to understand if this could be interpreted as a slowering or a fastening of the benzoyl motions, we measured ^{13}C T_1 of the benzoyl carbons in the complex at different temperatures (data not shown), observing that T_1 (1/PWRA) was decreasing with increasing temperature. This means that the motion mainly responsible for ^{13}C T_1 relaxation is actually in the "slow motional side" of the T_1 curve, i.e. it has a characteristic frequency lower than 100 MHz, the ^{13}C Larmor frequency. Since this trend is opposite to that observed for ^{1}H T_1, this means that two different types of motions contribute to ^{1}H and ^{13}C T_1 relaxation: we can tentatively identify the slower motion (contributing to ^{13}C relaxation) with the reorientations of the benzoyl group, and the faster motion (contributing to ^{1}H relaxation) with some libration of the same group. However, this is a merely speculative hypothesis, which would need further proofs. All this considered, the decrease of ^{13}C T_1 in passing from pure complex to the composites can be interpreted as a fastening of the reorientational motions of the benzoyl rings, possibly as a consequence of the dispersion of the complex within the modified MSN.

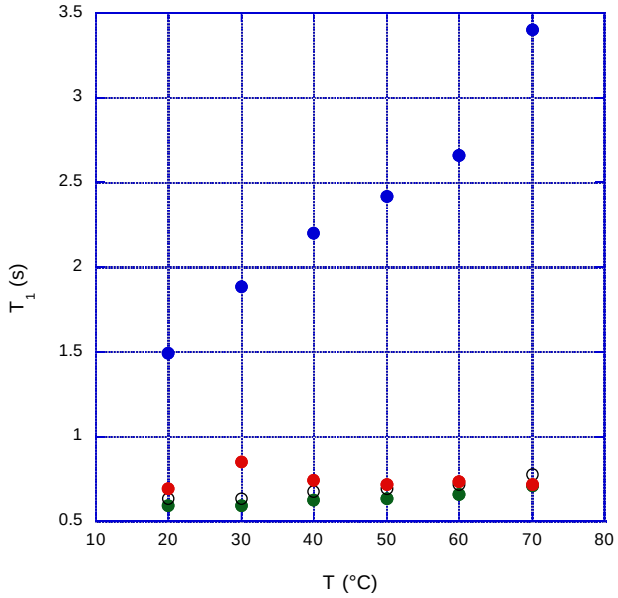

Figure 4.12: Trend of ^{1}H T_1 vs. temperature for: $Y(dbm)_3phen$ (blue circles), APTES-MSN (green circles), APTES-MSN/$Y(dbm)_3phen$ composite (red circles), and corresponding $T_{1,calc}$ (empty circles).

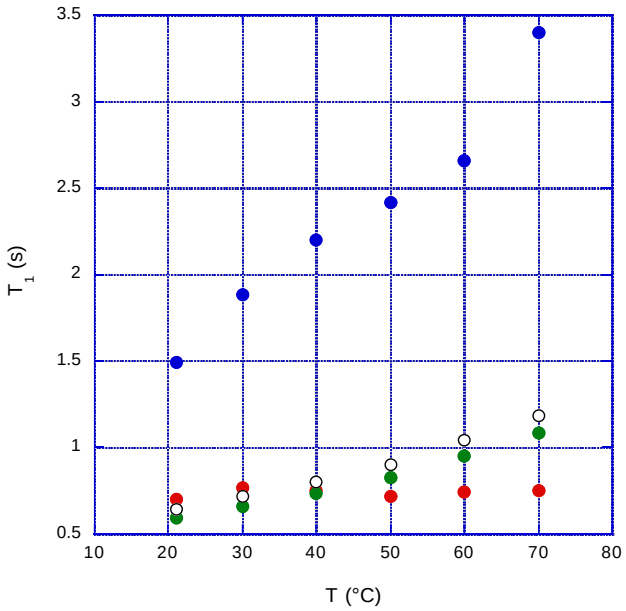

Figure 4.13: Trend of ^{1}H T_1 vs. temperature for: $Y(dbm)_3phen$ (blue circles), MPTMS-MSN (green circles), MPTMS-MSN/$Y(dbm)_3phen$ composite (red circles), and corresponding $T_{1,calc}$ (empty circles).

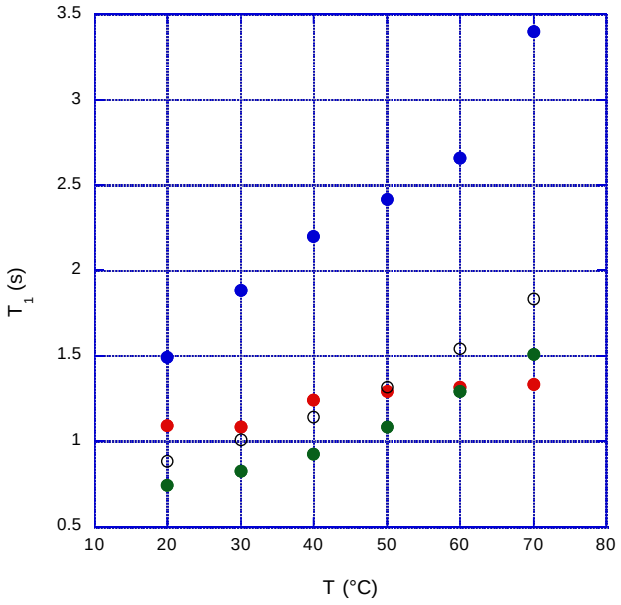

Figure 4.14: Trend of ^{1}H T_1 vs. temperature for: $Y(dbm)_3phen$) (blue circles), ETMS-MSN (green circles), ETMS-MSN/$Y(dbm)_3phen$ composite (red circles), and corresponding $T_{1,calc}$ (empty circles).

4.3.2.6.UV-reflectance measurements:

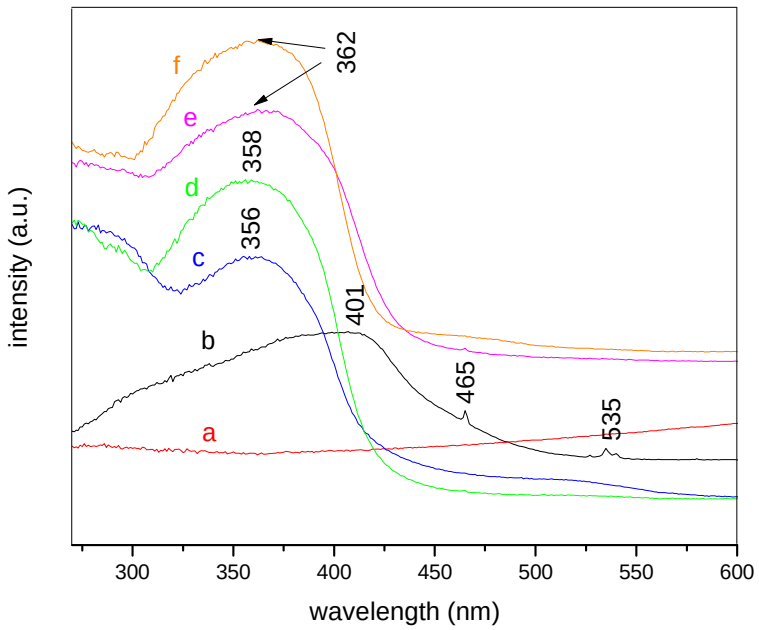

Figure 4.15: UV visible diffuse reflectance spectra of MSN (a), pure Eu(dbm)$_3$phen (b), MSN-Eu (c), MSN-ETMS-Eu (d), MSN-MPTMS-Eu (e), MSN-APTES-Eu (f).

The UV-Vis diffuse reflectance spectra of MSN, Eu(dbm)$_3$phen complex, and composites formed by the latter with unmodified and modified MSNs are shown in figure 4.15. The Eu(dbm)$_3$phen complex show a broad absorption band in the region 225 to 450 nm with the maxima centered at 401 nm. In all the composites the absorption bands of the complex are narrower and shifted toward shorter wavelengths, with maxima at 356-362 (figure 4.15 (c), (d), (e), (f). The shift in the absorption towards shorter wavelength observed in the composite materials indicates the change in the polarity of surroundings of the Eu^{3+} ion, confirming the encapsulation of Eu(dbm)$_3$phen in the pore structures of surface modified as well as unmodified MSNs.[41]

4.3.2.7.Photoluminescence properties:

Photoluminescence (PLE) excitation and emission (PL) spectra of the Eu(dbm)$_3$phen are given in figure 4.16 (a) and (b). The excitation spectrum in figure 4.16 (a) was obtained by monitoring

emission at 611 nm and the emission spectrum in figure 4.16 (b) was collected by excitation at 412 nm.

PL excitation is directly related to the absorption of the luminescent system and therefore to the upper electronic energy levels and presents the maximum value around 412 nm. Moreover it shows a specific peak at 464 nm. The excitation band is due to the absorption of the ligands, while the peak is due to the direct f–f electron transition of Eu^{3+} ions, as reported in the graph.

The emission spectrum shows five signals peaked at 579, 591, 611, 652 and 704 nm due to transitions between the $^5D_0$ excited state and the different ^7F_J levels (J = 0, 1, 2, 3, 4, 5).

Due to the weakness of the electric dipole transitions which are parity-forbidden ("Laporte-forbidden") the magnetic dipole transitions, which are parity-allowed, can be easily seen and are of comparable intensity.[42] For Eu^{3+}, the $^5D_0 - {}^7F_j$ transitions are predominantly electric dipole for j even, completely magnetic dipole for j odd. The intensities of electric dipole transitions, in particular for j = 0 and for j = 2, are strongly sensitive of the rare earth surrounding environment, being absent in high symmetry sites, while the intensities of magnetic dipole transitions are almost independent of the environment. In the emission spectrum, the $^5D_0 - {}^7F_0$ transition is clearly visible, indicating a low symmetry of the site occupied by Eu^{3+} ions. This is also confirmed by the fact that the intensity of the $^5D_0 - {}^7F_2$ transition is high with respect to the other lines.

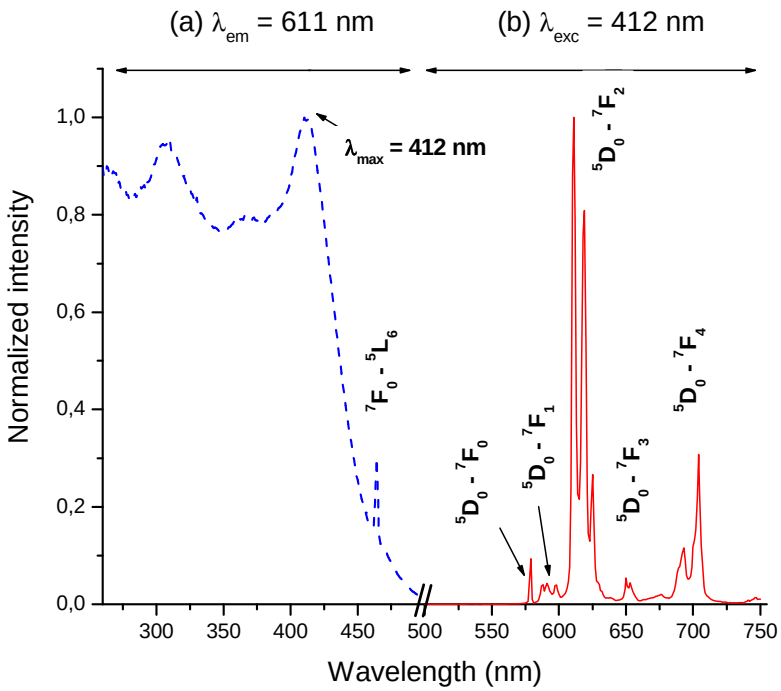

Figure 4.16: Excitation (a) and emission spectra (b) of pure Eu(dbm)$_3$phen in solid state.

Photoluminescence excitation and emission spectra of the rare-earth complex encapsulated into unmodified MSNs and into surface-functionalized MSNs is presented in figure 4.17 (a) and 4.17 (b) respectively. All the samples containing Eu(dbm)$_3$phen complex shows a strong red luminescence upon irradiation with UV light. The maximum absorption was found from the excitation spectrum to be at around 397 nm for the Eu(dbm)$_3$phen in all the functionalized silica samples as well as in the unmodified silica sample. This blue shift in the excitation band at 412 nm for pure rare earth complex to 397 nm for all the silica samples is attributed to the constrain induced by the rigidity of the environment surrounding the molecule. This causes an energy increase in the excited state electronic levels of the system.

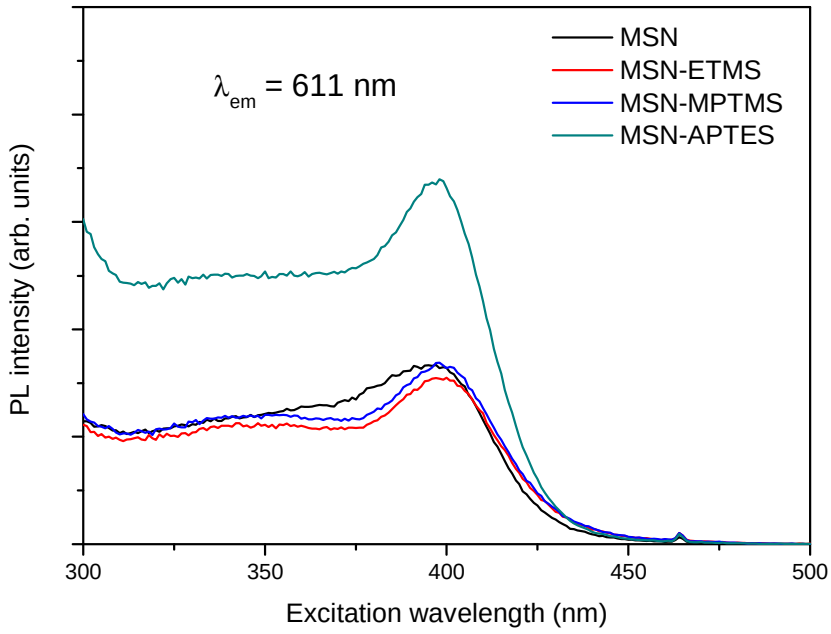

Figure 4.17 (a) Photoluminescence excitation spectra of $Eu(dbm)_3phen$ encapsulated into unmodified MSNs and surface functionalized MSNs.

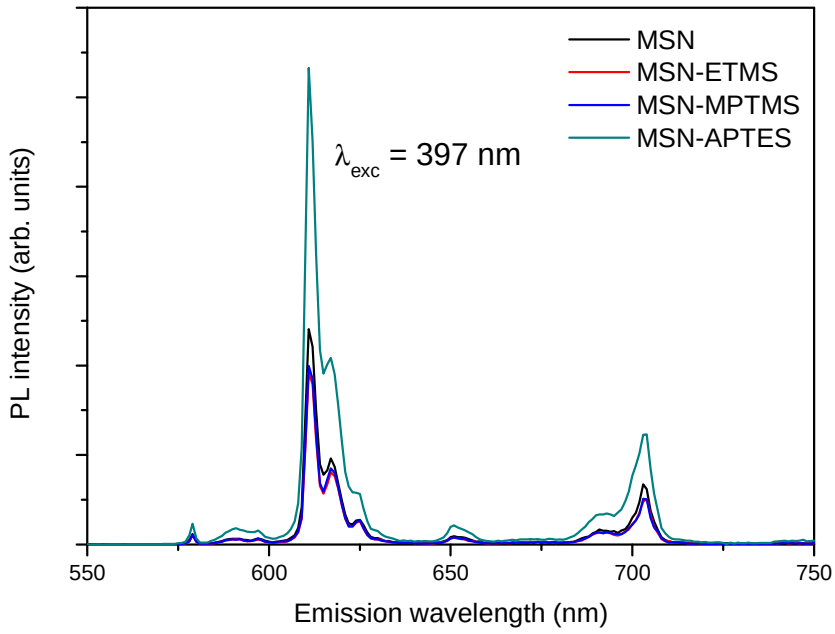

Figure 4.17 (b) Photoluminescence emission spectrum of the $Eu(dbm)_3phen$ encapsulated into unmodified MSNs and surface functionalized MSNs.

On the other hand, the emission spectrum is very similar to the one of pure $Eu(dbm)_3phen$ complex although a notable difference between band widths for the emission spectra of pure complex and the one incorporated in MSNs has been observed. The incorporation of complex in the silica matrix changes the environment around Eu^{3+} that affects the electronic transitions. As a result, the non homogeneous environment around the Eu^{3+} gives rise to band broadening in the emission spectra. Among all, the hypersensitive transition $^5D_0 - {}^7F_2$ is the most intense and it is peaked at 611 nm.

The photoluminescence intensity of the $Eu(dbm)_3phen$ complex reported in figure 4.18 (a) and (b) is very similar for MSN, MSN-ETMS and MSN-MPTMS, while it increases for MSN-APTES. In order to get better insight into this behavior some considerations about the site symmetry and the quantum efficiencies of the Eu^{3+} ions have been done.

Looking at the emission spectra, it should be noted that all the samples show only one peak due to $^5D_0 - {}^7F_0$ transition (579 nm), which implies that all the Eu^{3+} ions occupy a site of the same

symmetry.[43-44] Moreover, the ratio (R) between the intensity of the $^5D_0 - {}^7F_2$ (601 - 640 nm) and the $^5D_0 - {}^7F_1$ (580 - 601 nm) transitions can be used as an indicative measure of the asymmetry of the coordination polyhedron of the Eu^{3+} ion. In particular, the later transition is a pure magnetic dipole transition, impervious to the effects of the surrounding crystal field, while the former one is a hypersensitive-forced electric dipole transition allowed only at low symmetries with no inversion centre.[45-46]

The intensity ratios R for the pure complex and for the MSN, MSN-ETMS, MSN-MPTMS, MSN-APTES samples are 16.7, 18.6, 18.2, 18.0 and 16.5 respectively. These numbers are quite high, and very similar for all samples suggesting that the site symmetry for the Eu^{3+} ions is not changed and that the complex should have been preserved in the incorporation process into the mesoporous silica nanoparticles.[43] Indeed, as a comparison similar calculations have been reported for Eu^{3+} ions in an amorphous matrix both as a bulk and incorporated into mesoporous silica nanoparticles, obtaining much lower values around 4.5.[47]

Three crystal field levels are observed for the $^5D_0 - {}^7F_1$ transition at 591 nm which indicates lower site symmetry for the Eu^{3+} in the functionalized and unmodified MSNs.

The complex show higher $^5D_0 - {}^7F_2$ / $^5D_0 - {}^7F_1$ band intensity ratio on its incorporation into the pore structures of unmodified as well as surface modified MSNs. This change reflects the increase of the $^5D_0 - {}^7F_2$ emission band intensity and the decrease of the other emission bands due to the increase in the induced electric dipole interactions.[48] Also; all the other induced electric dipole transitions are much weaker than the $^5D_0 - {}^7F_2$ transition.

Among all the samples, the complex show highest intensity corresponding to the $^5D_0 - {}^7F_2$ transition of the complex in the APTES functionalized MSNs. This enhancement of the $^5D_0 - {}^7F_2$ transition intensity is most likely due to hydrogen bonding interaction of the $-NH_2$ protons of MSN-APTES with the coordinating oxygen atoms of the incorporated rare earth complex. On the other hand, the intensity of $^5D_0 - {}^7F_2$ transition of the complex seems to decrease in the ETMS and MPTMS functionalized MSNs. Also, the complex show similar $^5D_0 - {}^7F_2$ transition intensity in the ETMS and MPTMS functionalized MSNs. The decrease in the intensity can be possibly due to the absence of hydrogen bonding between the coordinating oxygen atoms of the complex with the $-(CH_3)_3$ and –SH groups grafted on the MSNs.

Due to the interactions of incorporated complex with the surrounding $–NH_2$ functional groups in the pore structures of the APTES-MSN, the symmetry of the rare-earth molecule is no longer held, resulting into an enhancement of the induced electric dipole transitions and depression of the magnetic dipole transitions. The $^5D_0 – {}^7F_2$ transition is the prominent peak due to the much less increase of the $^5D_0 – {}^7F_0$ and, $^5D_0 – {}^7F_4$ transitions as compared to $^5D_0 – {}^7F_2$ transition.

4.3.2.8.Lifetime measurements:

The $^5D_0$ decay curves for the pure $Eu(dbm)_3phen$ complex, $Eu(dbm)_3phen$ incorporated MSNs and $Eu(dbm)_3phen$ doped functionalized MSNs are shown in figure 4.18. The lifetime measurements were performed at 611 nm under the excitation wavelength of a LED source at 377 nm. The decay curves were fitted by a single exponential and the lifetime values for all the composites are listed in table 4.4.

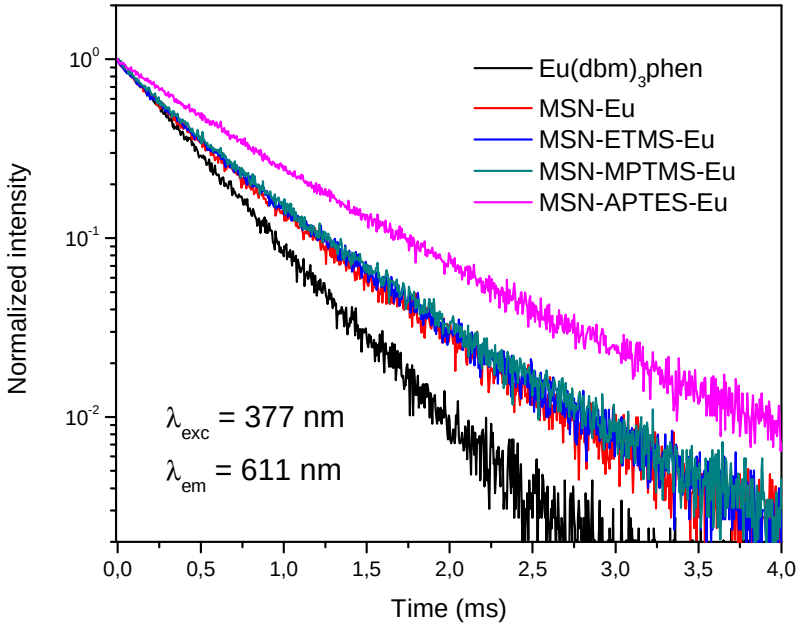

Figure 4.18: Photoluminescence decay curves for pure rare earth complex, MSN-Eu, MSN-APTES-Eu, MSN-MPTMS-Eu, and MSN-ETMS-Eu.

The results are in agreement with the presence of one kind of site of Eu^{3+} ions in these solid samples. Moreover, the lifetime values are also in agreement with the photoluminescent

intensities previously described showing a very similar lifetime value for the MSN, MSN-MPTMS and MSN-ETMS samples and a longer lifetime value for the APTES-MSN sample. A possible explanation for the different lifetime values of Eu^{3+} ions is attributable to some interaction taking place between incorporated complex and the different functional groups anchored on the surface modified MSNs. Indeed, the different strengths of interactions between the complex molecule and the functional groups grafted on the surface of silica matrix alter the strengths of the molecular vibrations and relaxation times.[48] These interactions slower the vibrations of the complex molecule and maximize the electron relaxation time resulting into a longer emission lifetime for Eu^{3+}. A longer lifetime has been noted for all the samples after complex incorporation into MSNs matrix.

The lifetimes of the excited rare-earth complex in these samples are 0.41 ms for the pure $Eu(dbm)_3phen$ complex, 0.73 ms for MSN-APTES-Eu, 0.53 ms for MSN-MPTMS-Eu, 0.53 ms for the MSN-ETMS-Eu, and 0.51 ms for the MSN-Eu. Lifetimes for Eu^{3+} in the samples follow the sequence of interaction strength. Among the three surface modified composites, MSN-APTES shows higher lifetime. The shorter lifetime for the MSN-Eu is related to the quenching effect of O–H oscillators on the surface of silica matrix.

The intrinsic quantum yield of the Eu(III) containing luminescent materials can be determined by using following formula.[49]

$$\phi_{Eu} = \frac{\tau}{\tau_{rad}} \qquad (4.1)$$

Where τ is the observed lifetime derived from the decay curves and τ_{rad} is the radiative lifetime. For the Eu^{3+} complexes, the radiative lifetime (τ_{rad}) can be calculated using equation (4.2), assuming that the energy of the $^5D_0/^7F_1$ transition (MD) and its oscillator strength are constant.

$$\frac{1}{\tau_{rad}} = A_{MD,\,0}\, n^3 \frac{I(^5D_0 \rightarrow {}^7F_J)}{I(^5D_0 \rightarrow {}^7F_1)} \qquad (4.2)$$

Where, $A_{MD,0}$ is the Einstein coefficient for spontaneous emission of the magnetic dipole transition $^5D_0 - {}^7F_1$ *in vacuo* which has a value of 14.65 s^{-1}, ($I(^5D_0 - {}^7F_J)/I(^5D_0 - {}^7F_1)$) is the ratio of the total integrated intensity of the corrected Eu^{3+} emission spectrum to the integrated

intensity of the $^5D_0/^7F_1$ transition and n is the refractive index of the medium. An index of refraction equal to 1.5 was considered for all the nanocomposites.

The internal quantum yields of the samples (ϕ_{Eu}), obtained as the rate between the measured lifetime and the calculated radiative lifetime, is reported in table 4.4. It is worth observing that after incorporation into the pores of MSNs the internal efficiency has a very good improvement (in particular for APTES functionalized silica the internal efficiency is close to 90%). This behavior is in agreement with the hypothesis that the silica matrix can protect the rare earth complex improving the optical performances.

Nevertheless, the evaluation of the external quantum yields (ϕ_{ext}) highlights a dramatic decrease of the total efficiency of the system after incorporation into the MSNs. The external quantum efficiencies of the samples have been measured at 397 nm excitation by using an integrating sphere and calculating the rate between the total number of emitted photons and absorbed photons. This strong reduction with respect to the internal ϕ_{Eu} can be mostly attributed to the scattering and absorption losses of the silica nanopowders, which can absorb and disperse the excitation light into non radiative processes and puts some limitations to the capability of exploitation of the system optical improvement previously discussed. Therefore we can infer that in real applications ϕ_{ext} will be critically determined by the incorporation and dispersion of the nanopowders in proper hosts and the optimization of this process will make possible the realization of high performing materials.

Table 4.5: photoluminescence data of $Eu(dbm)_3phen$, MSN-Eu, MSN-ETMS-Eu, MSN-MPTMS-Eu, MSN-APTES-Eu solid samples.

	$Eu(dbm)_3phen$	MSN-Eu	MSN-ETMS-Eu	MSN-MPTMS-Eu	MSN-APTES-Eu
ν_{00} (cm^{-1})	17271	17271	17271	17271	17271
ν_{01} (cm^{-1})	16920	17006	16949	16891	16920
ν_{02} (cm^{-1})	16366	16340	16340	16340	16340
ν_{03} (cm^{-1})	16385	15314	15338	15361	15361
ν_{04} (cm^{-1})	14205	14265	14225	14225	14205
I_{02}/I_{01} (R)	16.7	18.6	18.2	18.0	16.5
τ (ms)	0.41	0.51	0.53	0.53	0.73
τ_{rad}	0.82	0.74	0.75	0.76	0.83
$\Phi_{Eu.}$ (%)	50	69	71	70	88
Φ_{ext} (%)	26[2]	1.2	1.6	3.4	5.5

The decrease in the ^{13}C T_1 relaxation for the composite materials as compared to the pure complex suggests possible interactions between the complex molecule and the functional groups grafted on the surface of MSNs. An improvement in the luminescence properties was observed for the encapsulated $Eu(dbm)_3phen$ complex in the functionalized MSNs samples in the order MSN < MSN-ETMS < MSN-MPTMS < MSN-APTES. All these results indicate that there is some interaction taking place between the encapsulated rare earth complex and the different functional groups grafted on the surface of MSNs.

4.4. Conclusions:

In this paper, detailed study on encapsulation of $Eu(dbm)_3phen$ in unmodified and surface modified MSNs and the effect of different chemical environment on the photophysical properties of the complex is discussed. It was found that surface modification had a great deal of impact on the luminescence of the encapsulated $Eu(dbm)_3phen$ complex. Among the studied functionalized silica samples, complex showed a very high luminescence in APTES-MSN. Lifetime measurements showed that the complex exhibits longer lifetime in surface functionalized MSNs than pure complex in solid state. However, further studies will be needed to understand the effect

[2] QY of 4.9% has been reported for Eu(dbm)3phen complex in MeCN solution by Binnemans et. al.[50] In this study, the QY measurement on the pure complex was performed by physically dispersing the same quantity of complex as that impregnated in all the MSN samples.

of degree of functionalization on the encapsulated rare earth complex. SSNMR studies on the composites of diamagnetic complex doped functionalized MSNs indicate that some interactions are taking place between ligands of the complex and the functional groups grafted on the surface of MSNs. Surface functionalization changes the chemical environment inside the pore structures of MSNs. The encapsulation of $Eu(dbm)_3phen$ complex in these functionalized MSNs change symmetry of the complex due to interactions with the local chemical environment.

It can be concluded that the resulting hybrid mesoporous materials exhibits the characteristic emission of Eu^{3+} ions under UV irradiation with a higher $^5D_0$ luminescence quantum efficiency and longer lifetimes than the corresponding complex in unmodified MSNs.

4.5. References:

[1] Lin Jun, Su Qiang, Mater. Chem. Phys., 1994, 38, 98-101.

[2] E. Banks, Y. Okamoto and Y. Ueba, J. Appl. Polym. Sci., 1980, 25, 359-368.

[3] Sing Yan, Hong-Jie Zhang and Jia-Zuan Ni, Chin. J. Chem., 1997, 15, 242-249.

[4] Michael P. Bailey, Bernard F. Rocks and Clifford Riley, Analyst, 1984, 109, 1449-1450.

[5] Lowell Matthews R., Edward T. Knobbe, Chem. Muter., 1993, 5, 1697-1700.

[6] S. I. Weissman, J. Chem. Phys., 1942, 10, 214-217.

[7] Hananel Mack, Renata Reisfeld, David Avnir, Chem. Phys. Lett., 1983, 99, 238-239.

[8] R. Campostrini, G. Carturan, M. Ferrari, M. Montagna and O. Pilla, Journal of Materials Research, 1992, 7, 745-753.

[9] Tetsuro Jin, Satoshi Inoue, Shuji Tsutsumi, Ken-ichi Machida, Gin-ya Adachi, Journal of Non-Crystalline Solids, 1998, 223, 123-132.

[10] Bing Yan, Hong-jie Zhang, Shu-bin Wang, Jia-zuan Ni, Journal of Photochemistry and Photobiology A: Chemistry, 1998, 112, 231-238.

[11] D. Dong, S. Jiang, Y. Men, X. Ji, B. Jiang, Adv. Mater., 2000, 12, 646-649.

[12] Takashi Sawada, Shinji Ando, Chem. Mater., 1998, 10, 3368-3378.

[13] Junji Kido, Hiromichi Hayase, Kenichi Hongawa, Katsutoshi Nagai, and Katsuro Okuyama, Appl. Phys. Lett., 1994, 65, 2124-2126.

[14] Ronghu Wu, Huazhang Zhao, Qingde Su, Journal of Non-Crystalline Solids, 2000, 278, 223-227.

[15] Xiang Ling Ji, Bin Li, Shichun Jiang, Dewen Dong, Hong Jie Zhang, Xia Bin Jing, Bing Zheng Jiang, Journal of Non-Crystalline Solids, 2000, 275, 52-58.

[16] Lianshe FU, Hongjie Zhang, Philippe Boutinaud, 2001, 17, 293-298.

[17] Dongmei Wang, Junhu Zhang, Quan Lin, Lianshe Fu, Hongjie Zhang and Bai Yang, J. Mater. Chem., 2003, 13, 2279-2284.

[18] M. Fernandes, V. de Zea Bermudez, R. A. Sa´ Ferreira, L. D. Carlos, A. Charas, J. Morgado, M. M. Silva and M. J. Smith, Chem. Mater., 2007, 19, 3892. 91.

[19] C. Molina, K. Dahmouche, Y. Messadeq, S. J. L. Ribeiro, M. A. P. Silva, V. de Zea Bermudez and L. D. Carlos, J. Lumin., 2003, 104, 93. 92.

[20] C. Y. Peng, H. J. Zhang, J. B. Yu, Q. G. Meng, L. S. Fu, H. R. Li, L. N. Sun and X. M. Guo, J. Phys. Chem. B, 2005, 109, 15278.

[21] Q. Xu, L. Li, B. Li, J. Yu and R. Xu, Microporous Mesoporous Mater., 2000, 38, 351.

[22] G. Kickelbick, Angew. Chem. Int. Ed., 2004, 43, 3102-3104.

[23] G. Schulz-Ekloff, D. Wöhrle, B. van Duffel, R. A. Schoonheydt, Microporous Mesoporous Mater., 2002, 51, 91-138.

[24] Igor I. Slowing, Brian G. Trewyn, Supratim Giri, and Victor S.-Y. Lin, Adv. Funct. Mater., 2007, 17, 1225-1236.

[25] T. M. Chen, G. M. Brauer, J. Dent. Res., 1982, 61, 1439-1443.

[26] Wei Shen, Yi Gu, Hualong Xu, David Dube´, Serge Kaliaguine; Applied Catalysis A: General, 2010, 377, 1-8.

[27] Shane Moynihan, Daniela Iacopino, Deirdre O'Carroll, Hugh Doyle, David A. Tanner, and Gareth Redmond, Adv. Mater., 2007, 19, 2474-2479.

[28] D.V. Soldatov, A.T. Henegouwen, J.B. Wooten, D.E. Miser, Micropor. Mesopor. Mater., 2005, 83, 150-158.

[29] M.O. Ahmed, J. Liao, X. Chen, J. H. Kaldis, Acta Cryst. E, 2003, 59, 29-32.

[30] L. D. White, C. P. Tripp, Journal of Colloid and Interface Science, 2000, 232, 400-407.

[31] Scott, R. P. W. Silica Gel & Bonded Phases, Their Production, Properties & Use in LC; Wiley Science: New York, 1993.

[32] Shriner, R. L.; Hermann, C. K. F.; Morril, T. C.; Curtin, D. Y.; Fuson, R. C. The Systematic Identification of Organic Compounds, 7th ed.; John Wiley & Sons: New York, 1998.

[33] Christopher S. Gill, Bryant A. Price, Christopher W. Jones, Journal of Catalysis, 2007, 251, 145-152.

[34] Xin Du, Junhui He, ACS Appl. Mater. Interfaces, 2011, 3, 1269-1276.

[35] Isabellel L. Lagadic, Molly K. Mitchell, Bryan D. Payne, Environ. Sci. Technol., 2001, 35, 984-990.

[36] Dina Fattakhova Rohlfing, Jiří Rathouský, Yven Rohlfing, Oliver Bartels, and Michael Wark, Langmuir, 2005, 21, 11320-11329.

[37] H. Günzler, H.U. Gremlich, IR spectroscopy: An Introduction, Wiley-VCH, Berlin, 2002, 178-183.

[38] S. Borsacchi, M. Geppi, C.A. Veracini, F. Fallani, L. Ricci, G. Ruggeri J. Mater. Chem., 2006, 16, 4581-4591.

[39] S. Borsacchi, M. Geppi, L. Ricci, G. Ruggeri, C.A. Veracini Langmuir, 2007, 23, 3953-3960.

[40] U.P. Sudhakaran, I. Freris, M. Geppi, S. Borsacchi, D. Cristofori, P. Riello, A. Benedetti Colloids and Surfaces A: Physicochem. Eng. Aspects, 2010, 369, 191-195.

[41] Chun-Jing Liu, Shou-Gui Li, Wen-Qin Pang and Chi-Ming Che, Chem. Commun., 1997, 1, 65-66.

[42] Cotton, S. Lanthanide and Actinide Chemistry; John Wiley & Sons Ltd.: West Sussex, England, 2006.

[43] Koen Binnemans, Philip Lenaerts, Kris Driesen and Christiane Görller-Walrand, J. Mater. Chem., 2004, 14, 191-195.

[44] William Dew. Horrocks Jr., Michael Albin, Progress in Inorganic Chemistry, 1984, 31, 1-104.

[45] Reisfeld R, Jorgensen CK (1977) Lasers and excited states of rare earths. Springer-Verlag, NewYork.

[46] Liu GI, Chen X (2007) Spectroscopic properties of lanthanides in nano-materials. In: Gschneidner K Jr, Bünzli JC, Pecharsky V (eds) Handbook on the physics and chemistry of rare earths. Elsevier, Amsterdam, 99-169.

[47] S. Sivestrini, P. Riello, I. Freris, D. Cristofori, F. Enrichi, A. Benedetti, J. Nanopart. Res., 2010, 12, 993-1002.

[48] Qinghong Xu, Liansheng Li, Xinsheng Liu, and Ruren Xu, Chem. Mater., 2002, 14, 549-555.

[49] M. H. V. Werts, R. T. F. Jukes and J. W. Verhoeven, Phys. Chem. Chem. Phys., 2002, 4, 1542-1548.

[50] Peter Nockemann, Eva Beurer, Kris Driesen, Rik Van Deun, Kristof Van Hecke, Luc Van Meervelt and Koen Binnemans, Chem. Commun., 2005, 4354-4356.

Chapter 5

Studies on the effect of $Tb(dbm)_3phen$ on the luminescent properties of $Eu(dbm)_3phen$-containing mesoporous silica nanoparticles

Abstract

$Eu(dbm)_3phen$ and $Tb(dbm)_3phen$ complexes (Tris(dibenzoylmethane) mono(1,10-phenanthroline) Ln(III), where Ln(III) = Eu^{3+} and Tb^{3+}) have been impregnated in ordered mesoporous silica nanoparticles (MSNs) with an average size of 50-70 nm and a pore diameter centred at 2.8 nm, with the aim of increasing the luminescence by avoiding concentration quenching and having mainly in mind the application as down-shifter for multi-crystalline solar cells. The morphological, structural, textural and luminescent properties of the synthesized samples were characterized by N_2 adsorption-desorption, X-ray diffraction (XRD), transmission electron microscopy (TEM), UV-visible spectroscopy and photoluminescence measurements. It is demonstrated that the inclusion in the MSNs allows one to use much higher loadings (23 wt %) of the Eu-complex than in other matrices, and that co-doping with $Tb(dbm)_3phen$ improves luminescence for samples with $Eu(dbm)_3phen$ content lower than about 10 wt%.

5.1 Introduction

Lanthanide organic complexes have been widely studied for their interesting absorption and emission features and have been suggested for applications in many different fields.[1-11]

The present work was carried out having mainly the spectral converters for solar cells in mind, where the developed material needs to meet special requirements, like transparency, broad band absorption, and long-term stability. In fact, harnessing those regions of the solar spectrum which are only weakly, or not at all, converted into electricity by multicrystalline silicon solar cells is highly desirable, in order to increase efficiency and reach grid-parity. Down-shifters which convert UV radiation into visible or near infra-red light may serve this goal;[8] these materials need to efficiently absorb a broad spectral range between 300 nm and 450 nm and re-emit with a large Stokes shift in the region where the solar cells show a significantly better response. Lanthanide ions have sharp emission profiles with high internal efficiency, but their absorption is very small and it takes place only on very specific wavelengths; this may be appropriate for applications where excitation can be made by lasers, but not for solar spectrum conversion. However, if the lanthanide ion is conjugated with suitable organic ligands having an electronic structure which matches that of the lanthanide, the desired optical properties for this application may be obtained; in fact, the ligand acts as an antenna, efficiently absorbing in a broad spectral region (typically in the UV) and transferring this energy to the rare earth ion, which then emits in the visible. At the same time, in order to obtain a good quantum yield, the emitted radiation has not to be quenched by the chemical environment or the matrix in which the ions are included and/or by concentration quenching. Furthermore, the organic ligand may suffer from UV degradation or thermal instability.

In order to address such problems two synergic approaches have been tested in the presented work. The first is that of hosting the complex molecules within the pores of properly synthesized mesoporous silica nanoparticles. The pores were chosen of suitable size in order to “dilute” the emitting ions, thus avoiding concentration quenching and at the same time protecting them from the environment. Such an approach has shown to improve luminescence in similar cases.[12-15] Since the final goal is to obtain a layer transparent to visible light, the mesoporous silica must be in the form of nanoparticles to avoid light scattering; such nanoparticles can be then dispersed in the encapsulating layer of the solar cell. We show that this approach is able to host up to 26 wt%

of a lanthanide complex before concentration quenching takes place, which means some order of magnitude more than in solution.

The second approach is that of co-doping with two different lanthanide complexes, where not only the antenna but also the second lanthanide ion can act as sensitizer for the first ion. For this purpose, the Tb^{3+}/Eu^{3+} pair is well known where Tb ions can efficiently transfer energy to Eu ions increasing emission of the later ion in the red spectral region. In this situation UV light is absorbed by the ligand and then transferred to Eu ions, either directly or indirectly mediated by Tb. Optimizing the ratio between Tb^{3+} and Eu^{3+} complexes within the pores of silica nanoparticles, it is possible to avoid concentration quenching[16] and obtain high red emission intensity.

In this chapter of the thesis, the behaviour of silica mesoporous nanoparticles with different loadings of Eu-complex is investigated in detail and the effect of adding a second lanthanide complex is studied.

5.2 Experimental

5.2.1. Samples preparation

Incorporation of complexes in the mesoporous silica nanoparticles was obtained by wet impregnation technique. In a typical procedure, appropriate amount of $Ln(dbm)_3phen$ complex solution (Ln = Eu and Tb) in dichloromethane was added to 100 mg MSNs and the solution was stirred until complete evaporation of the solvent. The recovered solid was washed with dichloromethane and subsequently dried under reduced pressure (10^{-1} mbar for 4 h).

A series of samples with increasing amounts of $Eu(dbm)_3phen$ complex was prepared and labelled as Eu_x (x = 0.5, 1, 2, 5, 10, 20, 30, 40, 100), where x is the complex amount in mg per 100 mg of silica. These concentrations correspond to 0.5, 1, 2, 4.8, 9.1, 16.7, 23.1 and 28.5 wt% with respect to the overall weight of the sample, respectively. A further series of samples was prepared with different amounts of the two complexes (table 5.1). Four series were obtained by keeping constant the amount of Eu-complex at x = 0.2, 2, 5 and 10 mg, respectively and varying the Tb-complex amount by several times. Samples were then labelled as Eu_xTb_y, where x and y represent the complexes amount in mg per 100 mg of silica. The nominal wt % of each complex was calculated with respect to the overall weight of the sample and is shown in table 5.1. The

data for the four series of samples also generates a number of samples with the same Tb/Eu weight ratio. To have a finer sampling of the Tb/Eu = 5, four more samples with this weight ratio were prepared: $Eu_{0.05}Tb_{0.25}$, $Eu_{0.1}Tb_{0.5}$, $Eu_{0.5}Tb_{2.5}$, Eu_1Tb_5.

Table 5.1: Labels of the co-doped samples, Tb/Eu weight ratio, and nominal weight percentages calculated with respect to the overall weight of the sample.

Series - I			
Sample	**Tb/Eu (w/w)**	**Eu(dbm)$_3$phen (wt %)**	**Tb(dbm)$_3$phen (wt %)**
$Eu_{0.2}Tb_{0.1}$	0.5	0.20	0.10
$Eu_{0.2}Tb_{0.2}$	1	0.20	0.20
$Eu_{0.2}Tb_{0.4}$	2	0.20	0.40
$Eu_{0.2}Tb_1$	5	0.20	0.99
$Eu_{0.2}Tb_2$	10	0.20	1.96
$Eu_{0.2}Tb_4$	20	0.19	3.84
$Eu_{0.2}Tb_{10}$	50	0.18	9.07
Series - II			
Eu_2Tb_2	1	1.92	1.92
Eu_2Tb_4	2	1.89	3.77
Eu_2Tb_{10}	5	1.79	8.93
Eu_2Tb_{40}	10	1.41	28.17
Series – III			
Eu_5Tb_5	1	4.55	4.55
Eu_5Tb_{10}	2	4.35	8.70
Eu_5Tb_{25}	5	3.85	19.23
Eu_5Tb_{100}	20	2.44	48.78
Series - IV			
$Eu_{10}Tb_{10}$	1	8.33	8.33
$Eu_{10}Tb_{20}$	2	7.69	15.38
$Eu_{10}Tb_{50}$	5	6.25	31.25

5.3 Results and discussion

Molecular structures of the two complexes, viz., Eu(dbm)$_3$phen and Tb(dbm)$_3$phen, used in this work are shown in figure 5.1.

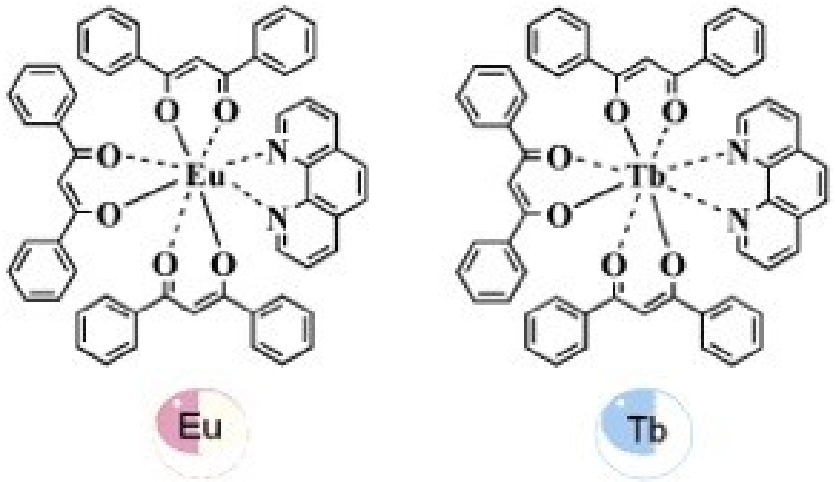

Figure 5.1: Molecular sketch of the used Ln-complex chromophores.

The absorption, excitation and emission spectra of the CH_2Cl_2 solution of $Eu(dbm)_3phen$ complex is shown in figure 5.2. Absorption takes place on two bands: one, centred at 270 nm, is attributed to the absorption by the phenanthroline ligand,[16] and is of no interest for terrestrial solar applications; on the contrary, the second band, centred in the near UV region (320-400 nm, λ_{max} = 376 nm) and attributed to the dbm ligands,[16] is of great interest since it harvests part of the AM 1.5 solar spectrum which is not harnessed by Si-based solar cells.

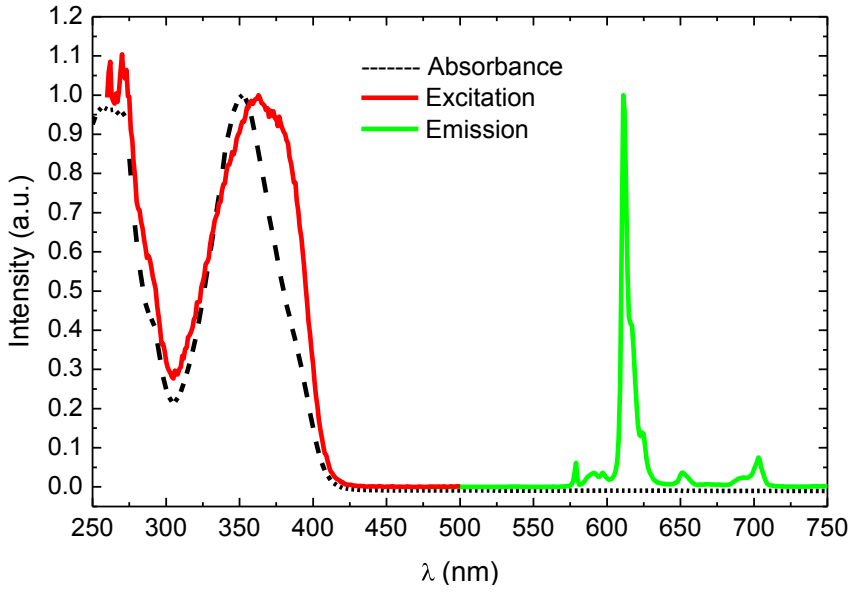

Figure 5.2: Absorption (dashed black), excitation (red) and emission (green) spectra of $Eu(dbm)_{3p}hen$ in CH_2Cl_2 solution (intensities have been suitably scaled).

The emission spectrum (figure 5.2) show the $^5D_0$-^7F_J (J = 0, 1, 2, 3, 4) transition lines of the Eu^{3+} ion, with the most prominent hypersensitive transition $^5D_0$-$^7F_2$ (618 nm) responsible for the red luminescence. The excitation spectrum recorded by monitoring emission at 618 nm overlaps fairly well with the absorption spectrum, indicating that the energy transfer from the ligands to the Eu^{3+} ions takes place efficiently. In particular, the down-conversion of the near UV light absorbed by the dbm ligands into the red emission of the Eu^{3+} would be ideal for the application to Si-based solar cells.

5.3.1. Mesoporous Silica Nanoparticles (MSN)

In order to preserve the above mentioned ideal behaviour while using the complex to produce a solid layer or film for solar applications by avoiding the problem of concentration quenching, the complex has been included into mesoporous silica nanoparticles. Figure 5.3 shows a typical TEM image of the mesoporous silica nanoparticles. The MSN are spherical in shape with an average diameter of about 50-70 nm. This size avoids scattering of the incoming light for wavelengths larger than about 200 nm, allowing a high transparency for the spectral range harnessed by photovoltaic solar cells.

The ordered channel system in the MSN can be clearly observed in the TEM micrographs by the pattern that appears when the image is slightly under-focused (see inset of figure 5.3); the pattern suggests the presence of channels opened on the surface of the particle.

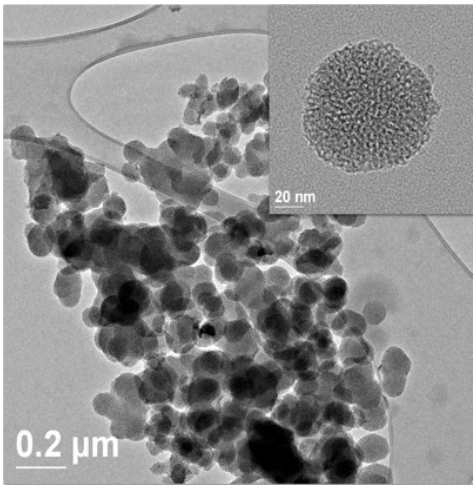

Figure 5.3: TEM image of the silica nanoparticles; in the inset, the mesoporous structure is visible for the image taken at higher magnification.

The overall specific surface area, measured by BET equation, is approximately 1000 m^2/g with a total pore volume of 1.06 cm^3/g and a narrow pore diameter distribution, centred at 2.8 nm (figure 5.4) which indicates the average size of the channel openings. The very high surface area suggests that the pore channels revealed by TEM are opened and interconnected.

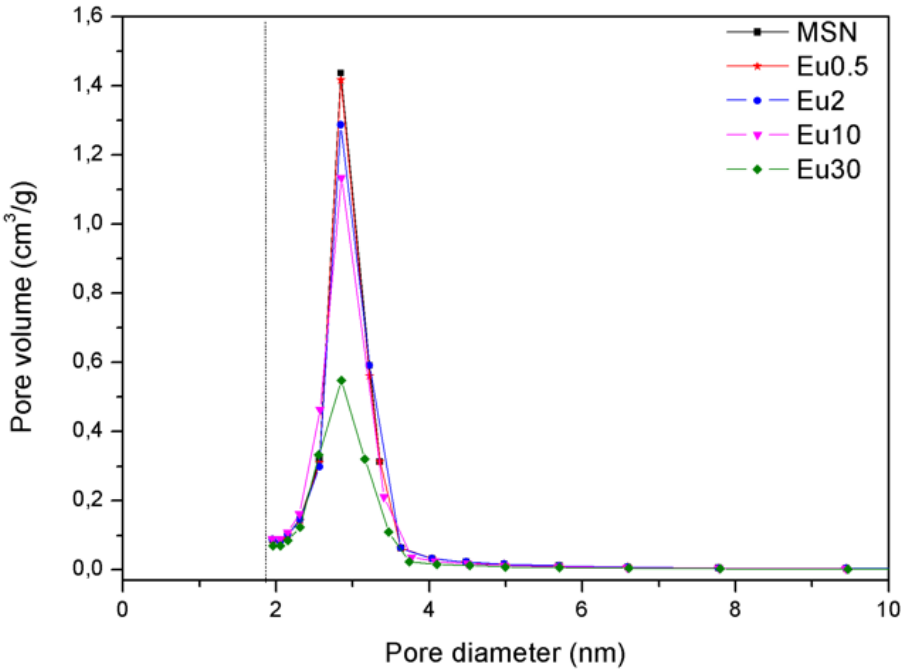

Figure 5.4: BJH pore diameter distribution of the silica nanoparticles, estimated on the adsorption branch, for different Eu loadings.

Comparing the pore diameter with the structural data of crystalline $Eu(dbm)_3phen$ complex,[17] which indicates a triclinic unit cell containing four full molecules (P-1, with α = 103.844(6)°, β = 91.466(6)°, γ = 101.585(6)°, a = 1.6275(6) nm, b = 2.3504(9) nm and c =3.171(1) nm, volume = 11,504 nm^3), it can be argued that the pore openings are sufficiently large to allow the complex molecules to enter into the channels and host at least one complex molecule (approximating the complex by a sphere, its diameter would be 1.76 nm; even if the unit cell suggests a slightly elongated shape, the molecule clearly remains smaller than the pore size, not mentioning that the molecule could oriented parallel to the channel direction and enter pores even smaller than its larger size).

By considering the density value (1.446 gcm^{-3}) for a crystalline arrangement reported in the same paper[17] and the measured total pore volume, the maximum theoretical amount of complex which could be hosted within the MSNs has been estimated to be 140 wt % of the silica matrix. This is of course an overestimated value, because the impregnation procedure will not allow accommodating the complex molecules in a compact manner as in the crystalline state, completely filling the whole pore volume. However, it is a useful theoretical upper limit for the complex loading.

5.3.2. Eu-doped MSN

The silica samples impregnated with the Eu-complex were measured by XRPD and no crystalline peaks were detected. This may be taken as an indication of the dispersion of the complex on a molecular level, even if the formation of an amorphous phase or crystals too small to be detected cannot be excluded using these data. However, BET analysis (figure 5.4) shows that the pore volume decreases when the complex is added, suggesting that the complex molecules are indeed entering into the pores of MSN.

TEM images of the Eu impregnated material do not show the presence of Eu-complex agglomerates outside of the silica particles until 23 wt% is reached. At this loading (sample Eu_{30}) amorphous agglomerates start to show up (figure 5.5) and become more frequent for higher loadings. The EDS analysis confirms that such agglomerates are indeed of Eu-complex and, at the same time, it detects the presence of europium in the MSNs, confirming that the Eu-complex has entered the pores of the impregnated MSNs.

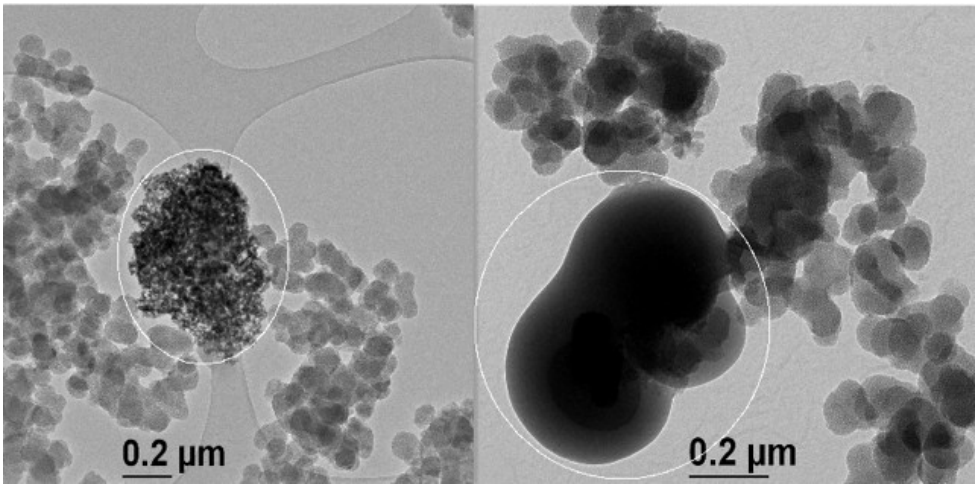

Figure 5.5: TEM images of samples Eu_{30} (left) and Eu_{40} (right) in areas where Eu-complex agglomerates outside of the nanoparticles are visible (see marked areas).

The shape of the emission spectrum does not change significantly from that of pure $Eu(dbm)_3phen$ when the Eu-complex is included in the MSN. However, the intensity of the hypersensitive $^5D_0$-$^7F_2$ peak shows a linear increase with increasing loading up to about 25 wt %, where it starts to bend towards an asymptotic behaviour (figure 5.6). The limit value of the linear range corresponds to about 20 wt % of the estimated maximum theoretical loading. This means that a substantial volume of the pores channels remains unexploited; we can imagine that at his loading all pore openings are filled with one molecule, hindering the entering of further molecules. This value also coincides with the loading from which external agglomerates have been observed by TEM, suggesting that concentration quenching starts to take place when the complex molecules are not confined within the pores.

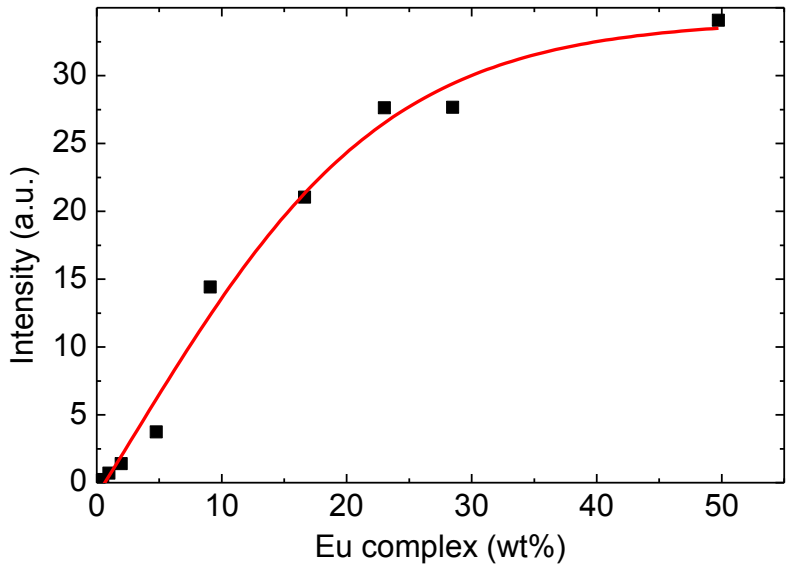

Figure 5.6: Plot of the $^5D_0$-$^7F_2$ peak intensity *vs* Eu-complex content in wt% (λ_{ex} = 618 nm).

Looking at the excitation spectra (figure 5.7), it is possible to observe that for the small amounts of Eu-complex, the band in the near UV range is significantly different from the one of the complex in solution and it greatly differs from the absorption band. On the contrary, this does not change its shape. In the case of very efficient sensitization (e.g. energy transfer from the sensitizer to the Ln^{3+} ion) such an excitation spectrum would be roughly equivalent to the sample

absorption spectrum (that is to the absorption spectrum of the sensitizer).[10] However, several non-radiative processes, like energy back transfer to the sensitizer, energy transfer quenching (important for Eu^{3+}), and matrix vibrations can decrease the efficiency of sensitization,[18] leading to a mismatch between absorption and excitation spectra. A relevant amount of light being absorbed by the sensitizer without being transferred to the Ln^{3+} ion, the overall luminescence quantum yield of the system decreases. Figure 5.7 shows that this is happening for low loadings, where the near UV band becomes asymmetric and its maximum moves from 350 to about 400 nm, in a spectral region where absorption is low, i.e. most of the energy absorbed by the chromophore seems to be wasted for down-conversion applications. For larger amounts of Eu-complex, the left side of the band is growing, progressively filling the region where absorption takes place. It looks like there was a threshold above which the electronic structure of the ligands relaxes towards a configuration where non-radiative processes are deactivated and energy transfer to the lanthanide ion is favored.

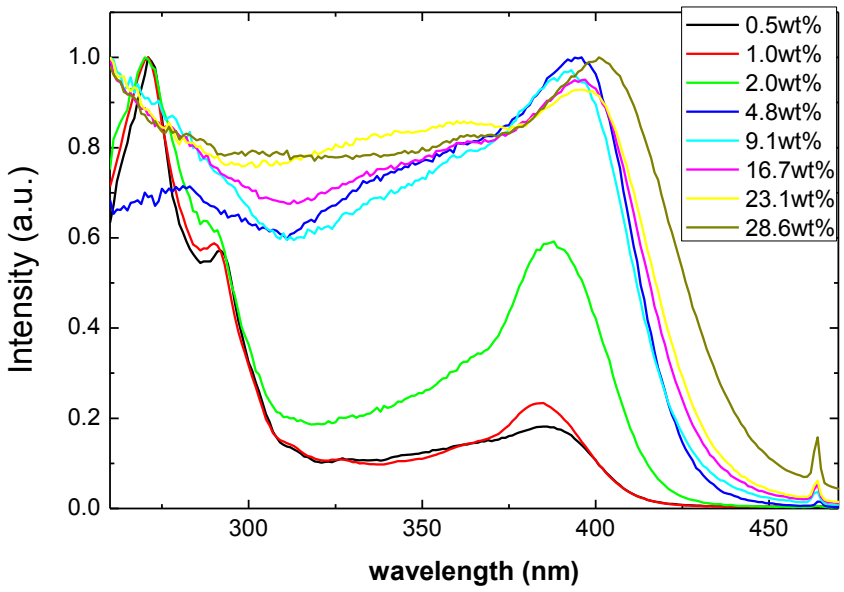

Figure 5.7: Excitation spectra of samples with different amounts of Eu-complex.

5.3.3. Co-doped MSN

As stated above, co-doping is a further possible mean to keep Eu^{3+} ions enough apart to avoid concentration quenching, in addition to possibly giving a further increase in the sensitizing effect

to the Eu^{3+} ions. With this aim, a Tb-complex with the same ligands has been used. It absorbs in the same spectral region, but due to energy levels proximity between triplet states of the ligands and $^5D_4$ level of the Tb ion (figure 5.8), negligible luminescence is observed. The terbium complex should work as solar "accumulator" for the Eu complex: the solar energy is absorbed by the complex and transferred via Förster Resonance Energy Transfer (FRET) to the Eu-complex (figure 5.8) augmenting the number of photons converted into visible region; at the same time this allows one to use a lower amount of Eu ions, decreasing the possibility of concentration quenching.

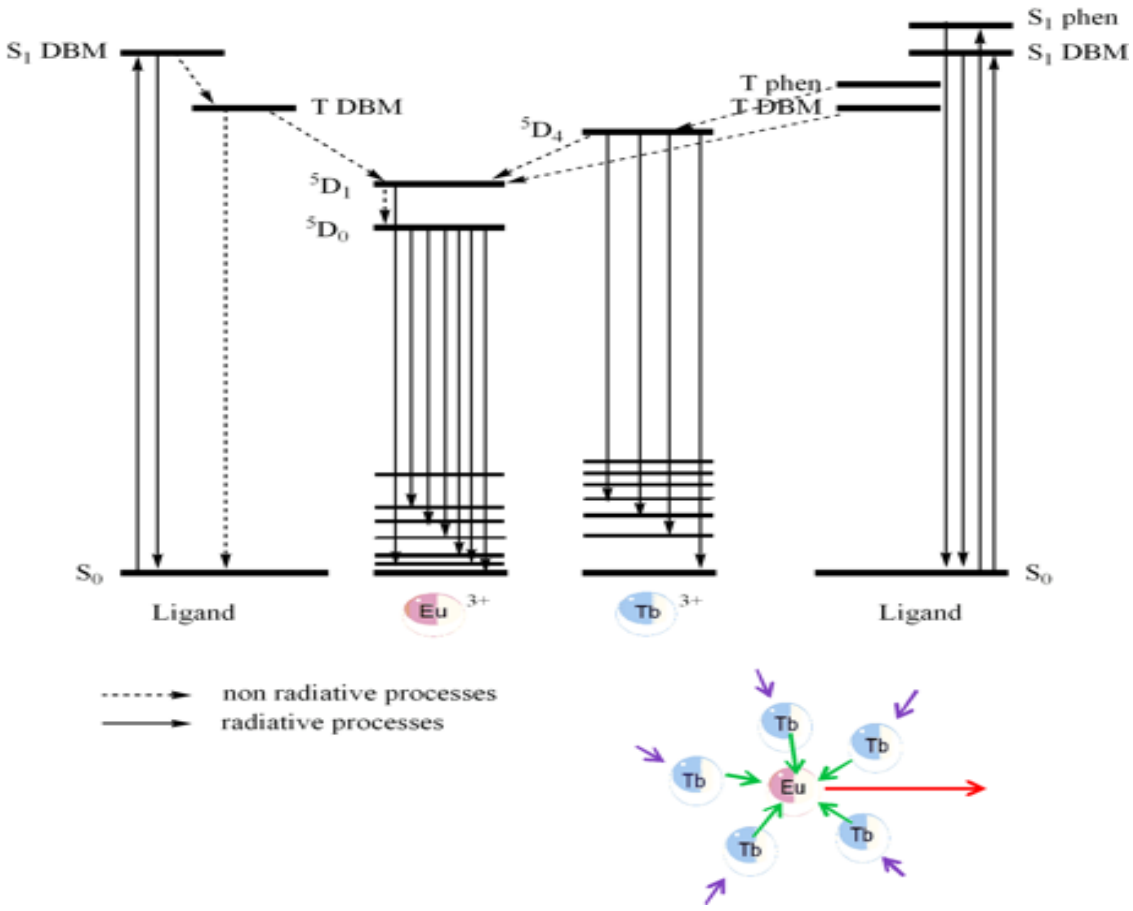

Figure 5.8: Schematic representation of photophysical processes of $Eu(dbm)_3phen$ and $Tb(dbm)_3phen$ co-doped in mesoporous silica nanoparticles.

Considering that FRET depends upon the donor to acceptor distance with an inverse 6th power,[19] the impregnation of both Eu and Tb complexes into the pores of mesoporous silica nanoparticles should keep both Tb and Eu complexes sufficiently close to one another, at the same time

maintaining the Eu^{3+} ions distance sufficiently large. Luo *et al.* has used a simple quenching "sphere of action" model for understanding the role of concentration in the case of a dispersion of the $Eu(dbm)_3phen$ and $Tb(dbm)_3phen$ complexes in Poly(methyl methacrylate) polymer.[16] Following this model, the Tb complex needs to be within a sphere of radius R centred in a Eu-complex, in order to act as a sensitizer. For larger distances the dipole-dipole interaction would be too weak to allow energy transfer. They determined a radius of 1.63 (±0.01) nm. In the frame of this model, the ratio between the numbers of Tb-complexes to Eu-complex molecule assumes a key role, and the best sensitization will be when each Eu-complex will be surrounded by the maximum number of Tb-complex molecules within the sphere of action, which, taking into account the size of the complexes will be about six. Also, there will be a minimum loading for sensitization since at least one Tb-complex needs to be within the sphere of action. Thus, for sensitization there will be minimum concentration which guarantees at least one molecule within the action sphere, an ideal concentration which is sufficient to position about six Tb-molecules around each Eu-complex molecule, and where the Eu/Tb ratio will have a value around six. In fact, Luo *et al.* reported that the intensity of emission of the Eu/Tb doped PMMA samples first show a decrease (due to some absorption of not sensitizing Tb-complexes) and then increases up to a certain loading, thereupon remaining constant.[16] However, no analysis was made to find the ideal concentration by systematically varying both Eu and Tb complex concentrations.

In the present work, a similar situation can be demonstrated by analyzing the excitation spectra at different concentrations. In figure 9, the excitation spectra for the four different series are shown (normalized by their maximum). At low Eu-complex loading ($Eu_{0.2}Tb_x$) the intensity in the central region, where absorption is at maximum, increases, but even for a Tb/Eu ratio of 20 there is still a minimum in that region. Apparently, the Eu complex molecules are too diluted in this case that a large amount of Tb complex is needed to have at least one sensitizer molecule close to a sufficient number of sensitized molecules. In this case, however, a large number of Tb complex molecules will absorb without sensitizing. For Eu_2Tb_x the highest intensity in the central region is reached for the Tb/Eu = 5, close to the ideal ratio. The latter also suggests that the total amount of complex is close to the ideal value. The trend of the Eu_5Tb_x series is a bit less clear: the highest intensity is obtained for a Tb/Eu ratio of 1, but the "flattest" one is at Tb/Eu = 5. For the

highest loadings, changes are not so significant, the non-doped sample having already quite a good match with the absorption profile, but at Tb/Eu = 5 the curve is somewhat flatter.

Comparing the excitation spectra of samples with the same ratio Tb/Eu = 5 (figure 5.10), close to the ideal ratio, we can see that sensitization is not effective for low total amount of complexes, while the best results are obtained for samples Eu_1Tb_5 and Eu_2Tb_{10}, confirming that the ideal concentration is reached for a total concentration of the order of 10 wt%, as already suggested by figure 5.9.

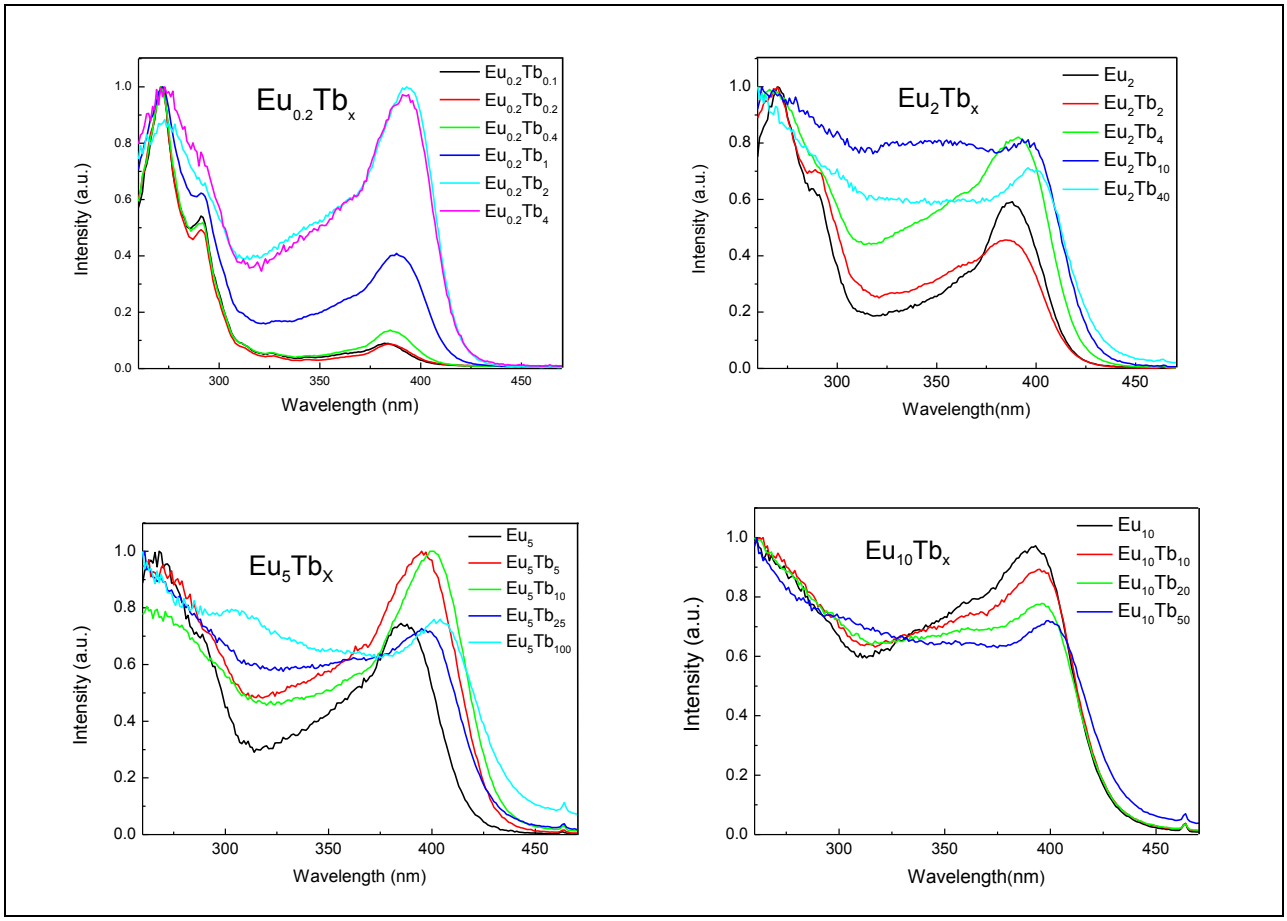

Figure 5.9: Excitation spectra of samples with different amount of Tb-complex for different constant amounts of Eu-complex (each normalized to its maximum intensity).

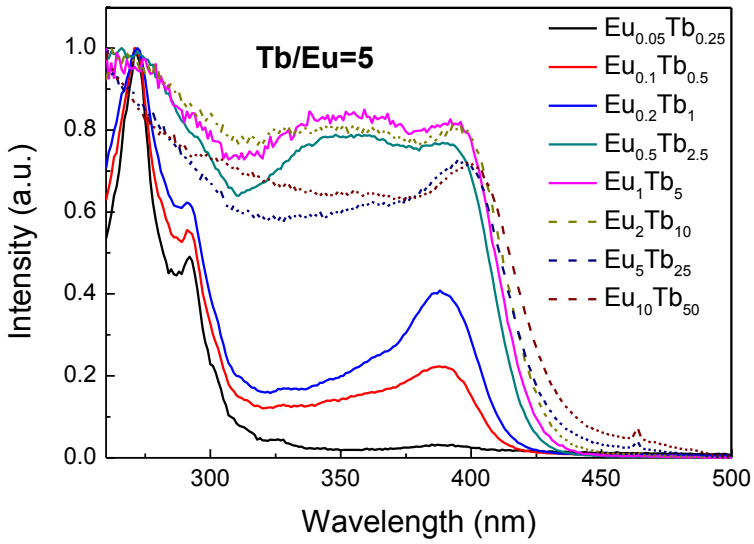

Figure 5.10: Excitation spectra of samples with the same Tb/Eu ratio (each normalized to its maximum intensity).

The results of the emission measurements reflect the considerations made above on the excitation spectra. For all of the co-doped samples the emission profile, as well as the lifetime measurements at 618 nm, does not show any significant difference from the singly-doped samples. At the same time, the emission intensity tends to increase by increasing the loading. However, a plot of the emission intensity at constant Eu amount with increasing Tb loading (figure 5.11) shows an increase only when the total amount of complex is lower than about 10 wt.%. For the samples containing 10 wt% of Eu, the addition of the Tb-complex does not seem to have any effect. This is because for the $Eu_{10}Tb_{10}$ sample the quantity of the Tb is probably below the limit to give at least one Tb-complex in the action sphere and for higher Tb-complex loadings the total amount exceeds the quantity that be contained in the pores, as seen in the singly-doped samples.

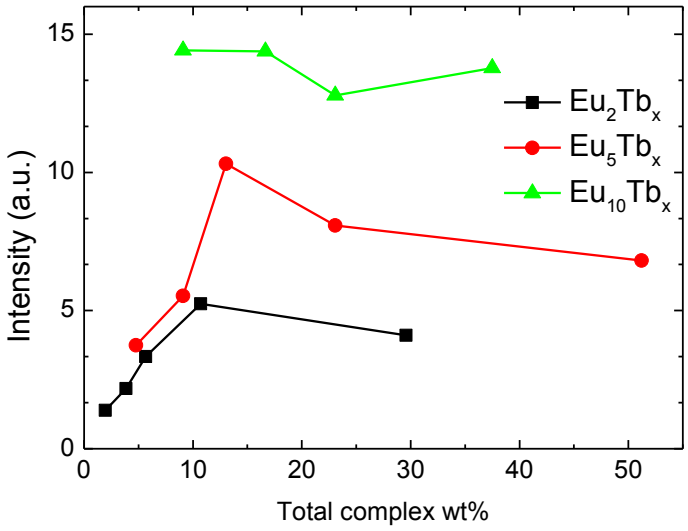

Figure 5.11: Emission intensity of the $^5D_0$-$^7F_2$ peak for different constant amounts of Eu-complex and increasing Tb-complex loadings.

The behaviour of the material can be explained by the sphere of action model in terms of ideal concentrations and Tb/Eu ratios and considering the constraint introduced by the pores. In fact, the model used by Luo must be adapted to the present situation, since the pores introduce a limit to the possible number of neighbouring molecules. Actually, the pores have an average size smaller than the diameter of the sphere of action, so that, for most of the pores the ideal ratio of 6 could possibly not be reached due to space limitations. The experimental data do not seem to confirm this, since the better sensitization seems to take place close to the ideal ratio, which probably means that the complex molecules are able to use their elongated size to find a geometrically optimized configuration, or that the size of the molecule has been slightly over-estimated. It would be, however, interesting to experiment with MSN with slightly larger pores, in order to see if the idealness of the system could be improved.

5.4. Conclusions

The inclusion of $Eu(dbm)_3phen$ inside mesoporous silica nanoparticles, either alone or together with $Tb(dbm)_3phen$, have a positive effect on luminescence, since the emission increases linearly up to much higher Eu-loadings (23 wt.%) than in other matrices before showing concentration quenching. Co-doping with Tb enhances the emission of the material, but reaches a limit for a

total amount of the complex of about 10 wt%. The results could be interpreted by using a simple sphere of action model adapted to the case of a pore-limited system.

5.5. References

[1] V. Divya, R.O. Freire, M.L.P. Reddy, Dalton Trans., 2011, 40 3257-3268.

[2] S. V. Eliseeva, J.-C. G. Bünzli, Chem. Rev., 2010, 39, 189-227.

[3] M.D. McGehee, T. Bergstedt, C. Zhang, A.P. Saab, M.B. O'Regan, G.C. Bazan, V.I. Srdanov, A.J. Heege, Adv. Mater., 1991, 11, 1349-1354.

[4] N.T. Kalyani, S.J. Dhoble, Renew. Sust. Energ. Rev., 2012, 16, 2696-2723.

[5] C.J. Piguet, C.G. Bünzli, G. Bernardinelli, G. Hopfgartner, A.F. Williams, J. Am. Chem. Soc., 1993, 115, 8197-8206.

[6] X. Huang, S. Han, W. Huang, X. Liu, Chem. Soc. Rev., 2013, 42, 173-201.

[7] B.M. van der Ende, L. Aarts, A, Meijerink, Phys. Chem. Chem. Phys., 2009, 11, 11081-11095.

[8] E. Klampaftis, D. Ross, K.R. McIntosh, B.S. Richards, Sol. Energy Mat. Sol. C., 2009, 93, 1182-1194.

[9] C. Strümpel, M. McCann, G. Beaucarne, V. Arkhipov, A. Slaoui, V. Svrcek, C. del Cañizo, I. Tobias, Sol. Energ. Mat. Sol. C., 2007, 91, 238-249.

[10] A. Le Donne, M. Acciarri, D. Narducci, S. Marchionna, S. Binetti, Prog. Photovolt: Res. Appl., 2009, 17, 519-525.

[11] A. Le Donne, M. Dilda, M. Crippa, M. Acciarri, S. Binetti, Opt. Mater., 2011, 33, 1012-1014.

[12] X. Qinghong, L. Liansheng, L. Bin, Y. Jihong, X. Ruren, Micropor. Mesopor. Mater., 2000, 38, 351-358.

[13] Q. Xu, L. Li, X. Liu and R. Xu, Chem. Mater., 2002, 14, 549-555.

[14] Y. Li, B. Yan, Y. Li , J. Solid State Chem., 2010, 183, 871-877.

[15] D. Zhang, D. Tang, X. Wang, Z. Qiao, Y. Li. Y. Liu, Q. Huo, Dalton Trans., 2011, 40, 9313-9319.

[16] Y. Luo, Q. Yan, S. Wu, W. Wu, Wenxuan and Q. Zhang, J. Photochem. Photobiol. A-Chem., 2007, 191, 91-96.

[17] M.O. Ahmed, J.L. Liao, X. Chen, S.A. Chen, J.H. Kaldis, Acta Cryst. E59 (2003) m29-m32.

[18] K. Binnemans, Chem. Rev., 2009, 109, 4283-4374.

[19] T. Förster, Ann. Phys., 1948, 2, 55-75

Chapter 6

Phosphonium ion based tetrakis dibenzoylmethane Eu(III) and Sm(III) complexes: Synthesis and luminescence properties in weakly coordinating ionic liquid

Abstract

Highly luminescent anionic Ln(III)-β-diketonate complexes (Ln = Eu and Sm) has been synthesized and dissolved in phosphonium ionic liquid, trioctylmethylphosphionium bis(trifluoromethylsulfonyl)imide, [TOMP][Tf_2N]. The common countercation of the ionic liquid and those of Eu(III) and Sm(III) complexes ensured good solubility of these complexes in ionic liquid. The Ln(III)-β-diketonate complexes that were studied are [TOMP][$Ln(dbm)_4$], where Ln: Eu^{3+} and Sm^{3+}, and dbm is 1,3-diphenylpropane-1,3-dione. Single crystal X-ray structure determination performed on the europium complex show that the europium ion is surrounded by four ligands and no water/solvent molecules are coordinated to the Eu^{3+}. These solid complexes showed good thermal stability up to 250°C. The photoluminescence of Eu(III) and Sm(III) complexes were studied in solid state, in the solution of these complexes in ionic liquid as well as in acetonitrile solvent (MeCN). This study demonstrates that the phosphonium ionic liquids such as [TOMP][Tf_2N] can be used as spectroscopic solvent for the luminescence of lanthanide(III)-β-diketonate complexes.

6.1. Introduction

The past three decades have witnessed continuing interest in the field of lanthanide based materials research. Lanthanide (III) β-diketonate complexes have been widely studied either as tris (LnL_3 type) or tetrakis (β-diketonate) complexes $[C]^+[Ln(L)_4]^-$ type. Because of the lower coordination number of tris complexes (generally six), they usually contain water or other solvent molecules in the first coordination sphere, which is detrimental for obtaining high luminescence intensities. In the later case, all the coordination positions are filled up by four β-diketonate ligand donor atoms (L) and the charge neutrality is provided by an organic cation (C). An additional ligand in the tetrakis complexes provide better shielding of the Ln^{3+} ion which can lead to significant enhancement of the luminescence properties of the complex by avoiding the coordination of small but strongly quenching solvent molecules. Tetrakis complexes usually show much higher luminescence intensities than the corresponding hydrated tris complexes.[8] There are few reports on the lanthanides complexes of the $[C]^+[Ln(L)_4]^-$ type as compared to the tris complexes of the LnL_3 type.

Some recent studies have successfully demonstrated the use of room-temperature ionic liquids (RTILs) in photochemistry and spectroscopy.[2-9] Lanthanide metal containing ionic liquids are being viewed as new type of promising soft material which can combine the advantageous properties of the ionic liquids with additional intrinsic magnetic, optical and catalytic properties of the incorporated metal complex anion.[10] Therefore, it is attractive and desirable to develop ionic liquids containing high concentrations of lanthanides. Most of the studies on the lanthanide compounds in ionic liquids have been performed with ionic liquids based on imidazolium cations and on the emission of Eu^{3+} due to high-luminescence intensity combined with relatively easy-to-interpret emission spectra of the Eu^{3+} ion.[2,5,6,11-13] Sm^{3+} is an interesting nevertheless less well studied lanthanide emitter that in addition to visible luminescence also show the large contribution of its luminescence in the near-infrared region (NIR). Due to the poor absorbing abilities (typically less than 3 L mol^{-1} cm^{-1}) and smaller energy gap between the emitting level and the next lower energy level (7500 cm^{-1}) of Sm^{3+}, they show weaker luminescence intensity. This can be overcome by using efficient sensitizing ligands such as B-diketonates. However, these ligands exhibit lower photostability for the corresponding complexes in conventional organic solvents. A high quantum yield and an enhanced photostability have been reported for a

Eu(III) tetrakis complex after dissolving in a weakly coordinating imidazolium ionic liquid.[2] The improvement of the photophysical properties of tetrakis complex in ionic liquid [HMIM][Tf_2N] were assumed to be due to the hydrogen bonding between the cation and ligands. Phosphonium ionic liquids (PILs) have been available in large scale for about two decades and their use has gained great interest as reaction media.[14,15] They were found to have wider electrochemical window than the imidazolium salts. Unlike imidazolium ionic liquids, PILs will not be reduced by the electropositive f-elements and therefore these are suitable for study of the electrochemical properties and electrodeposition of f-elements. Moreover, PILs are found to be thermally more stable than IILs.[16] When the lanthanide complexes are dissolved in the imidazolium ILs, the acidic hydrogen atoms on the imidazolium rings form hydrogen bonds to the oxygen's of the diketonate anion. However phosphonium ILs used in the present study does not form such hydrogen bonds with the dibenzoylmethane anion. Therefore, it is interesting to study spectroscopy of lanthanide compounds in phosphonium ionic liquids.

Our aim was to prepare ionic lanthanide complexes with phosphonium cation wherein a good shielding of the lanthanide ion can be accomplished by an efficient light harvesting antenna such as 1,3-diphenylpropane-1,3-dione and that show good solubility in phosphonium ionic liquid [TOMP][Tf_2N] (TOMP = trioctylmethylphosphionium, Tf_2N = bis(trifluoromethanesulfonyl)imide). Ionic liquid [TOMP][Tf_2N] used in this study have been purposefully designed to gain the weakly coordinating solvent characteristics suitable for the study of lanthanide β-diketonate complexes.

In the present work, we report synthesis of trioctylmethylphosphionium tetrakis (dibenzoylmethane) europate (III) [TOMP][$Eu(dbm)_4$] **(I)** and Trioctylmethylphosphionium tetrakis (dibenzoylmethane) samarate (III) [TOMP][$Sm(dbm)_4$] **(II)** complexes and their photoluminescence properties in the phosphonium ionic liquid. The introduction of trioctylmethylphosphionium countercation [TOMP] in the Eu(III) and Sm(III) complexes ensured their solubility in the ionic liquid [TOMP][Tf_2N]. The photophysical properties of solutions of tetrakis europium and samarium complexes in [TOMP][Tf_2N] were investigated systematically. The visible luminescence of **(I)** and **(II)** in solid state and in [TOMP][Tf_2N] has been studied along with the near infrared emission (NIR) of **(II)**. [TOMP][Tf_2N] IL was used in this study, since the [Tf_2N] anions are known to coordinate very weakly to the lanthanide ions.

6.2. Results and discussion

Complex **(I)** was prepared by dissolving 4 equiv. of the ionic liquid [TOMP][dbm] in ethanol, followed by the dropwise addition of 1 equiv. of the $Eu{\cdot}Cl_3{\cdot}6H_2O$ in water. The solution was left to stir at room temperature for 2 h; precipitated complex was filtered and dried under high vacuum (10^{-1} mbar/1 h). It was then crystallized from ethanol (scheme 6.1).

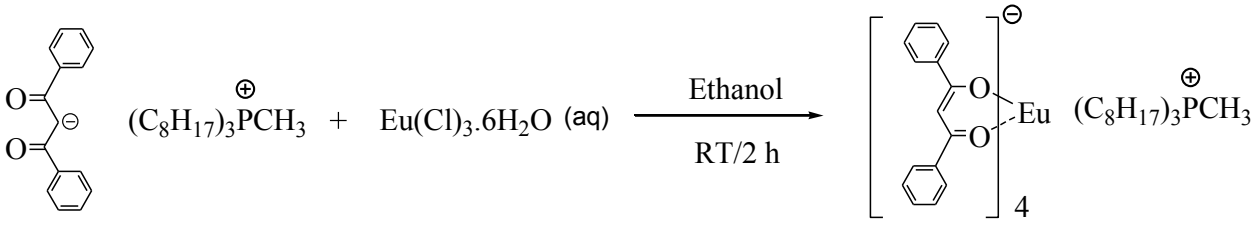

I

Scheme 6.1: Synthesis of complex **(I)**

Complex **(II)** was prepared by dissolving 4 equiv. of the ionic liquid [TOMP][dbm] in ethanol, followed by the dropwise addition of 1 equiv. of the $Sm{\cdot}(NO_3)_3{\cdot}6H_2O$ in water. The solution was left to stir at room temperature for 2 h, precipitated complex was filtered, washed with ice-cold water and the sticky solid was first dried under reduced pressure (10^{-1} mbar/4h) and crystallized from ethanol (scheme 6.2).

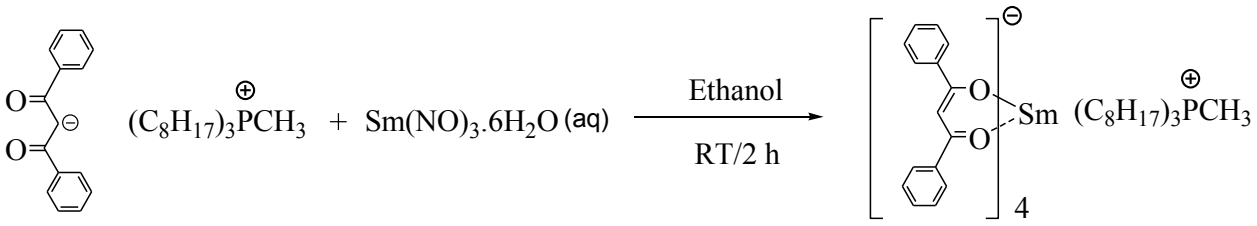

II

Scheme 6.2: Synthesis of complex **(II)**

6.2.1. Crystal structures of (I) and (II):

Crystal structures obtained for $TOMP[Eu(dbm)_4]$ and $TOMP[Sm(dbm)_4]$ complexes show monoclinic cells, containing two crystallographically independent molecules for Europium complex (figure 6.1) and one for Samarium one (figure 6.2). No crystallization solvent molecules have been found trapped in the crystal packing. Essential structural data are reported in table 6.1.

Table 6.1: Essential crystallographic data for TOMP[Eu(dbm)$_4$] and TOMP[Sm(dbm)$_4$].

	TOMP [Eu(dbm)$_4$]	**TOMP[Sm(dbm)$_4$]**
Empirical formula	2 · (C_{85} H_{98} O_8 P Eu)	C_{85} H_{98} O_8 P Sm
Formula weight	2861.12	1428.95
Temperature	100(2) K	100(2) K
Wavelength	0.6525 Å	0.6525 Å
Crystal system	Monoclinic	Monoclinic
Space group	P 2_1/a	P 2_1/c
Unit cell dimensions	a = 20.852(3) Å, b = 22.412(3) Å, c = 32.475(2) Å, α = γ = 90°, β= 102.214(13)°	a = 16.169 (4) Å, b = 22.341(5) Å, c = 20.962 (5) Å, α = γ = 90°, β= 100.60 (15)°
Volume	14833(3) Å^3	7443.0(8) Å^3
Z	4	4
Density (calculated)	1.281 Kg/dm^3	1.275 Kg/dm^3
Absorption coefficient	0.679 mm^{-1}	0.638 mm^{-1}
F(000)	6000	2996
Theta range for data collection	0.589 to 22.574°.	1.444 to 21.253°.
Reflections collected	314047	48880
Independent reflections	24306 [R(int) = 3.2 %]	10455 [R(int) = 15.5%]
Refinement method	Full-matrix least-squares on F^2	Full-matrix least-squares on F^2
Data / restraints / parameters	24306 / 1462 / 1527	10455 / 213 / 764
Goodness-of-fit on F^2	1.046	1.025
Final R indices [I>2sigma(I)]	R1 = 0.0954, wR2 = 0.2261	R1 = 0.0785, wR2 = 0.2049
R indices (all data)	R1 = 0.0984, wR2 = 0.2284	R1 = 0.1038, wR2 = 0.2332

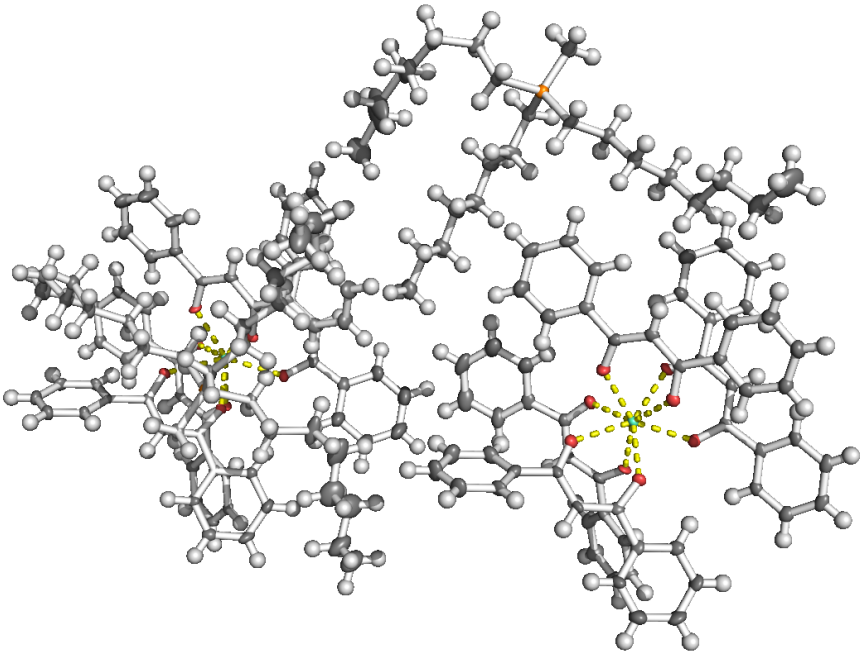

Figure 6.1: TOMP[Eu(dbm)$_4$] crystallographically independent unit (50% thermal ellipsoid probability)

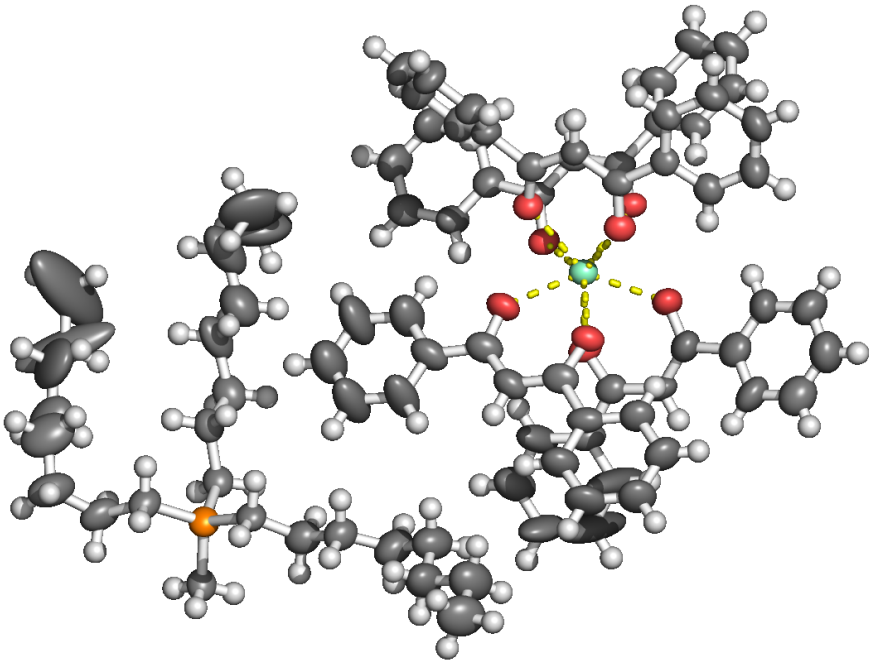

Figure 6.2: TOMP[Sm(dbm)$_4$] crystallographically independent unit (50% thermal ellipsoid probability)

The unit cells for the two compounds differ in their volume, maintaining a very similar crystal packing: the small Samarium cell (figure 6.3) can transformed in the Europium one (figure 6.4), swapping *c* and *a* axis and doubling the length of the shorter cell edge.

The larger cell shows a volume which is double of Samarium one, due to a different conformation of the TOMP cation for each crystallographically independent molecule. The long alkylic chains of TOMP cation in fact are quite flexible and can assume different conformations in the cavities among neighbor's dibenzoylmethane complexes, leading to disorder in the crystal packing (not shown in figures).

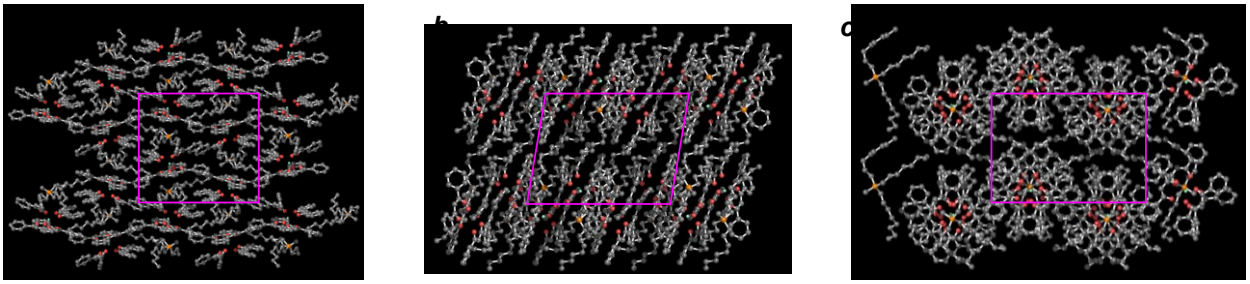

Figure 6.3: TOMP[Sm(dbm)$_4$] crystal packing (50% thermal ellipsoid probability – hydrogen atoms omitted for clarity); views along *a*, *b* and c axis.

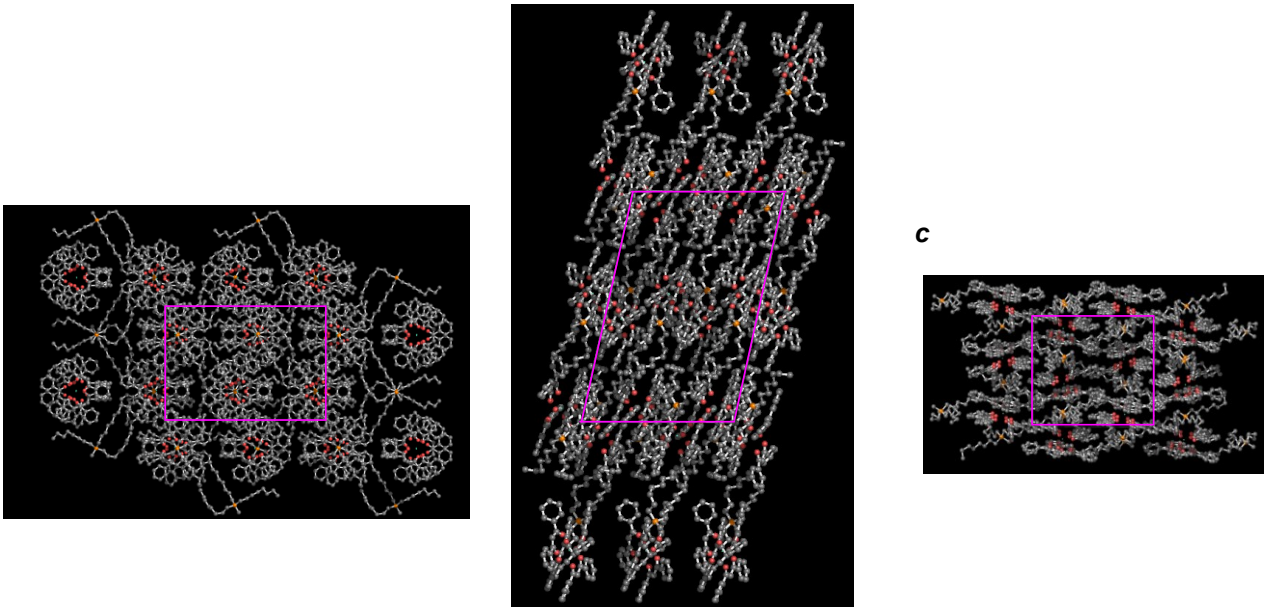

Figure 6.4: TOMP[Eu(dbm)$_4$] crystal packing (50% thermal ellipsoid probability – hydrogen atoms omitted for clarity); views along *a*, *b* and *c* axis.

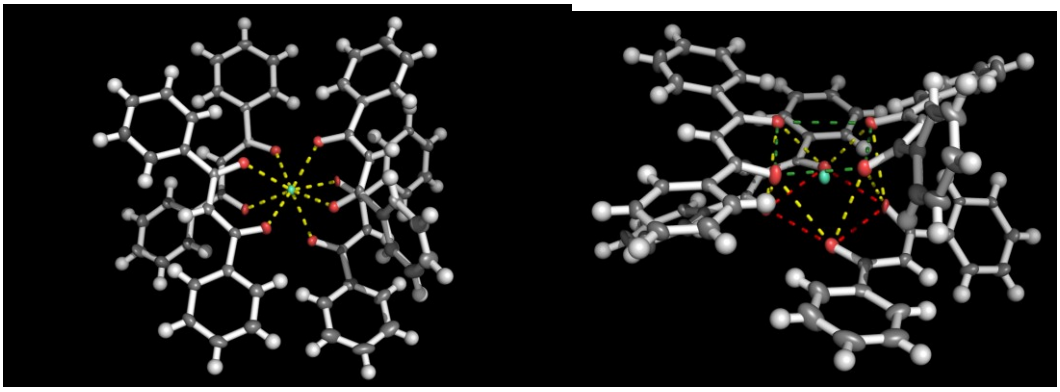

Figure 6.5: TOMP[Ln(dbm)$_4$] (a) show the eight-coordinate metal center. (b) Show the distorted square antiprism coordination geometry (50% thermal ellipsoid probability).

Both the complexes show a mean bond length of 2.40(4) Å around the metal atom and mean bond angles of 75(5)°; each dibenzoylmethane chelate molecule shows alternate long-short Ln-O bond distances (with bond length differences varying from 0.01 to 0.1 Å; figure 6.5a).

The overall coordination geometry (figure 6.5b) resembles a distorted square antiprism as previously reported in literature for similar tetrakis complexes.[17]

6.2.2. Thermal analysis

6.2.2.1.Thermal analysis of (I)

Thermal analysis of the complexes (I) and (II) were carried out under (N_2/air) atmosphere in the temperature range from 40 to 900 °C, at a heating rate 10 °C /min. The TG/DTG curves for the Eu complex are shown in figure 6.6. It shows excellent thermal stability up to 250 °C. The weight loss can be divided into two stages. The first weight loss in the temperature range of 250 – 425 °C gave weight loss of (47 %). The second weight loss in the temperature range of 425 – 600 °C. From the derivative weight loss curve it is apparent that the maximum weight loss occurs at 325 °C. It may be caused by the oxidation of ligands in the complex. No weight loss was observed in the region (30 – 115 °C) due to the absence of any moisture or coordinated water molecules in the complex.

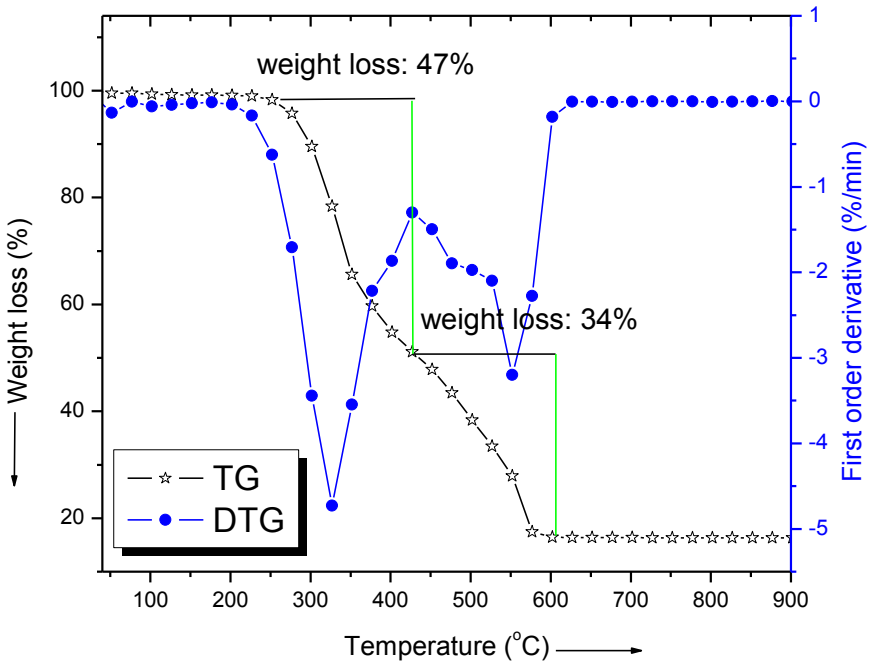

Figure 6.6: TG–DTG curve of the complex **[I]**.

6.2.2.2 Thermal analysis of (II)

The TG analysis of the Sm complex was carried out under (N_2/air) atmosphere in the temperature range of 40 to 900 ^oC at a heating rate 10 ^oC/min. The TG/DTG curves for the Sm complex are shown in figure 6.7. High thermal stability is an essential requirement for most applications. The complex shows an excellent thermal stability up to 285 ^oC, which is high enough for most luminescence applications. The weight loss can be divided into two stages similar to the europium complex discussed above. The first weight loss in the temperature range of 285 – 410 ^oC gave weight loss of (49.6%). The second weight loss in the temperature range of 410 – 610 ^oC. From the derivative weight loss curve it is apparent that the maximum/highest weight loss occurs at 385.3 ^oC. It may be caused by the oxidation of dibenzoylmethane ligands in the complex. No weight loss was observed in the region (30 – 115 ^oC) due to the absence of any moisture or coordinated water molecules in the complex.

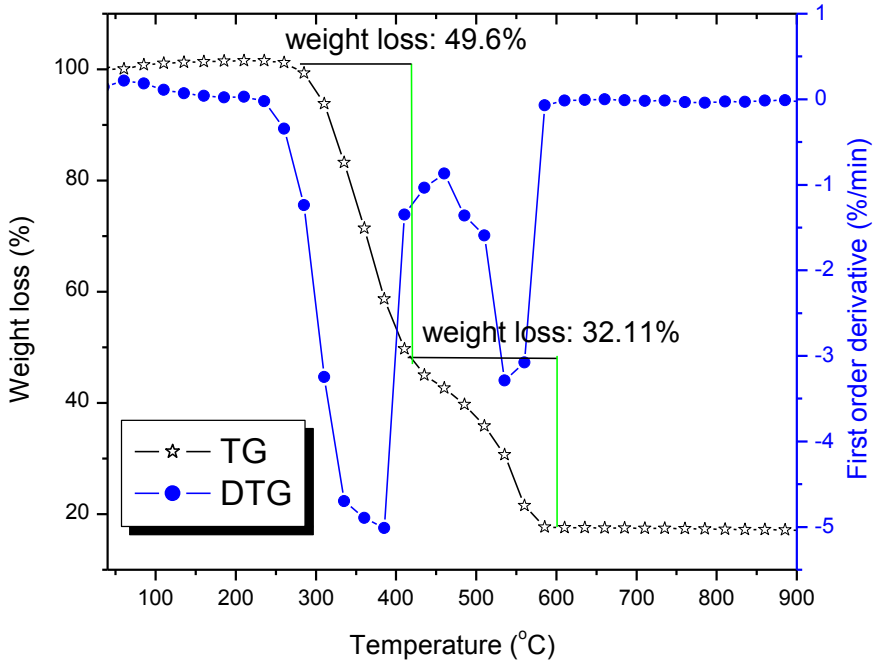

Figure 6.7: TG–DTG curve of the complex **[II]**.

6.2.3. Photoluminescence properties

6.2.3.1 Photoluminescence properties of Eu complex (I)

The room temperature photoluminescence excitation spectrum of complex **[I]** in solid state is shown in figure 6.8. The excitation spectrum was obtained by monitoring the $^5D_0 - {}^7F_2$ transition of Eu^{3+} at 611 nm. It shows broad band in the range of 280 – 450 nm with maximum absorption around 415 nm due to the efficient p → p* transition of the DBM ligands.[18-20] The narrow band at 464 nm is assigned to $^7F_0 - {}^5D_2$ transition. The emission spectrum of the complex **(I)** is shown in figure 6.9. It was recorded by setting excitation wavelength at 415 nm. The excitation energy is absorbed by the ligands and transferred to the Eu^{3+} emitting center in a subsequent step (antenna effect). The emission spectrum consists of several transitions $^5D_0 - {}^7F_J$ (J = 0, 1, 2, 3, 4) related to the radiative de-excitation from the $^5D_0$ emitting level of Eu^{3+} [579 ($^5D_0 - {}^7F_0$), 591 ($^5D_0 - {}^7F_1$), 611, 613 ($^5D_0 - {}^7F_2$), 651 ($^5D_0 - {}^7F_3$) and 691, 702 nm ($^5D_0 - {}^7F_4$)]. The spectrum is dominated by the so-called "europium red" $^5D_0 - {}^7F_2$ emission as the dominant band (hypersensitive transition) peaking at 611 nm, giving an intense red luminescence output for the

complex **[I]**. The intensity ratio $I(^5D_0 - {}^7F_2)/I(^5D_0 - {}^7F_1)$ is 15.4. Such a high ratio is typical of the Eu^{3+} ion without inversion symmetry.[21]

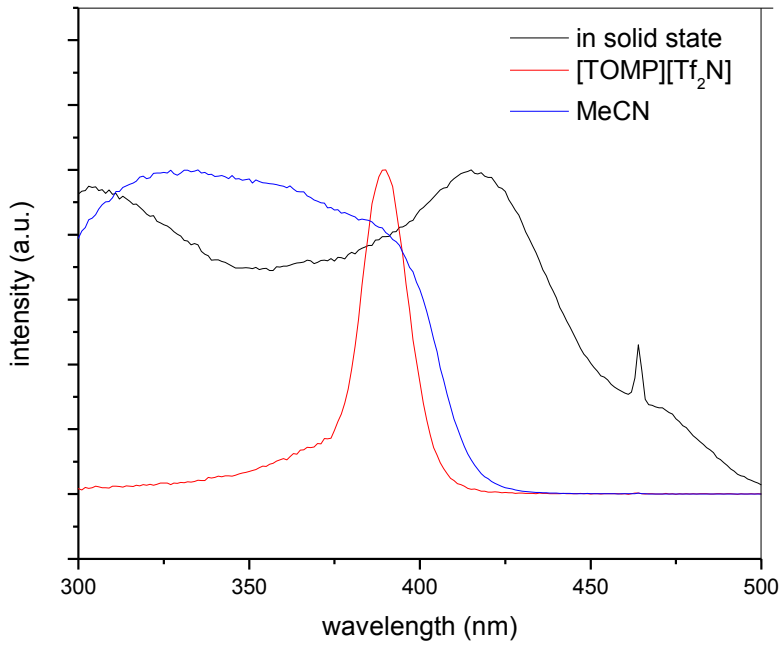

Figure 6.8: room temperature excitation spectra of complex **[I]** in solid state (λ_{em} = 611 nm), in ionic liquid [TOMP][Tf_2N] (λ_{em} = 614 nm) and in MeCN (λ_{em} = 611 nm).

Luminescence decay curve of Eu^{3+} related to the $^5D_0 - {}^7F_2$ emission in the pure europium complex **[I]** in solid state is shown in figure 6.10. The lifetime measurements were performed at room temperature and at 611 nm emission wavelength, under the excitation wavelength of a LED source at 377 nm. The decay curve is monoexponential and the lifetime of the $^5D_0$ excited state is 0.58 ms. This value is, as expected, higher than lifetimes of several tris complexes with dibenzoylmethane ligands[22] and tetrakis europium complexes.[23]

6.2.3.2 Photoluminescence of [I] dissolved in Ionic liquid

The room temperature excitation spectra of the complex **(I)** dissolved in acetonitrile (MeCN) and in the ionic liquid [TOMP][Tf_2N] are shown in figure 6.8. Absorption of the complex is shifted towards the shorter wavelength on its dissolution into MeCN solvent and in the ionic liquid [TOMP][Tf_2N]. The emission spectra of the **[I]** in solid state, dissolved in the acetonitrile

(MeCN), and in the ionic liquid [TOMP][Tf_2N] obtained by excitation at 415, 350 and 390 nm respectively, are presented in figure 6.9. The emission spectra of **[I]** are very similar in the solid state and in MeCN solution. Dissolving complex **[I]** in the ionic liquid [TOMP][Tf_2N] found to affect the spectroscopic fine structure of the emission spectrum of the compound compared to a solution of the same compound in MeCN.

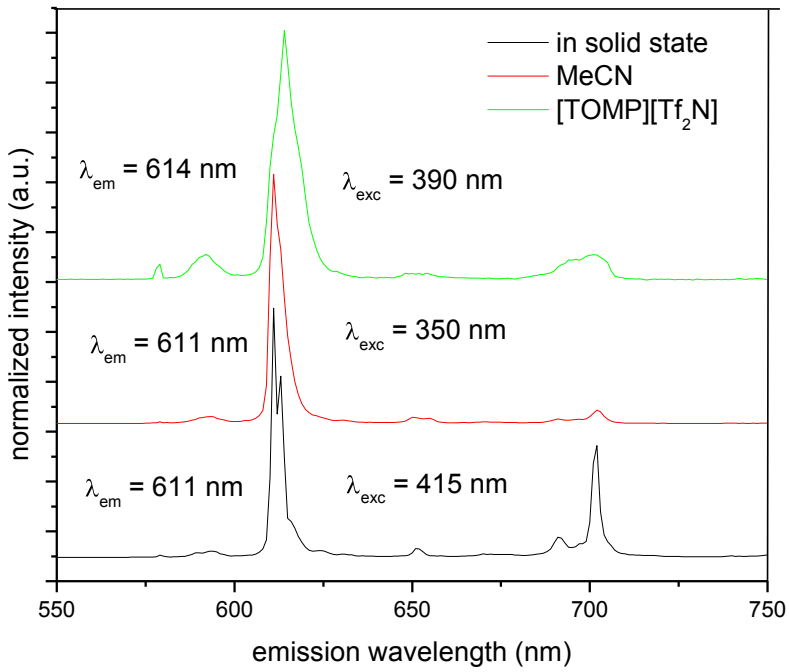

Figure 6.9: room temperature emission spectra of complex **[I]** in solid state ($\lambda_{exc.}$ = 415 nm), in MeCN ($\lambda_{exc.}$ = 350 nm) and in ionic liquid [TOMP][Tf_2N] ($\lambda_{exc.}$ = 390 nm).

The emission bands related to the $^5D_0$ – ^7F_J (J = 0 – 4) transitions are relatively broad and unsplitted. The emission band at 611 nm due to the $^5D_0$ – $^7F_2$ transition is shifted to 614 nm. The possible explanation for the band broadening and its shifting to 614 nm for the complex **[I]** dissolved in ionic liquid is related to the [Tf_2N] anions, which are known to coordinate very weakly to lanthanide ions,[24,25] and the absence of hydrogen bonding interactions between cation and ligand oxygen atoms could be responsible for this change. It should be noted that the emission spectrum for all the samples show only one peak due to $^5D_0$ – $^7F_0$ transition (579 nm), which implies that all the Eu^{3+} ions occupy a site of the same symmetry.[26,27] The hypersensitive

transition ($^5D_0 - {}^7F_2$) for the emission at 614 nm reveals changes of the coordination sphere of the Eu^{3+} ion. The symmetry and strength of the ligand field around Eu^{3+} can be determined from ratio of the relative intensities between the $^5D_0 - {}^7F_2$ / $^5D_0 - {}^7F_1$ transitions (table 6.2). In contrast to the magnetic dipole $^5D_0 - {}^7F_1$ transition, intensity of the electric dipole $^5D_0 - {}^7F_2$ transition changes with the variation of the ligand field strength. The intensity ratio for the complex **[I]** dissolved in MeCN and [TOMP][Tf_2N] is 19.7 and 9.2 respectively.

The $^5D_0$ decay curves for the complex **[I]** in solid state, **[I]** dissolved in MeCN solvent and in the ionic liquid [TOMP][Tf_2N] are shown in figure 6.10. The lifetime measurements were performed at 611 nm under the excitation wavelength of a LED source at 377 nm for the complex in solid state, the one that dissolved in MeCN solvent and at 614 nm for the complex dissolved in ionic liquid [TOMP][Tf_2N] using same excitation wavelength of 377 nm. The decay curves were fitted by a single exponential and the lifetime values for all the samples are listed in table 6.2.

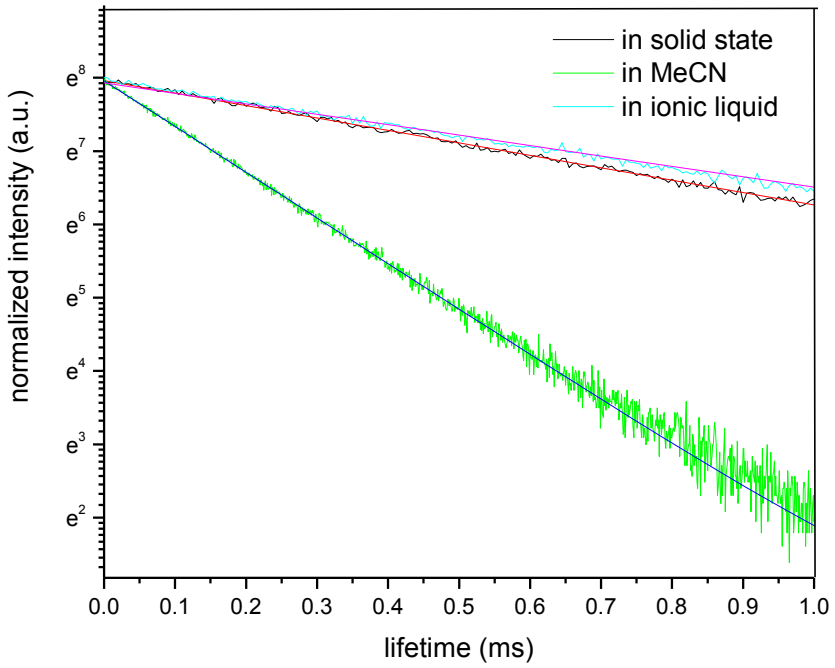

Figure 6.10: Photoluminescence decay curves for complex **(I)** in solid state, in the MeCN and in ionic liquid [TOMP][Tf_2N].

The ionic liquid sample containing the complex **[I]** show higher lifetime as compared to the lifetime value of complex in solid state and the one dissolved in MeCN solvent. It is well known

that β-diketonate ligands are unstable in the organic solvents[2] and the lower lifetime of **[I]** in MeCN could be related to the decomposition of dibenzoylmethane ligand in the MeCN solvent.

Table 6.2: the ratio between $^5D_0 - {}^7F_2$ / $^5D_0 - {}^7F_1$ transitions and lifetime values for the **[I]** in solid state, dissolved in MeCN and in ionic liquid [TOMP][Tf_2N].

Solvent	$I(^5D_0 - {}^7F_2)/I(^5D_0 - {}^7F_1)$	**τ (ms)**
Solid state	15.4	0.58
[TOMP][Tf_2N]	9.2	0.69
MeCN	19.7	0.16

6.2.3.3.Photoluminescence properties of Sm complex (II)

The room temperature excitation spectrum of the **(II)** complex in solid state is shown in figure 6.11. The excitation spectrum was recorded by monitoring emission at 650 nm; it shows a broad absorption in the 300 – 500 nm range with the maximum absorption at about 418 nm.

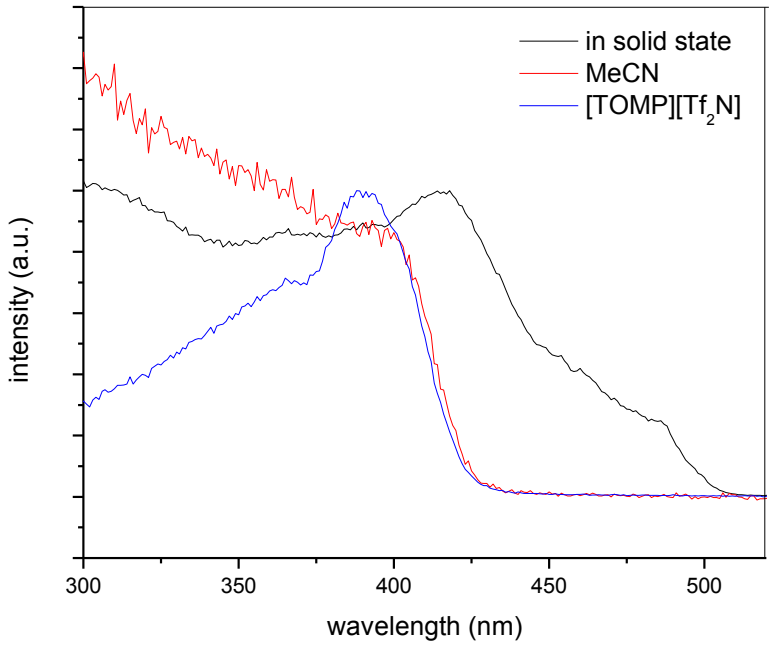

Figure 6.11: Room temperature excitation spectrum of the **[II]** complex in solid state (black line), in MeCN (red line), and in ionic liquid (blue line).

The emission spectrum of **[II]** in solid state, recorded at room temperature is shown in figure 6.12, and the assignments of lines are given in table 6.3. The emission spectrum was recorded by

excitation at 418 nm (23 923 cm^{-1}). The dibenzoyl methane ligands (dbm) absorb the excitation energy and transfer it to the Sm^{3+} emitting center in the following step. The emitting level for the samarium emission is the $^4G_{5/2}$ level. Emission spectrum exhibited four emission transitions at 563 (17 761 cm^{-1}), 608 (16 447 cm^{-1}), 650 (15 408 cm^{-1}) and 709 nm (14 104 cm^{-1}) due to $^4G_{5/2} \rightarrow {}^6H_{5/2}$, $^4G_{5/2} \rightarrow {}^6H_{7/2}$, $^4G_{5/2} \rightarrow {}^6H_{9/2}$ and $^4G_{5/2} \rightarrow {}^6H_{11/2}$ transitions. The $^4G_{5/2} \rightarrow {}^6H_{9/2}$ transition is the hypersensitive transition and responsible for the most intense line (c) in the visible region (650 nm) (15 408 cm^{-1}). The complex showed the characteristic orange color of the Sm^{3+} ion. A peak located at 563 nm (17 761 cm^{-1}), due to $^4G_{5/2} - {}^6H_{5/2}$ transition, has predominant magnetic dipolar character. For Sm^{3+} ion, the ratio between the integrated areas of the $^4G_{5/2} \rightarrow {}^6H_{9/2}$ and $^4G_{5/2} \rightarrow {}^6H_{5/2}$ (R) transitions in the emission spectrum can be used as a measure for the polarizability of its chemical environment. The intensity ratio R calculated for the complex **[II]** in solid state is 13.3. This value is quite high for a Sm^{3+} complex and is similar to Eu(III) β-diketonate complexes.

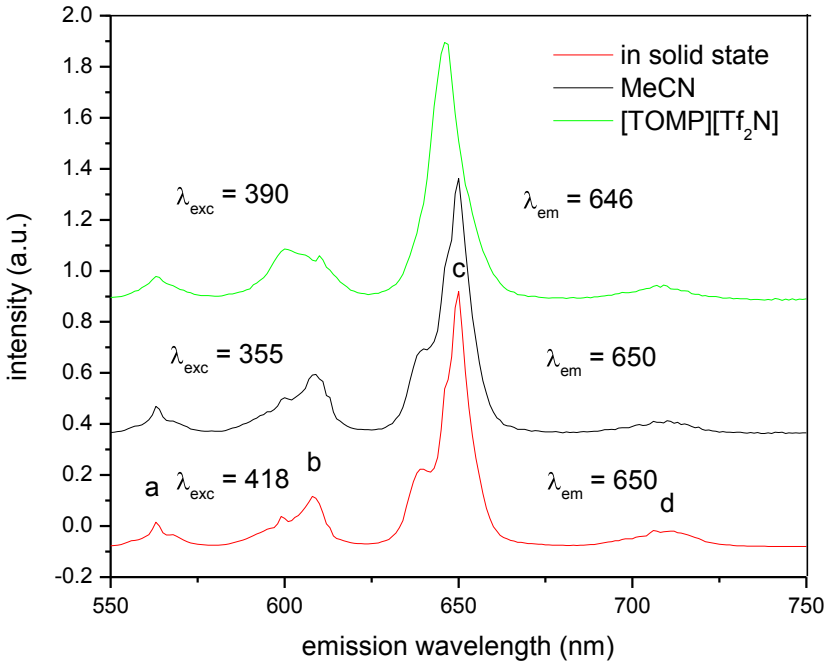

Figure 6.12: emission spectra of complex **[II]** in solid state (λ_{exc} = 418nm), dissolved in MeCN (λ_{exc} = 355 nm) and ionic liquid Tf_2N (λ_{exc} = 390 nm).

In addition to visible emission, complex **[II]** also displayed emission in the NIR region of the electromagnetic spectrum which is presented in figure 6.13 (A). The excitation wavelength was set at 418 nm. The emission spectrum show peaks corresponding to the transition from the emitting level $^4G_{5/2}$ to the different J levels of the ^6H term (^6H_J, J = 13/2, 15/2), ^4F term (^4F_J, J = 1/2, 3/2, 5/2, 7/2), and ^6F term (^6F_J, J = 9/2, 11/2). The main line in the NIR area is at 1301 nm (7686 cm^{-1}) due to $^4G_{5/2} \rightarrow {}^6F_{11/2}$ transition. Assignment of the different emission lines is summarized in the table 6.3.

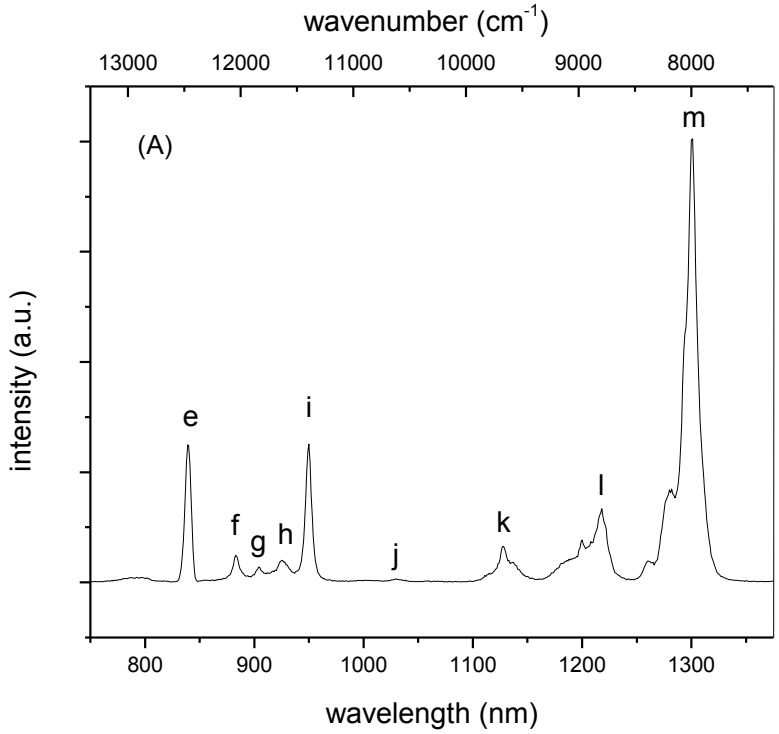

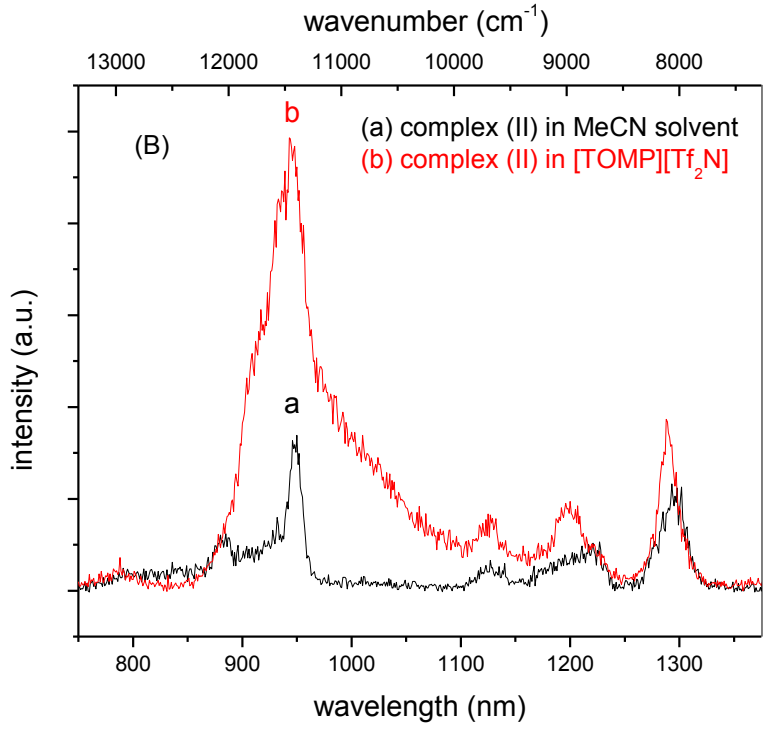

Figure 6.13: NIR luminescence of complex **[II]** in solid state (λ_{exc} = 418 nm) **(A),** dissolved in MeCN (λ_{exc} = 360 nm) **(B-a)**, and in ionic liquid [TOMP][Tf_2N] (λ_{exc} = 394 nm) **(B-b).**

Table 6.3: peak assignment for the observed Sm^{3+} transitions

line	Line assignment	Wave number (cm^{-1})	Wavelength (nm)
a	$^4G_{5/2} \rightarrow {}^6H_{5/2}$	17762	563
b	$^4G_{5/2} \rightarrow {}^6H_{7/2}$	16447	608
c	$^4G_{5/2} \rightarrow {}^6H_{9/2}$	15408	650
d	$^4G_{5/2} \rightarrow {}^6H_{11/2}$	14104	709
e	$^4G_{5/2} \rightarrow {}^6H_{13/2}$	11918	839
f	$^4G_{5/2} \rightarrow {}^4F_{1/2}$	11325	883
g	$^4G_{5/2} \rightarrow {}^4F_{3/2}$	11061	904
h	$^4G_{5/2} \rightarrow {}^6H_{15/2}$	10810	925
i	$^4G_{5/2} \rightarrow {}^4F_{5/2}$	10526	950
j	$^4G_{5/2} \rightarrow {}^4F_{7/2}$	9708	1030
k, l	$^4G_{5/2} \rightarrow {}^6F_{9/2}$	8865, 8210	1128, 1218
m	$^4G_{5/2} \rightarrow {}^6F_{11/2}$	7686	1301

The decay curve for the complex **[II]** in solid state is shown in figure 6.14 (a). The lifetime measurement was performed at 650 nm under the excitation wavelength of a LED source at 377

nm. The decay curve was fitted by a single exponential and the lifetime value derived from luminescence decay curve is 62.9 μs.

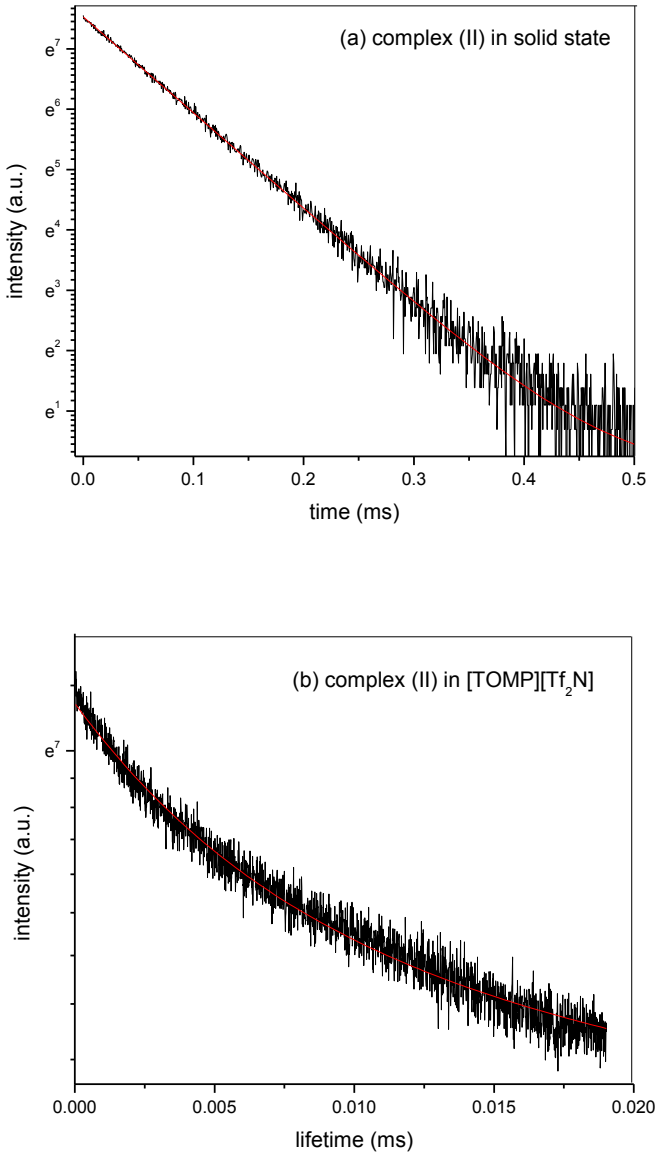

Figure 6.14: The decay curve for Sm^{3+} $^4G_{5/2} \rightarrow {}^6H_{9/2}$ emission in the samarium complex in solid state **(a)** and dissolved in ionic liquid [TOMP][Tf_2N] **(b).**

6.2.3.4.Photoluminescence of [II] dissolved in Ionic liquid

The excitation spectra of the complex **(II)** in solid state, dissolved in MeCN and in ionic liquid [TOMP][Tf_2N] are shown in the figure 6.11. The complex absorption is shifted towards shorter

wavelength when it is dissolved in MeCN solvent and in ionic liquid [TOMP][Tf_2N]. The room temperature photoluminescence emission spectra of the complex **[II]** in solid state, dissolved in MeCN and in ionic liquid [TOMP][Tf_2N] are presented in figure 6.12. The emission spectrum of the Sm complex dissolved in MeCN is similar to the one solid state. Nevertheless, the changes in the fine structure of the emission of complex **[II]** dissolved in the ionic liquid [TOMP][Tf_2N] has been observed. The emission bands related to the emitting level $^4G_{5/2}$ to the different J levels of the ^6H term (^6H_J, J = 13/2, 15/2), ^4F term (^4F_J, J = 1/2, 3/2, 5/2, 7/2), and ^6F term (^6F_J, J = 9/2, 11/2) transitions are relatively broad and unsplitted. The band at 650 nm, due to the $^4G_{5/2} \rightarrow {}^6H_{9/2}$ transition is shifted to 646 nm. This shift in the emission band indicates that the first coordination sphere of the samarium complex is influenced on its dissolution in the ionic liquid, [TOMP][Tf_2N].

The luminescence decay curves for the complex **(II)** in solid state, dissolved in ionic liquid [TOMP][Tf_2N] are shown in figure 6.14 (a) and 6.14 (b). The decay times derived from the decay curves are given in table 6.3.

Table 6.3: RI value [(ratio between the area under the emission peaks of the hypersensitive and of the magnetic-dipole allowed transitions) for the [TOMP][$Sm(dbm)_4$] complex was calculated by considering the [$I(^4G_{5/2} \rightarrow {}^6H_{9/2})$/ $I(^4G_{5/2} \rightarrow {}^6H_{5/2})$]] and the lifetime values for the **[II]** in solid state, dissolved in MeCN and ionic liquid [TOMP][Tf_2N].

Sample	**Solvent**	$I(^4G_{5/2} - {}^6H_{9/2})/I(^4G_{5/2} - {}^6H_{5/2})$	**τ (μs)**
[TOMP][$Sm(dbm)_4$]	Solid state	13.3	62.9
[TOMP][$Sm(dbm)_4$]	[TOMP][Tf_2N]	4.8	15.07 and 1.93
[TOMP][$Sm(dbm)_4$]	MeCN	12.2	Too low/could not be measured

The complex showed a low QY value of 0.1 in the ionic liquid [TOMP][Tf_2N]. The low QY for the complex **[II]** in ionic liquid [TOMP][Tf_2N] is possibly due to the traces of water in the ionic liquid, which might be introduced during the handling of sample that quenches the luminescence. This is also because the QY measurements on the complex **(II)** in ionic liquid [TOMP][Tf_2N] were performed in the visible region, which is only a part of its luminescence and the remaining part its luminescence output also lies in the NIR region. On the other hand, the QY of the solution of complex **[II]** dissolved in MeCN was too low to measure which can probably be due to the decomposition of the β-diketonate ligands of complex **(II)** in the MeCN solvent.

In addition to the emission in visible region, complex **[II]** dissolved in MeCN and [TOMP][Tf_2N] also showed emission in the NIR region of the electromagnetic spectrum as shown in figure 6.13 (B-a) and 6.13 (B-b). The emitting level for the NIR transitions is the $^4G_{5/2}$ level. In the NIR area, the most intense transition is the $^4G_{5/2} \rightarrow {}^4F_{5/2}$ transition located at 950 nm (10526 cm^{-1}).

Decay curve for the complex **(II)** in ionic liquid is biexponential and the two lifetime values were derived from the decay curves are 15.07 and 1.93 ms. The biexponential decay curve and the two lifetime values for the complex **(II)** dissolved in to ionic liquid [TOMP][Tf_2N] indicates the presence of more than one kind of sites of Sm^{3+} ion in this sample.

6.3 Conclusions

Tetrakis rare earth complexes (Eu^{3+} and Sm^{3+}) with 1,3-diphenylpropane-1,3-dione ligand were synthesized. The crystal structures of complexes (I) and (II) consists of $[TOMP]^+$ cations and complex anions. It shows that the Eu^{3+} and Sm^{3+} ions are surrounded by four 1,3-diphenylpropane-1,3-dione ligands. The coordination numbers of the Eu^{3+} and Sm^{3+} ions are eight. No solvent molecules are coordinated to the central metal ions. Unlike imidazolium cation based lanthanide tetrakis complexes, there is no hydrogen bonding interaction between [TOMP] cation and the complex anion due to the lack of acidic protons on the phosphonium cation in these complexes. Both the Eu and Sm tetrakis complexes showed thermal stability up to 250 and 285 °C, respectively. Photoluminescence of complexes (I) and (II) in phosphonium ionic liquid [TOMP][Tf_2N] were studied and The changes in the fine structure of emission spectra were observed. Complex (I) showed a single exponential decay curve and a higher lifetime value of 0.69 ms when it was dissolved in to ionic liquid [TOMP][Tf_2N]; while in the acetonitrile solvent, lower lifetime of 0.16 ms was measured. This decrease could be possibly due to the decomposition of β-diketonate ligands in the acetonitrile solvent. Complex (II) showed a biexponential decay profile and two lifetime values (15.07 and 1.93 ms) when it was dissolved into ionic liquid. This indicates that this sample contains more than one kind of Sm^{3+} ion sites. Nevertheless, the tunable properties of phosphonium ionic liquids together with the dissolution of tetrakis-β-diketonate complexes of lanthanides can open up new potential applications for

these materials, e.g. for study of the electrochemical properties and electrodeposition of f-elements.

6.4 References

[1] Rik Van Deun, Dries Moors, Brecht De Fré and Koen Binnemans, J. Mater. Chem., 2003, 13, 1520-1522.

[2] Peter Nockemann, Eva Beurer, Kris Driesen, Rik Van Deun, Kristof Van Hecke, Luc Van Meervelt and Koen Binnemans, Chem. Commun., 2005, 4354-4356.

[3] K. Driesen, P. Nockemann and K. Binnemans, Chem. Phys. Lett., 2004, 395, 306-310.

[4] S. Arenz, A. Babai, K. Binnemans, K. Driesen, R. Giernoth, A.-V. Mudring and P. Nockemann, Chem. Phys. Lett., 2005, 402, 75.

[5] I. Billard, S.Mekki, C. Gaillard, P. Hesemann, G. Moutiers, C.Mariet, A. Labet and J.-C. G. Bünzli, Eur. J. Inorg. Chem., 2004, 6, 1190-1197.

[6] E. Guillet, D. Imbert, R. Scopelliti and J.-C. G. Bu¨nzli, Chem. Mater., 2004, 16, 4063-4070.

[7] Kyra Lunstroot, Peter Nockemann, Kristof Van Hecke, Luc Van Meervelt, Christiane Gorller-Walrand, Koen Binnemans, and Kris Driesen, Inorg. Chem., 2009, 48, 3018-3026.

[8] Puntus, L. N.; Schenk, K. J.; Bünzli, J.-C. G. Eur. J. Inorg. Chem., 2005, 4739-4744.

[9] Babai, A.; Mudring, A. V. Chem. Mater., 2005, 17, 6230-6238.

[10] K. Binnemans, Chem. Rev., 2007, 107, 2592-2614.

[11] Gaillard, C.; Billard, I.; Chaumont, A.; Mekki, S.; Ouadi, A.; Denecke, M. A.; Moutiers, G.; Wipff, G. Inorg. Chem., 2005, 44, 8355-8367.

[12] Samikkanu, S.; Mellem, K.; Berry, M.; May, P. S.Inorg. Chem., 2007, 46, 7121-7128.

[13] Nagaishi, R.; Arisaka, M.; Kimura, T.; Kitatsuji, Y. J. Alloys Compd., 2007, 431, 221-225.

[14] J.D. Holbrey, K.R. Seddon, Clean Products and Processes, 1999, 1 223-236.

[15] Matthew R. Netherton and Gregory C. Fu, Org. Lett., Vol. 3, No. 26, 2001.

[16] Christine J. Bradaric , Andrew Downard , Christine Kennedy , Allan J. Robertson and Yuehui Zhou, Green Chem., 2003, 5, 143-152.

[17] Linda M. Sweeting and Arnold L. Rheingold, J. Am. Chem. Soc., 1987, 109, 2652-2658.

[18] Bihai Tong, Shuanjin Wang, Yuezhong Meng and Biao Wang, Photochem. Photobiol. Sci., 2007, 6, 519-520.

[19] Zhao Dan, Qin Weiping, Wu Changfeng, Zhang Jisen, Qin Guanshi, Lin Haiyan, J. Rare Earths, 2004, 22, 49.

[20] Xianmin Guo, Jean-Louis Canet, Damien Boyer, Pierre Adumeau, Rachid Mahiou, J Sol-Gel Sci Technol., 2012, 64, 404-410.

[21] Görller-Walrand, C.; Binnemans, K. "Spectral intensities of f-f transitions" in: Handbook on the physics and chemistry of rare earths, Vol. 25 eds K.A. Gschneidner Jr and L. Eyring (North-Holland, Amsterdam) ch., 167, 101-264.

[22] Biao Chen, Yanhua Luo, Hao Liang, Jie Xu, Fuquan Guo, Yizhong Zhang, Aibin Lin, Xuan Liu, Spectrochimica Acta Part A, 2008, 70, 1203-1207.

[23] J.P. Duignan, I.D.H. Oswald, I.C. Sage, L.M. Sweeting, K. Tanaka, T. Ishihara, K. Hirao, G. Bourhill, Journal of Luminescence, 2002, 97, 115-126.

[24] Y. Hasegawa, K. Sogabe, Y. Wada and S. Yanagida, J. Lumin., 2003, 101, 235.

[25] R. Van Deun, P. Nockemann, C. Go¨rller-Walrand and K. Binnemans, Chem. Phys. Lett., 2004, 397, 447.

[26] Koen Binnemans, Philip Lenaerts, Kris Driesen and Christiane Görller-Walrand, J. Mater. Chem., 2004, 14, 191-195.

[27] William Dew. Horrocks Jr., Michael Albin, Progress in Inorganic Chemistry, 1984, 31, 1-104.

ACKNOWLEDGEMENTS

Many people helped me with this thesis and deserve my gratitude; my sincere apologies if I have inadvertently omitted anyone to whom acknowledgement is due.

Foremost, my most sincere gratitude and respect go to my research supervisor Prof. Alvise Benedetti for his commitment to guiding me through my doctoral research, for his patience, wisdom, and mentoring. I will remain grateful for the opportunity he offered me to join his research group. The joy and enthusiasm he has for the research was motivational for me, even during the tough times in this pursuit. You are one of a kind. Working with you was the experience of a lifetime

I am much indebted to Prof. Pietro Riello and Stephano Pollizi, for all the valuable suggestions and support. This work would not have been possible without their guidance.

Remembering the time I spent in National Chemical Laboratory (NCL), Pune (INDIA). I want to thank Dr. A. J. Varma. It was his guidance that motivated me to pursue my interests in research. His advice in research helped me to evolve into a scientist and his wisdom in life taught me valuable lessons to become a better person. Without his encouragement and support, I would not have been able to achieve what I have accomplished as a researcher.

I wish to extend my warmest thanks to K. V. Pandare, whom I have great regard, for the encouragement and support he had provided in the NCL.

I would like to express my earnest appreciation and gratitude to Dr. Luca Bellotto and Dr. Isidora Freris for the encouragement and for having helped me significantly with this work.

Chapter 4 is the result of a productive collaboration with the “solid state NMR group” from the University of Pisa. Therefore, I would like to thank Prof. Marco Geppi, Dr. Silvia and Dr. Uma for their enthusiastic cooperation.

Special thanks go to Prof. Alvise Perosa and his research group (Dr. Marco, Manuela, and Dr. Giulia) for the fruitful collaboration, allowing me to work in their laboratory and helping me with the synthesis and characterization of ionic liquids.

I would like to express my appreciation for the precious help that I have received over the past few years from many wonderful people, in particular I kindly acknowledge: Dr. Francesco Enrichi of C.I.V.E.N. (Coordinamento Interuniversitario Veneto per le Nanotecnologie), for giving me an opportunity to work in the optics laboratory and also for his kind assistance during the luminescence measurements, most of the reported measurements would have not possible without him; Mr. Davide Cristofori for the TEM analysis and for his kindness and humor; Prof. Elisabetta Zendri and her research group (Dr. Francesca Izzo, Dr. Manuela Sgobbi and Dr. Eleonora Balliana) for giving me the opportunity and assistance to carry out the TGA measurements; Prof. Loretta Storaro and her research group (Mrs. Martina Marchiori, Dr. Elisa Moretti, Mr. Aldo Talon) for the N_2 adsorption-desorption analysis and for giving me an opportunity to perform the DRIFT spectroscopy measurements; Mr. Tiziano Finotto and Mr. Loris Bertoldo for performing the XRD measurements and also for their valuable assistance and kind help to tackle my day to day problems and making me feel at home during my stay in Venice; Dr. Jasper Plaisier and Nicola Demitri for the single crystal X-ray structure determination of lanthanide complexes at the Elettra Synchrotron source (Trieste, Italy); Marta Maria Natile from ISTM-CNR, INSTM, Dipartimento di Scienze Chimiche, Università di Padova, Italy for her valuable help with quantum yield measurements; Prof. Amadelli Rossano and Dr. Luca Samiolo for the Diffuse reflectance UV-visible spectroscopic measurements; Prof. Mirella Zancato of University of Padova, Italy for the elemental Analysis. I would also like to thank Dr. Cattaruzza Elti and Prof. Battaglin for the general assistance.

This thesis was edited several times. A special thank goes to my internal reviewer, Dr. Marco Bortoluzzi, for his valuable suggestions.

Francesca Guidi was always ready and able to solve administrative problems, many thanks to her for the kind assistance she has provided.

I would be remiss if I did not acknowledge Dr. Alvise Parma, who has been a good friend and helped me in many ways. Many thank to him for his kind assistance during my doctoral research.

ACKNOWLEDGEMENTS

I thank all my colleagues, especially: Gloria, Marco, Marta, Gabrielle, Nicolo, Riccardo, Marcello, Marta, Marika, and Laura. Thanks also to my roommate Vikas for his help while writing this thesis.

I thank my past colleagues in NCL: Dr. Rakesh, Dr. Hamid, Nishikant, Anil, Bashirbhai, Dr. Kalpana, Sam, Dhirubhai, Nagesh, Maroti, Majid who have been helping me in many ways.

The lifetime of thank go to my beloved parents for their persistent support during my academic life. I always owe to their love, and sacrifices, which have brought me up to this level.

Finally, I want to thank my wife Swati, for her endless understanding, patience, encouragement and love when it was most required.

APPENDIX

PUBLICATIONS

[1] **C. Malba**, Luca Bellotto, Isidora Freris, Francesco Enrichi, Davide Cristofori, Pietro Riello, Alvise Benedetti, *"In situ synthesis of Eu(Tp)3 complex inside the pores of mesoporous silica nanoparticles"* ***J. Lum.,*** 2013, *142*, 28-34.

[2] E. Moretti, L. Bellotto, M. Basile, **C. Malba**, F. Enrichi, A. Benedetti, S. Polizzi, *"Investigation on the effect of $Tb(dbm)_3phen$ on the luminescent properties of $Eu(dbm)_3phen$ containing mesoporous silica nanoparticles"* has been accepted for publication in ***Materials Chemistry and Physics*****,** 2013.

[3] **C. Malba**, U. Sudhakaran, S. Borsacchi, M. Geppi, M. Natile, F. Enrichi, I. Freris, P. Riello, A. Benedetti, *"Structural and photo-physical properties of rare-earth complex encapsulated into surface modified mesoporous silica nanoparticles"*, in preparation.

[4] **C. Malba**, F. Enrichi, M. Facchin, J. Plaisier, A. Perosa, M. Natile, P. Riello, A. Benedetti, *"Phosphonium ion based tetrakis dibenzoylmethane Eu(III) and Sm(III) complexes: Synthesis, crystal structure determination and luminescence properties in weakly coordinating phosphonium ionic liquid"* in preparation.

POSTER PRESENTATIONS

C. Malba, L. Bellotto, I. Freris, F. Enrichi, P. Riello, A. Benedetti, "*Preparation and Characterization of Functional Materials for Energy Applications*", International conference on Micro- and nano-photonic materials and devices - Jan. 16 - 18, 2012, Trento, Italy.

Estratto per riassunto della tesi di dottorato

L'estratto (max. 1000 battute) deve essere redatto sia in lingua italiana che in lingua inglese e nella lingua straniera eventualmente indicata dal Collegio dei docenti.

L'estratto va firmato e rilegato come ultimo foglio della tesi.

Studente: Chandrashekhar Marotirao Malba matricola: 955770

Dottorato: Scienze Chimiche Scuola di dottorato in Scienze e Tecnologie

Ciclo: XXV

Titolo della tesi[1] : Synthesis and characterization of lanthanide based luminescent materials

Abstract:

In this thesis, synthesis and characterization of new lanthanide based luminescent hybrid materials is studied. The thesis consists of two parts. The silica based luminescent hybrid nanomaterials have been prepared and studied in the first part. The different ways for the nanoencapsulation of rare earth complexes in mesoporous silica nanoparticles have been used to prepare highly luminescent nanomaterials. A highly luminescent $Eu(Tp)_3$ complex with limited solubility in organic solvents has been synthesized in situ inside the pores of presynthesized mesoporous silica nanoparticles. The effect of different chemical environment in the silylated mesoporous silica nanoparticles on the luminescence properties of the Eu(III) complex has been studied in detail by encapsulating $Eu(dbm)_3$phen complex in the pores of organically modified mesoporous silica nanoparticles. Furthermore, solid state NMR studies were performed on the $Y(dbm)_3$phen encapsulated mesoporous silica nanoparticles to obtain the structural and dynamic information on these materials. Co-luminescence effect of Tb(III) and Eu(III) complexes has been studied in the mesoporous silica matrix, with the aim of improving luminescence properties of the encapsulated Eu(III) complex. In the second part of this PhD thesis, new anionic tetrakis lanthanide complexes have been synthesized, characterized and their luminescence properties have been studied in detail in the solid state. Furthermore, the luminescent soft materials were prepared by dissolving anionic tetrakis lanthanide complexes in the phosphonium ionic liquids. The phosphonium ionic liquids have been explored as spectroscopic solvents for studying luminescence of new tetrakis lanthanide complexes.

Estratto:

In questa tesi e' stata condotto uno studio che ha riguardato la sintesi e la caratterizzazione di nuovi materiali ibridi luminescenti a base di lantanidi. La tesi si compone di due parti. Nella prima parte sono stati preparati e studiati dei nanomateriali ibridi luminescenti a base di silice. Sono state utilizzate diverse modalita' per il nanoincapsulamento di complessi di terre rare in nanoparticelle di silice mesoporose per preparare nanomateriali altamente luminescenti. Il complesso luminescente $Eu(Tp)_3$, che genralmente mostra una limitata solubilità in solventi organici, è stato sintetizzato in situ all'interno dei pori delle nanoparticelle di silice mesoporose pre-sintetizzate. E' stato inoltre studiato in dettaglio l'effetto di diverse funzionalizzazioni di nanoparticelle di silice mesoporosa sulle proprietà luminescenti del complesso $Eu(dbm)_3$phen tramite il suo incapsulamento nei pori modificati sulla superficie delle nanoparticelle di silice mesoporose. Per ottenere le informazioni strutturali e dinamiche su questo tipo di sistemi si sono condotti anche degli studi NMR, allo stato solido, su nanoparticelle di silice mesoporose con il complesso $Y(dbm)_3$phen incapsulato. L'effetto di columinescenza dei complessi di Tb(III) e Eu(III) è stato studiato in matrice di silice mesoporosa,

[1] Il titolo deve essere quello definitivo, uguale a quello che risulta stampato sulla copertina dell'elaborato consegnato.

allo scopo di migliorare le proprietà di luminescenza del complesso di Eu(III) incapsulato in essa. Nella seconda parte di questa tesi di dottorato, sono stati inoltre sintetizzati e caratterizzati nuovi complessi anionici tetrakis conteneti elementi lantanoidi allo stato solido, e sono state studiate in dettaglio le loro proprietà luminescenti. Infine, sono stati preparati materiali luminescenti “soffici” sciogliendo complessi anionici tetrakis conteneti elementi lantanoidi in liquidi ionici a base di fosfonio e sono state studiate le proprità luminescenti relative.

Firma dello studente

_____